

A Thesis Submitted for the Degree of PhD at the University of Warwick

Permanent WRAP URL:

<http://wrap.warwick.ac.uk/157203>

Copyright and reuse:

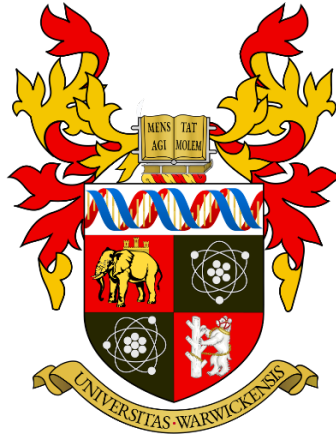
This thesis is made available online and is protected by original copyright.

Please scroll down to view the document itself.

Please refer to the repository record for this item for information to help you to cite it.

Our policy information is available from the repository home page.

For more information, please contact the WRAP Team at: wrap@warwick.ac.uk



Experimental and Theoretical Study of Capillary Force
in Adhesive Contact between Microspheres

by

Lidong Liu

Thesis Submitted to the University of Warwick

for the Degree of

Doctor of Philosophy

School of Engineering

Feb 2021

Contents

| | |
|---|-----|
| List of Figures | iv |
| List of Tables | vii |
| Acknowledgments | ii |
| Declaration | iii |
| Abstract | iv |
| Abbreviations | v |
| 1 General introduction | 1 |
| 1.1 Introductions | 1 |
| 1.2 The motivation of the study | 2 |
| 1.3 The aim of this study | 3 |
| 1.4 The methodology | 8 |
| 1.5 The structure of the thesis..... | 11 |
| 2 Experimental methods | 12 |
| 2.1 Introduction..... | 12 |
| 2.2 Review of the previous methods..... | 12 |
| 2.2.1 Atomic force microscopy (AFM)..... | 13 |
| 2.2.2 Surface forces apparatus (SFA)..... | 17 |
| 2.2.3 Centrifuge technique | 19 |
| 2.2.4 Environmental scanning electron microscopy (ESEM) | 20 |
| 2.3 A novel technique for measuring interparticle capillary force | 21 |
| 2.3.1 Experimental setup | 22 |
| 2.3.2 The major merits of the current system..... | 28 |
| 3 Theoretical backgrounds..... | 30 |
| 3.1 Introduction of the capillary force | 30 |
| 3.2 Liquid surface tension: the origin of the capillary force..... | 31 |
| 3.3 Liquid-condensation capillary | 33 |
| 3.4 The capillary force between soft particles | 35 |
| 3.4.1 Classical contact theories | 36 |
| 3.4.2 Applications of the models..... | 37 |
| 3.5 The capillary force between rigid particles..... | 38 |
| 3.5.1 Young-Laplace equation and its variants | 38 |
| 3.5.2 Applications of the models..... | 39 |

| | | |
|-------|---|------------|
| 4 | Capillary force in adhesive contact between hydrogel microspheres..... | 41 |
| 4.1 | Introductions | 41 |
| 4.2 | Experimental section | 43 |
| 4.2.1 | Fabrication of hydrogel microparticles | 43 |
| 4.2.2 | Preparation of hydrogel disk | 43 |
| 4.2.3 | Capillary force measurements | 43 |
| 4.2.4 | Indentation testing | 48 |
| 4.3 | Theoretical basis | 50 |
| 4.3.1 | Contact mechanics and adhesion..... | 50 |
| 4.3.2 | Viscoelastic model..... | 54 |
| 4.4 | Results and discussion | 57 |
| 4.5 | Summary..... | 66 |
| 5 | Investigations of humidity influencing interparticle capillary force | 67 |
| 5.1 | Introduction: | 67 |
| 5.2 | Experimental section | 70 |
| 5.2.1 | Experimental procedure..... | 70 |
| 5.2.2 | Surface roughness measuring | 72 |
| 5.3 | Analytical and numerical analyses | 73 |
| 5.3.1 | First-order approximation..... | 73 |
| 5.3.2 | Numerical model | 77 |
| 5.3.3 | Influence of the surface roughness | 82 |
| 5.4 | Results and discussion | 87 |
| 5.5 | Summary..... | 97 |
| 6 | Conclusions and future work | 98 |
| 6.1 | The governing effects responsible for the observed capillary forces | 98 |
| 6.2 | The experimental method | 99 |
| 6.3 | The theoretical interpretation..... | 100 |
| 6.3.1 | For soft hydrogel microparticles with capillary rises from the accumulation of absorbed liquid | 100 |
| 6.3.2 | For rigid microparticles with capillary rises from liquid condensation influenced by RH | 101 |
| 6.4 | Future work..... | 101 |
| | References | 103 |

List of Figures

Figure 1.1 The schematic of the force-displacement (F - D) curve in capillary adhesive contact between hydrogel microspheres measured by pull-off testing. The cyan-blue line is representative of the force versus approach data measured by the novel experimental setup. The measured F - D curve can be divided into three distinct phases: I. two hydrogel spheres had a solid-to-solid contact, the capillary was formed from squeezed liquid. II. two hydrogel spheres had no more solid-to-solid contact. But they were linked by the capillary bridge in between. III. two hydrogel spheres were completely separated, the capillary bridge in between ruptured and the liquid was re-absorbed by the hydrogels.....5

Figure 1.2 The schematic (with exaggerated surface profile) of the surface roughness influences capillary force in adhesive contact between PMMA microspheres under various RH environments. The red line is representative of the measured adhesion force against RH. In the low humidity environment, as shown in I., only a few small capillary bridges formed between the surface roughness asperities. In the medium humidity environment, as shown in II., more capillary bridges formed. In the high humidity environment, as shown in III., smaller capillary bridges merged into one...6

Figure 1.3 A flow chart outlines the methodology of current work and potential applications.10

Figure 2.1 Schematic of atomic force microscopy. A laser beam is reflected on the cantilever and received by the photodetector. By knowing the stiffness of the cantilever spring and the obtained laser signal from the photodetector, an accurate force between the tip and the sample can be determined..... 15

Figure 2.2 Schematic of a typical SFA setup. Two contacting cylinders are aligned vertically. One cylinder is mounted to a piezoelectric transducer, and the other cylinder is mounted to a spring with a known spring constant. A white light illuminates the contacting area, and a spectrometer analyzer captures the image optically. The separation displacement between the two contacting surfaces is measured optically using multiple-beam interference fringes. 18

Figure 2.3 (a) Schematic (not to scale) and (b) image of the experimental setup to measure adhesion.23

| | |
|--|----|
| Figure 2.4 Schematic of the system data flow. The arrows indicate the direction of the data flow between different modules. | 26 |
| Figure 4.1 (a) Micrographs and (b) schematic of the liquid bridge formed between two agarose hydrogel spheres. | 45 |
| Figure 4.2 The side-view images acquired at a constant separation speed of 20 $\mu\text{m/s}$, show (a) the capillary breakage and (b) the liquid re-absorbed completely after 0.166 s. | 47 |
| Figure 4.3 (a) Schematic of the alternative spherical indentation test for measuring Young's modulus of the agarose gel independently (not to scale). (b) Comparison of theoretical and the experimental indentation force F versus indentation depth h , $F(h)$ curve (measured at a constant loading speed 20 $\mu\text{m/s}$). Young's modulus was 72 kPa for the prediction of Hertz theory with least-square fitting..... | 49 |
| Figure 4.4 Schematic diagram of Voigt model, the system consists of a Newtonian dashpot and linear elastic spring connected in parallel undergoing the same deformation. | 56 |
| Figure 4.5 Comparison of experimental force-approach $P(\delta)$ curve (measured at a constant separation speed 20 $\mu\text{m/s}$) and the JKR theoretical prediction with least-square fitting. | 59 |
| Figure 4.6 (a) The unloading force-approach $P(\delta)$ curves measured at different separation speeds. (b) The JKR-fitted values of Young's modulus E and work of adhesion $\Delta\gamma$ | 62 |
| Figure 4.7 (a) Using least-squares fitting experimental force-time $P(t)$ curve (measured at a constant speed 20 $\mu\text{m/s}$) with the Eq. (4.27). (b) Comparison of the measured Young's modulus E at various separation speeds and the prediction of the viscoelastic model using the Eq. (4.30). | 65 |
| Figure 5.1 The schematic of the experimental setup (not to scale)..... | 71 |
| Figure 5.2 Micrographs of the PMMA spheres in contact..... | 71 |
| Figure 5.3 Schematic of the liquid bridge formed between two PMMA spheres of the same radius..... | 74 |
| Figure 5.4 Schematic of the coordinate system for the numerical solution based on the DS model. Capillary forms between two spheres of the identical radius R_s , with the | |

| | |
|--|----|
| filling angle β and contact angle θ . The first calculation vertex is located on Sphere 1. | 79 |
| Figure 5.5 Flowchart of numerical calculation for the geometric shape of the meniscus..... | 81 |
| Figure 5.6 Schematic of capillary bridges forming between asperities of two spheres under different RH (not to scale): (a) only one capillary bridge forms between asperities under low RH; (b) number of capillary bridges increases with RH; (c) various smaller capillary bridges merge into one. | 83 |
| Figure 5.7 (a) the uniform surface roughness function φ_1 and the joint surface roughness function φ are assumed in Butt's model; (b) the experimental surface roughness function measured by AFM, fitted with Gaussian distribution with $\mu = 0$ and $\sigma = 1.8$ | 86 |
| Figure 5.8 Experimental force-distance (F - D) curve (measured at a constant separation speed $1 \mu\text{m/s}$) in comparison with the predictions of: (a) the first-order approximation; (b) the DS model..... | 88 |
| Figure 5.9 Capillary geometric boundary between two PMMA spheres using the DS model and first-order approximation (unit in μm); (a) quarter view of two liquid-bridge spheres; (b) the calculated shape of the meniscus, and the subtle difference of the predictions between the DS model and first-order approximation in: (c) the near-wall slop and (d) the profile of the meniscus neck. | 90 |
| Figure 5.10 The adhesion force between two PMMA spheres under different RH compared with the theoretical predictions based on equations (5.19) and (5.22)..... | 92 |
| Figure 5.11 AFM measurements of (a) surface topography and (b) RMS roughness, carried out on two different areas from two different PMMA spheres (256 sampling points per line, $5 \times 5 \mu\text{m}^2$). The 8×8 pixels RMS distribution maps in (b) were constructed from the roughness heights of the topography in (a). (c) shows the measured asperity height distribution of surface roughness. | 94 |
| Figure 5.12 The comparison between Butt's joint surface roughness function φ_{Butt} calculated by the uniform surface roughness distribution and the joint surface roughness function φ_{Exp} calculated by the Gaussian distribution fitted by the experimental surface roughness data. | 96 |

List of Tables

| | | |
|-------------------|--|---|
| Table 1. 1 | The characteristics of the investigated microparticles. | 7 |
|-------------------|--|---|

Acknowledgments

I would like to express my extreme gratitude to my supervisor Dr. Isaac Kuo-Kang Liu who has been my beacon light and motivator throughout the time as his student. It has been a great honor and privilege to take training under his supervision. His modesty, professional insights, rigorous attitude to every detail and immense effort above and beyond his duty taught me so much not only on academic level, but also as how to become a better human being.

My thanks also go to Prof. Kai-Tak Wan at Northeastern University, Dr. Humphrey Yiu at Heriot-Watt University for their useful discussions about my projects and the help on reviewing the manuscripts; to Dr. Tianrong Jin, Dr. Eleftherios Siamantouras, Dr. Xinyao Zhu and Dr. Binglin Tao for their help in numerous aspects in my research (e.g., experimental setup and theoretical modeling). I would like to thank Mr. Zhuonan Yu, especially for his help on the LabView program coding and experimental instruments. Without his kind and unselfish help, I could not have the ability to finish my projects. I would like to thank the School of Engineering, University of Warwick for the scholarship that partially funded my Ph.D.. I acknowledge the technical support from the technicians from School of Engineering, Department of Physics and Warwick Manufacturing Group (WMG) (e.g., building the experimental instrument, using the 3D optical microscope and scanning electron microscope).

I enjoyed my Ph.D. study with the help of my friends. I have been so fortunate to have them supporting every aspects of my life in UK. My gratitude goes to Dr. Shudi Dong, Dr. Chengxi Zhao, Mr. Yixin Zhang, Dr. Jin Ren, Mr. Xingguang Xu, Mr. Fei Gao and Dr. Zeng Luo for keeping me company. I shall always cherish this precious memory.

Finally, I would like to express my most sincere thanks to my beloved family for their endless support, tireless encouragement, and unconditional love, especially to my parents, Mr. Xingwu Liu, Mrs. Qingping Liu and my girlfriend, Ms. Siyun Zhan.

Declaration

This thesis is submitted to the University of Warwick in support of my application for the degree of Doctor of Philosophy. No part of this thesis has been submitted for a research degree at any other institution.

Parts of this thesis have been published by the author:

- Lidong Liu, Kuo-Kang Liu. Capillary force in adhesive contact between hydrogel microspheres. *Colloids and Surfaces A: Physicochemical and Engineering Aspects*, Volume 611, Issue 2021: (125828). doi: 10.1016/j.colsurfa.2020.125828

Parts of this thesis have been presented by the author:

- Lidong Liu, Kuo-Kang Liu. Capillary adhesive contact between soft microparticles. International Conference on Adhesion in Aqueous Media: From Biology to Synthetic Materials AAM2019, Dresden, Germany, 9th – 12th September 2019.
- Lidong Liu, Kuo-Kang Liu. Capillary adhesive contact between soft microparticles. 707. WE-Heraeus-Seminar Wetting and Capillarity in Complex Systems, Bad Honnef, Germany, 24th – 29th November 2019.

Abstract

This thesis describes investigations into the capillary forces between microparticles (ca. 200-1000 μm in diameter). Its original contributions to knowledge are the validations and developments of the existing theories both experimentally and theoretically.

A novel technique for force-displacement measuring, in combination with an image acquisition system, has been developed to directly measure the capillary forces between two microparticles. The instrument is also capable of recording the side-view profile of the contacting process optically, which is necessary to correctly identify the geometric shape of the capillary, the pole-to-pole alignment, as well as the deformation behavior of these particles. The experiments cover samples with different mechanical properties, i.e. soft hydrogel and rigid polymer particles. The theoretical studies undertaken include both analytical and numerical analyses, which are developed for interpreting the experimental data. Classical contact mechanics theory such as Johnson-Kendall-Roberts (JKR) theory is used for the capillary formed spontaneously between two soft sponge-like hydrogel microparticles, while Kelvin equation and Young-Laplace equation are applied for the capillary formed between two PMMA microparticles due to liquid condensation.

In general, the experimental data and the theoretical predictions show good agreement in both soft and rigid microparticles. For soft microparticles, the current research findings show that the work of adhesion is independent of the separation speed and, by contrast, Young's modulus exhibits a linear increase with the separation speed. A viscoelastic model is used to further quantitatively characterize the deformation behavior of the soft hydrogel. It also demonstrates that the JKR theory reconciles with the generalized Hertz theory, which takes capillary force into account for soft microspheres in a relationship that the work of adhesion is equal to twice the surface tension of water. For rigid microparticles, both analytical and numerical models have been used to interpret the force-displacement curves measured during separation. The results demonstrate both the adhesion force and the capillary volume increase monotonically with the rise of the relative humidity. Also, subtle differences in the calculated capillary profile and adhesion forces between the analytical solution and the numerical simulation have been revealed. A surface roughness model is used to quantify the adhesion under the effect of relative humidity.

These new findings are essential for developing techniques to quantitatively characterize the capillary force of colloids and granular materials and potentially to improve the material performance in their applications.

Abbreviations

| | |
|-------|--|
| AFM | atomic force microscopy |
| CCD | charge-coupled device |
| cm | centimeter |
| DAQ | data acquisition |
| DMT | Derjaguin-Muller-Toporov |
| DS | Dörmann and Schmid |
| ESEM | environmental scanning electron microscopy |
| F-D | Force-Displacement |
| g | gram(s) |
| Hz | Hertz |
| IC CJ | Interactive Control Centre Joystick |
| J | joule |
| JKR | Johnson-Kendall-Roberts |
| K | Kelvin |
| kPa | kilo-pascal |
| m | meter |
| ml | milliliter |
| mN | millinewton |
| mol | mole |
| MPa | mega-pascal |
| N | newton |
| nm | nano-meter |
| PCI | peripheral component interconnect |
| PMMA | polymethyl methacrylate |
| pN | piconewton |
| RH | relative humidity |
| RMS | root mean square |
| s | second(s) |
| SFA | surface forces apparatus |
| SEM | scanning electron microscope |

| | |
|-----|-------------------------------|
| SFM | scanning force microscopy |
| SPM | scanning probe microscopy |
| STM | scanning tunneling microscopy |
| W/W | weight/weight |
| Å | Ångström |
| μm | micro-meter |
| μN | micronewton |

1 General introduction

The main purpose of this chapter is directed to defining the problem which has been investigated and the objectives of the current work. A preliminary survey of the potential applications which may be derived from this study is also described. In addition, the main theme of this thesis, a novel methodology for characterizing capillary force , which combines both theoretical and experimental approaches are addressed briefly. Finally, a brief structure of the thesis is presented.

1.1 Introductions

Adhesion among particles as well as adhesion between particles and surfaces are fundamental to solids processing. They have significant impacts on the physical behaviors of biological [1], chemical [2], pharmaceutical [3], food [4], anti-icing [5], and cosmetic materials[6], such as sticking to surfaces, agglomerating, and breaking [7]. From an industrial aspect, these physical behaviors will ultimately affect the reproducibility and the quality of these solid particles [8,9] or fluid [10]. Serval interfacial forces such as Van der Waals, dipole-induced forces, electrostatic forces, and capillary forces influence the strength of the adhesion [11]. Among them, the capillary force is of particular interest because it tends to dominate the adhesion interaction when presents in most cases [12–14]. This strong adhesion caused by liquid menisci, which is formed around the contact areas of two neighboring particles is a common phenomenon in nature. For bioadhesion, a recent report shows that certain

beetles have the capability of walking on a glass surface beneath the water due to the strong effect of the capillary force [15].

1.2 The motivation of the study

Despite its wide-reaching influence, understanding the surface-to-surface interactions between particles with capillary forces present remains challenging.

1. The capillary force rises from a solid-liquid-vapor three-phase interface; each phase has a potential impact on the magnitude of the adhesion. To fully understand the physics behind the capillary forces, a thorough investigation of the physical and chemical properties of liquid, solid, and vapor is a must.
2. The forming of the capillary is dynamic and the origin of the capillary forming can be different from case to case. That is to say, the accuracy of capillary forces modeling depends on the precision of the physical assumptions.
3. The scaling effect may be significant. Capillary forces behave drastically different on the different sizes of particles [16,17].
4. Limited methods of experimental apparatus. More detailed descriptions are presented in chapter 2.
5. Limited methods are available for computational simulations [18–20].

The proper selection of theoretical solutions is crucial for modeling the capillary forces between surfaces. Investigating the fundamental issues behind capillary force has a great impact on numerous potential industrial applications.

As described more in chapter 3, the current theoretical methods have certain limitations:

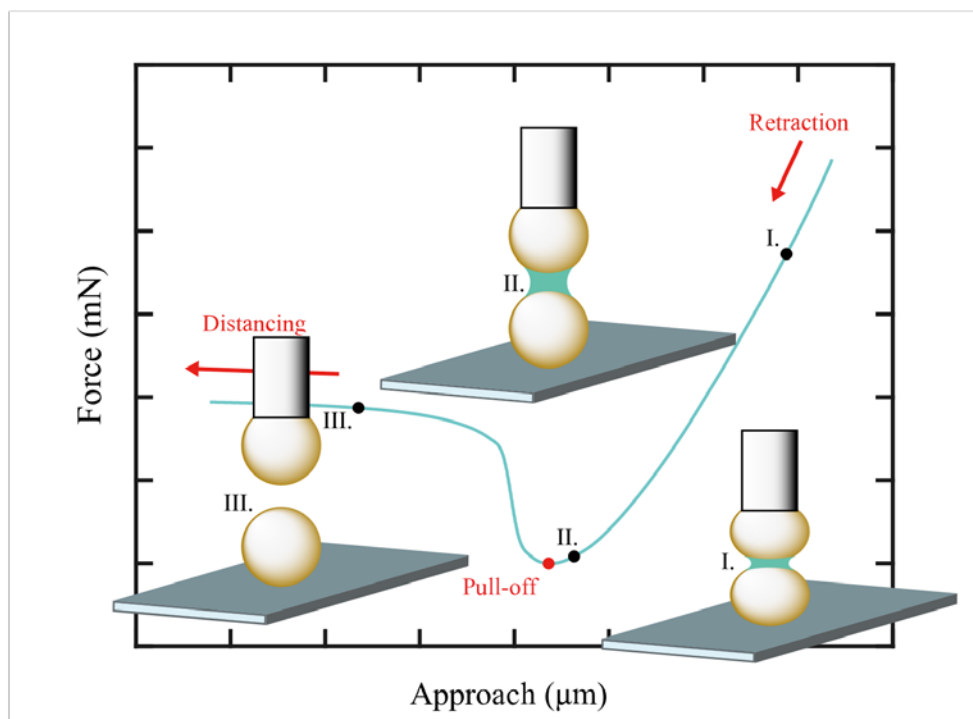
1. The classical adhesive contact theories emphasize heavily on the solid-to-solid surfaces interaction. Their expandability on solid-liquid-vapor three-phase interface needs further investigations.
2. Currently there is a lack of experimental validation on the magnitude of the capillary force in relation to the viscoelasticity property of the hydrogels.
3. The impact of surface roughness on the RH influenced capillary force needs quantitative assessments.

In the current study, the experimental method combined with appropriate theoretical analyses, both analytical and numerical, are presented.

1.3 The aim of this study

The central theme to be described in this thesis is the development of a methodology that combines both experimental and theoretical approaches to facilitate the measurement of capillary force between microparticles (ca. 200-1000 μm in diameter). The experimental investigation covers two major sources of the capillary forming: accumulation of absorbed liquid and liquid condensation. The capillary force caused by the accumulation of absorbed liquid is conducted between two agarose hydrogel microparticles (see Figure 1.1), while the capillary force caused by condensation is performed between two rigid PMMA microspheres under different relative humidity (RH) shown in Figure 1.2 (details of the experimental procedures are presented in section 2.3). The key characteristics are summarized in Table 1.1. A novel experimental setup is built to measure the interparticle capillary force and the corresponding displacements between two particles directly. An incorporated side-view profile visualization system that allows for the investigation of the capillary geometric shape, as well as the deformation of the particles, has been implemented.

Two theoretical approaches have been applied to interpret the force-displacement (F - D) curves. The so-called “energetic approach” is based on the derivation of the total interface energy, while the so-called “Laplace approach” evokes a direct force computation from the meniscus geometry [21].



Pull-off testing for measuring the capillary force between particles.

Figure 1.1 The schematic of the force-displacement (F - D) curve in adhesive contact between hydrogel microspheres measured by pull-off testing. The cyan-blue line is representative of the force versus approach data measured by the novel experimental setup. The measured F - D curve can be divided into three distinct phases: I. two hydrogel spheres had a solid-to-solid contact, the capillary was formed from squeezed liquid. II. Two hydrogel spheres had no more solid-to-solid contact. But they were linked by the capillary bridge in between. III. Two hydrogel spheres were completely separated, the capillary bridge in between ruptured and the liquid was re-absorbed by the hydrogels.

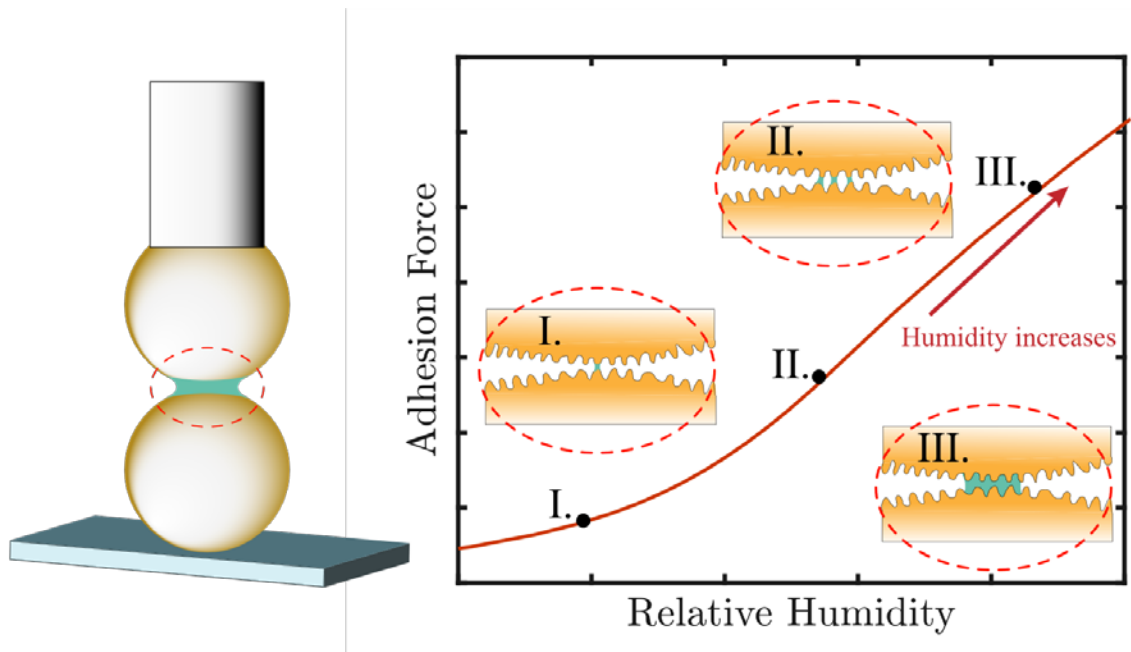


Figure 1.2 The schematic (with exaggerated surface profile) of the surface roughness influences capillary force in adhesive contact between PMMA microspheres under various RH environments. The red line is representative of the measured adhesion force against RH. In the low humidity environment, as shown in I., only a few small capillary bridges formed between the surface roughness asperities. In the medium humidity environment, as shown in II., more capillary bridges formed. In the high humidity environment, as shown in III., smaller capillary bridges merged into one.

| Materials of the particles | Agarose hydrogel | PMMA |
|------------------------------------|---------------------------------|-----------------------|
| Particle diameter | 200-1000 μm | 600-800 μm |
| Material category | Hydrogel | Synthetic polymer |
| Deformability | Soft | Rigid |
| Viscoelasticity | Highly viscoelastic | Unknown |
| Source of capillary forming | Accumulation of absorbed liquid | Liquid condensation |
| Theoretical approach | “Energetic approach” | “Laplace approach” |

Table 1.1 The characteristics of the investigated microparticles.

1.4 The methodology

The methodology of the current study is based on the quantitative characterizations of the capillary force by taking account of potential influences such as surface roughness, particle deformability, and RH. The following parts of the thesis are emphasized in more details:

1. *The experimental setup and the handling of the samples.* This step has the following challenges: The measuring system is delicate and sensitive, and it requires routine maintenance and calibration. The size of the investigated microparticles is small and difficult to handle. The experiments are highly time-related thus must be carried out within a specific short period of time. The hydrogel microparticle samples are not commercially available due to the difficulty in manufacturing and preserving; thus, must be manufactured in the laboratory.
2. *The determination of the mechanical properties of the hydrogel microparticles.* Since agarose hydrogel microparticles were made in the laboratory, mechanical properties such as Young's modulus must be measured independently. These microparticles contained a significant amount of water which was constantly vaporizing during experiments. The vaporization tends to have a much greater influence on smaller spheres due to the higher surface area/volume ratio. Thus, apart from the experiments of the compression between two hydrogel spheres, indentation experiments were performed independently to provide additional data.
3. *The different strategies of using theoretical solutions.* The implementations of different theoretical approaches are selected based on their physical assumptions to ensure the theories can adequately interpret the experiments. The selection of

the “energetic approach” for soft hydrogel particles is due to a few reasons. Firstly, the hydrogels are highly deformable. Secondly, capillary forming is spontaneous under pressure, and the capillary is in a “quasi-static” form. Thirdly, since the capillary forming is not because of the liquid condensation, the shape of the capillary is not governed by the condensation governing equation, the Kelvin equation. The implementation of the “Laplace approach” for rigid PMMA spheres due to the relatively high rigidity of PMMA, the deformation caused by the capillary effect is negligible. Also, because the experimental separation speed is significantly higher than the capillary forming speed; thus, the capillary volume can be assumed constant between the PMMA particles (as described in section 5.3.1).

4. *A comparison of the experimental results with the corresponding theoretical modeling.* If the hypotheses made in theory are validated in the experiments, the numerical values of the undermined coefficients in the constitutive equations thus can be determined. Then, a proper estimation of the material properties of the testing samples can be done.
5. *Further explorations of more practical applications.* If the implemented theory is experimentally proven, it may be applied to predict the capillary force behaviors under similar conditions.

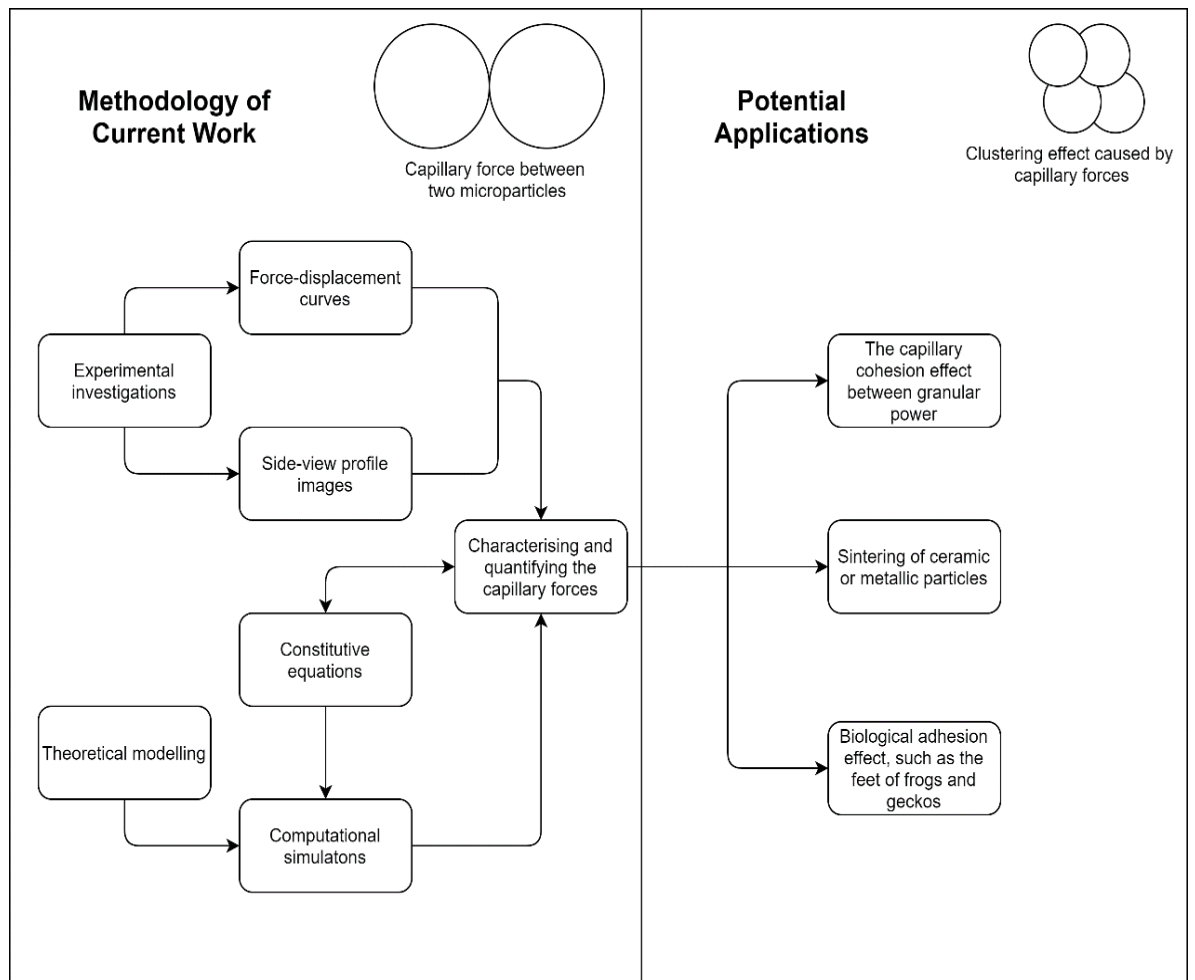


Figure 1.3 A flow chart outlines the methodology of current work and potential applications.

1.5 The structure of the thesis

The rest of the thesis consists of five chapters. In chapter 2, both the previous experimental techniques and the current method are reported in detail. Chapter 3 briefly describes the theoretical backgrounds, and reviews various theories that are adopted in the current study. Chapter 4 presents the experimental data associated with the theoretical analysis of the capillary force between soft micro hydrogel particles. Apart from characterizing the adhesion effect, the impacts of elastic and viscoelastic deformation behavior of the soft hydrogels are also discussed in this chapter. The experimental results for the condensation capillary forces between rigid microparticles under different RH are reported in chapter 5. In this chapter, quantitative investigations on the dynamics of capillary forming and surface roughness influencing adhesion are presented. A direct comparison between the first-order approximation and a numerical solution of the capillary geometric shape is also addressed. Finally, some of the more important conclusions are given in chapter 6.

2 Experimental methods

2.1 Introduction

This chapter is composed of two major parts: The first part discusses some of the previous experimental techniques which have been widely used to measure the capillary force as well as optically observe the meniscus geometric profile. To date, various nano-/micro- force-displacement sensing techniques for measuring the particle-to-particle or particle-to-surface capillary force have been developed. Among these techniques, atomic force microscopy (AFM) surface forces apparatus (SFA), and centrifuge which are the most prevailing, will be described later. Apart from the force measurement, environmental scanning electron microscopy (ESEM), which has been widely used to acquire the images of liquid menisci at micro/nanometer-scale, will also be introduced.

The second part describes the current experimental setup, a novel technique for measuring micrometer-sized interparticle capillary force which combines the force-displacement sensing and the meniscus optical image acquiring.

2.2 Review of the previous methods

Capillary forces between particles and surfaces were firstly characterized by McFarlane and Tabor [22] in the year 1950. They introduced a method of characterizing freely suspended microspheres (diameter ranges from $60\mu\text{m}$ to $200\mu\text{m}$) and flat, vertical surfaces in a controlled environment. Their research reveals that the magnitude of the capillary force increases with the sizes of the contacting sphere

increasing. Through the years, the impact of surface roughness, the lyophilic nature, and the type of condensed vapor have been gradually discovered. With the advancement in the revolution of experimental technologies, more sophisticated techniques such as AFM and SFA have been employed to measure capillary force between solid surfaces.

The meniscus optical image acquiring and force-displacement sensing are equally important in the area of capillary force characterization. Harris and Morrow [23] first imaged acid menisci between steel spheres in the year 1964. The challenge remains in acquiring the image of micro/nanometer-sized menisci until the recent application of ESEM [24].

The fundamental principles of these different techniques are briefly described, and the relative merits and demerits of each method are also discussed in detail in the following sub-sections.

2.2.1 Atomic force microscopy (AFM)

The AFM belongs to the category of scanning probe microscopy (SPM) invented in the 1980s. It was invented by Binnig *et al.*[25] in the year 1986 with the function of measuring the surface topography. The rapid developments of SPM, such as scanning force microscopy (SFM) and scanning tunneling microscopy (STM), have helped researchers to establish important and straightforward tools in the area of adhesion measuring and many industrial applications. One particular advantage of these techniques is the ability to probe the topography and other properties of the sample at high spatial resolution in both liquid and vapor [26].

AFM aims to detect the attractive or repulsive forces between a cantilever tip and the sample. In the setup of AFM (see Figure 2.1), the sample is scanned by the tip mounted onto a cantilever spring. The force between the sample and the tip resulting

in the deflection of the cantilever can be measured by using a laser and a photodetector. Through plotting the deflections of the cantilever at many surface locations, a topographic image of the sample can be resolved. Apart from its application in surface topography imaging, AFM is also used in the study of interactive forces between surfaces, provided that the spring constant of the cantilever has been well characterized. For a typical “force measurement” mode of AFM, when the tip moves towards the sample in the normal direction, the vertical position of the tip and the cantilever deflections are recorded and converted to force against displacement curves.

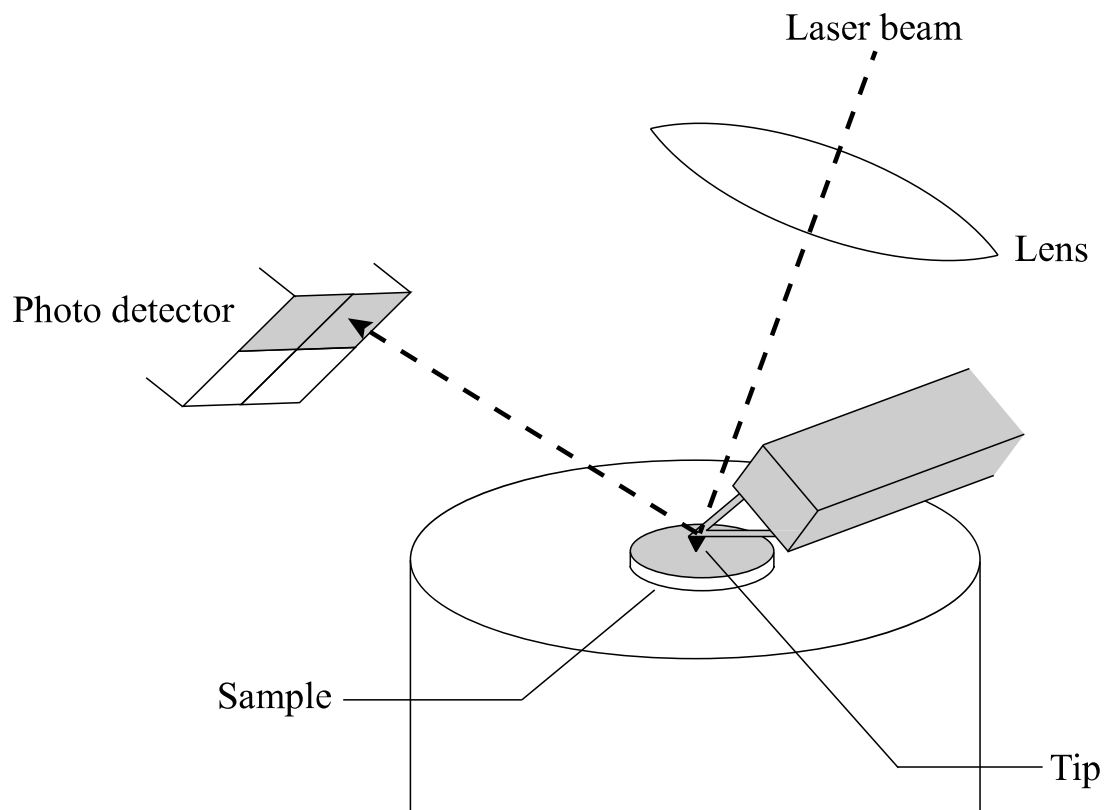


Figure 2.1 Schematic of atomic force microscopy. A laser beam is reflected on the cantilever and received by the photodetector. By knowing the stiffness of the cantilever spring and the obtained laser signal from the photodetector, an accurate force between the tip and the sample can be determined.

Due to its capability in high-resolution displacement measuring, the AFM force measuring technique is becoming more and more important to the studies of surface forces. The introduction of the colloidal probe technique [27,28] makes quantitatively measuring the surface forces possible. For the colloidal-probe AFM, a spherical sphere replacement tip is used to substitute the normal tip and attached to the end of the cantilever. Then the forces between the spherical probe and the contacting surface are measured. By knowing the diameter of the sphere, the surface forces can be determined quantitatively.

Various researchers studied the aspects of experimental capillary forces using AFM over the years. The spherical probe's dimension, lyophilic nature, surface roughness, and deformability all influence the magnitude of the capillary force [29].

AFM studies [30–35] show the impact of the hydrophilicity nature of the surfaces and its dependence on the RH in the surrounding atmosphere. These results suggest that the hydrophobicity inhibits capillary condensation and all the attractive forces can be attributed to Van der Waals force interactions and surface topography. Researches [33,36–39] report the decrease of capillary force because of the surface roughness of the contacting surfaces. They observed the nano-asperities limit the size of the menisci until the RH reaches a critical value where the asperities are fully encompassed by the condensed liquid. Other studies reported the impact of deformation [30,40], ionic diffusion [41,42], and kinetics of meniscus formation [43,44] by using the AFM in their experimental measurements.

The major challenge in AFM measuring technique is to accurately determine the point of contact. When the tip is extremely close to the sample, the effects of electrostatic force, electrical double layer force, and chemical force (e.g. hydrogen

bond) become significant, making the determination of the contact point challenging to achieve without visualizing the side-view profile of the probe-surface.

2.2.2 Surface forces apparatus (SFA)

Another powerful tool of the surface force measuring technique is the SFA. The surface force apparatus allows direct measurement of molecular forces in vapor and liquid at Ångström resolution level [45]. It has been used to measure the physical forces between surfaces for many years, such as adhesion and capillary force, forces due to the surface and liquid structure, hydrophobic interactions, Van der Waals force, and electrostatic force in both vapor and liquid.

In the year 1969, Tabor and Winterton described the first apparatus to measure the forces between surfaces for separations as low as 5 - 30 nm with a 3 Å distance resolution [46]. The classical design of SFA contains two crossed atomically smooth cylinders. The interaction force is measured at the point where the two vertically aligned cylinders are in contact. One cylinder is mounted to a piezoelectric transducer, and the other cylinder is mounted to a spring. The spring constant is known. The separation displacement between the two contacting surfaces is measured optically using multiple-beam interference fringes (see Figure 2.2). Like the atomic force microscopy, the surface forces apparatus is capable of measuring the dynamic interactions and time-dependent interfacial effects.

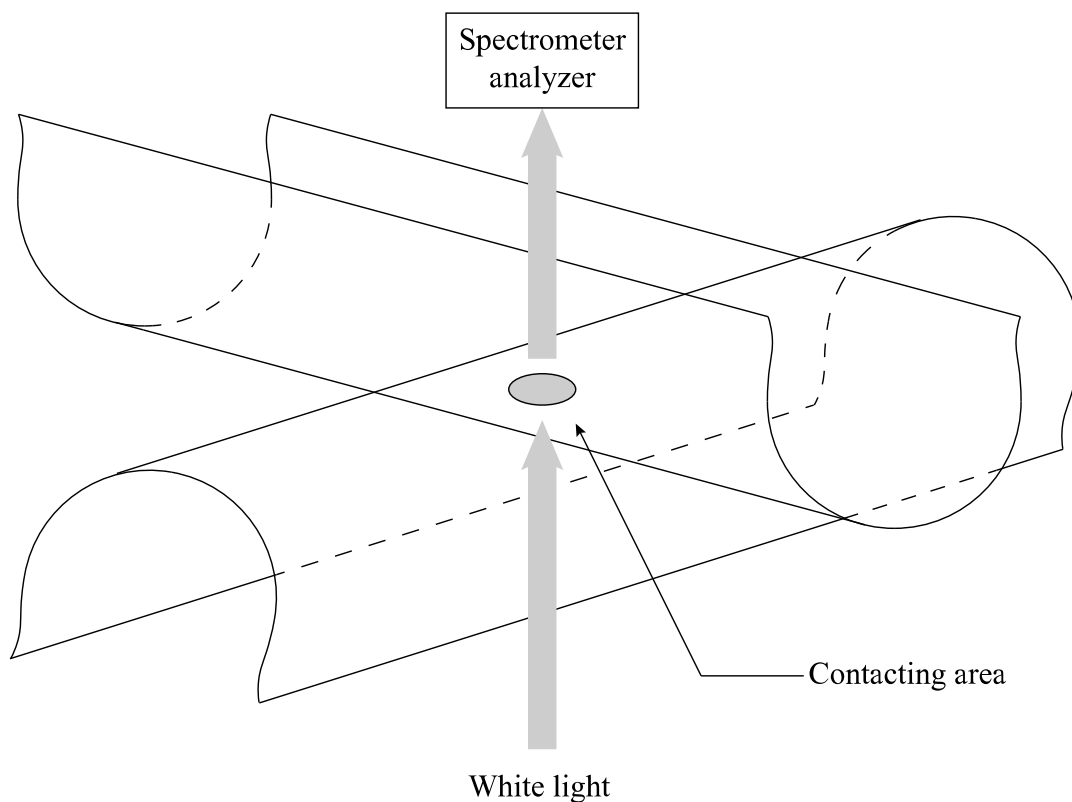


Figure 2.2 Schematic of a typical SFA setup. Two contacting cylinders are aligned vertically. One cylinder is mounted to a piezoelectric transducer, and the other cylinder is mounted to a spring with a known spring constant. A white light illuminates the contacting area, and a spectrometer analyzer captures the image optically. The separation displacement between the two contacting surfaces is measured optically using multiple-beam interference fringes.

Due to its capability of high-resolution force sensing, the SFA plays a crucial role in the experiments of capillary force measurements. The validity of Kelvin's equation (see details in chapter 3) has been confirmed for several liquids in the radii of curvature down to a few nanometers [47,48]. Important reports [16,17,49] done by SFA show that the discrete molecular nature of the liquid does not seem to play a crucial role down to dimensions of 0.8 nm for hexane and 1.4 nm for water. Furthermore, the formation and evaporation of liquid menisci [50–55] and the ionic diffusion effect of the dissolved surface contaminants [56,57] are also studied experimentally by using SFA.

The major disadvantage of the SFA is that it is restricted to substances such as mica and gold which can be coated on highly curved, crossed cylinders. This limitation makes the SFA not suitable for studying the capillary force between soft matters [29].

2.2.3 Centrifuge technique

The centrifuge method was described initially by Boehme *et al.*[58] and the methodology was developed and used by Booth and Newton [59] in the year 1987.

The centrifuge method adjusts the centrifugal detachment force by changing the rotational speed. After the centrifugal force reaches the same value as the adhesion force, the particles detach from the surface. This method is a relatively easy way to obtain the particle-surface adhesion force, especially the adhesion force distribution, compared to other methods [60,61]. The centrifugal force detaching particles from the surfaces is given by

$$F_d = m\omega_j^2 d \quad (2.1)$$

where m is the mass of a single particle, d is the rotational radius, and ω_j is the rotational angular speed which can be adjusted in an ascending sequence to increase the centrifugal force. Multiple particles with different diameters are attached to the

substrate before centrifugation and are counted optically under a microscope. After a round of centrifugation with a certain rotation speed, the number of particles within the designed area of each substrate is counted. At a certain rotating speed, centrifugal detachment occurs and a certain portion $n\%$ of the particles are removed by the centrifugal force. For the detached particles, the centrifugal force is higher than the adhesion force, and for the remaining $(100-n)\%$ of the particles, the centrifugal force is lower than the adhesion force. With several centrifugations at different rotating speeds, a diagram of the cumulative distribution of the detached particles versus the rotating speeds can be drawn. The distribution of the adhesion force thus can be calculated based on the density and the diameter distribution of the particles. The centrifuge technique has been widely applied in the area of granular adhesion [62,63]. Experimental studies on the impact of surface roughness on the adhesion have also been reported [8,64].

The centrifuge method is capable of performing the adhesion measuring experiments in a large number of samples during a relatively short time. However, it is considered as an indirect method of adhesion measurement, and the major disadvantage is that this method cannot sense the displacement between the testing surfaces.

2.2.4 Environmental scanning electron microscopy (ESEM)

Apart from the traditional force-displacement sensing techniques, the acquisition of the optical side-view image profile is equally important to the research of capillary force. Before the application of the ESEM, the image of the meniscus was usually taken by CCD cameras optically on a macroscopic level [65–67].

The application of an ESEM gives the researchers the capability to visualize the dynamic behavior of water meniscus between a tungsten tip and hydrophilic sample on a sub-micrometer level. The ESEM is a type of commercially available Scanning

Electron Microscope (SEM) that allows imaging at high resolution (< 10 nm) in water vapor or any other gaseous environment at a defined pressure ranging from 0.1 to 2 kPa [68,69]. As indicated by the phase diagram of water, it is possible to establish a relative stationary condition of humidity and to wet the sample by selecting an appropriate pressure and temperature (ca. 2 - 20°C) of the testing environment. Hence, ESEM can provide the chance of directly viewing a small water meniscus between the AFM tip and a sample at a much higher resolution level comparing to the traditional optical solutions.

The first attempt at ESEM direct visualization of the dynamic behavior of a water meniscus was made by Michael Schenk *et al.* [26]. Weeks and Vaughn [70] reported their customized ESEM setup mounted on an AFM. By utilizing a special instrument called the Peltier cooling stage for varying the pressure of water vapor within the instrument, they managed to control the humidity enabling images to be collected from 0 to 100% RH.

2.3 A novel technique for measuring interparticle capillary force

Notwithstanding its superiority in force and displacement sensing, the challenge remains for using AFM to directly measure capillary force between microparticles. That is because the accurate alignment between particles is difficult to achieve. Alternatively, SFA has been used to study capillary forces between interacting surfaces across fluid media [71]. SFA is ideally suited for rigid surface-surface interactions, longer-range forces, and surface interactions with long relaxation times, such as adhesive contact between high-viscosity materials. However, SFA-based measurement for capillary force between soft particles is not feasible due to the limitation in its instrumental setup. As mentioned above, the centrifuge technique

doesn't allow to measure displacement directly. There is therefore a need for new advancement in experimental techniques to directly measure the capillary force between both soft and rigid particles. A novel nanomechanical tester has been developed to measure the pull-off force and side-view profiles between two microspheres during separation.

2.3.1 Experimental setup

The system was constructed to measure both the force and displacement between two liquid-bridged microparticles (see Figure 2.3). An ultrasensitive force transducer probe (Aurora Scientific, 406A) was driven by a micro-stepper stage (Newport, UTS 100CC with ESP301 Motion Controller) in *Z*-direction to provide the measurement capability for a force and displacement resolution of 10 nN and 10 nm, respectively. An *X-Y* motorized stage (Prior Scientific, H117P1T4) of 100 nm resolution in both *X* and *Y* directions was used to adjust the two spheres to align axially. A data acquisition system (National Instruments, SCC-68) was incorporated to measure the outputs of both the force transducer and the *Z*-stage simultaneously for recording the force-displacement curves. A computerized control panel was developed based on LabVIEW software (National Instruments, LabVIEW 2016) to synchronize all the stage movements and force sensing. In parallel, an image acquisition system that consists of a long-focal distance objective microscope (Edmund Industrial Optics, VZM 450) with a CCD camera (Sony, XC-ST50CE) was computerized and used to monitor the whole attach-detach procedure between the spheres. The system allowed a zoom ratio of 6.4:1 and magnification of 0.7 – 4.5 times for acquiring the side-view images of the two spheres. The entire measurement instrument was mounted on an anti-vibration table (Wentworth Laboratories Ltd, ATV 702).

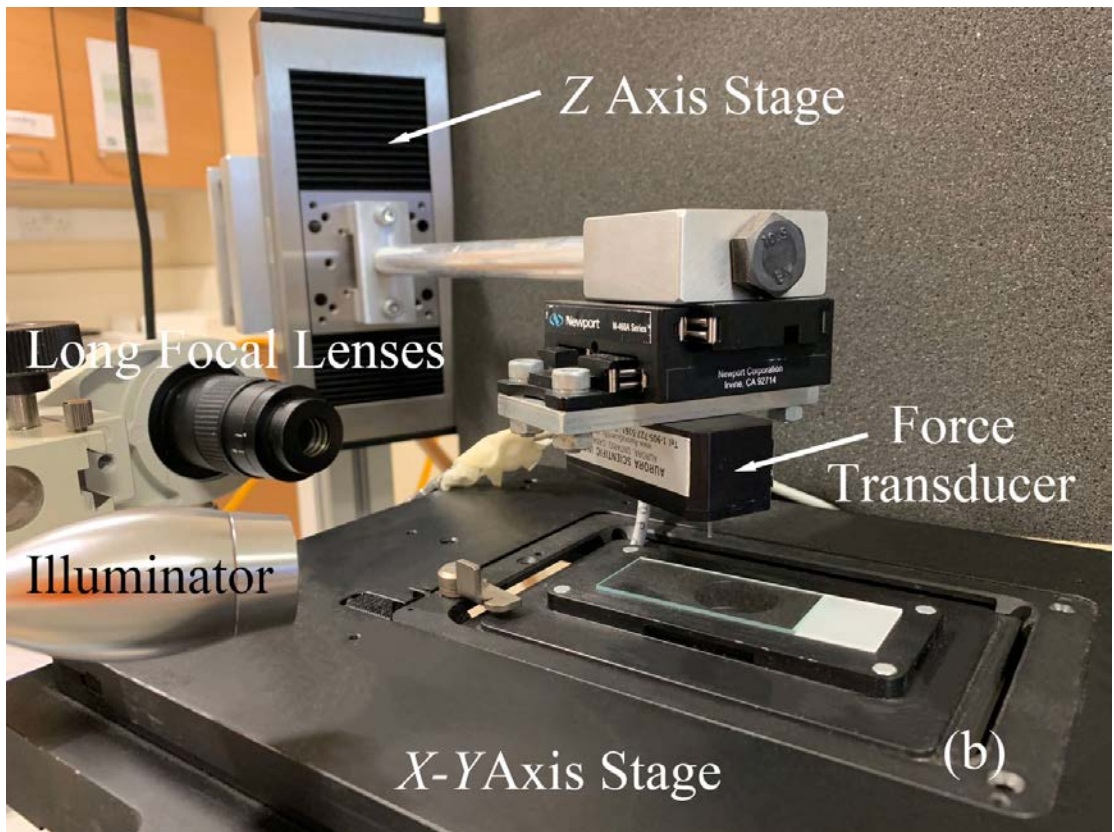
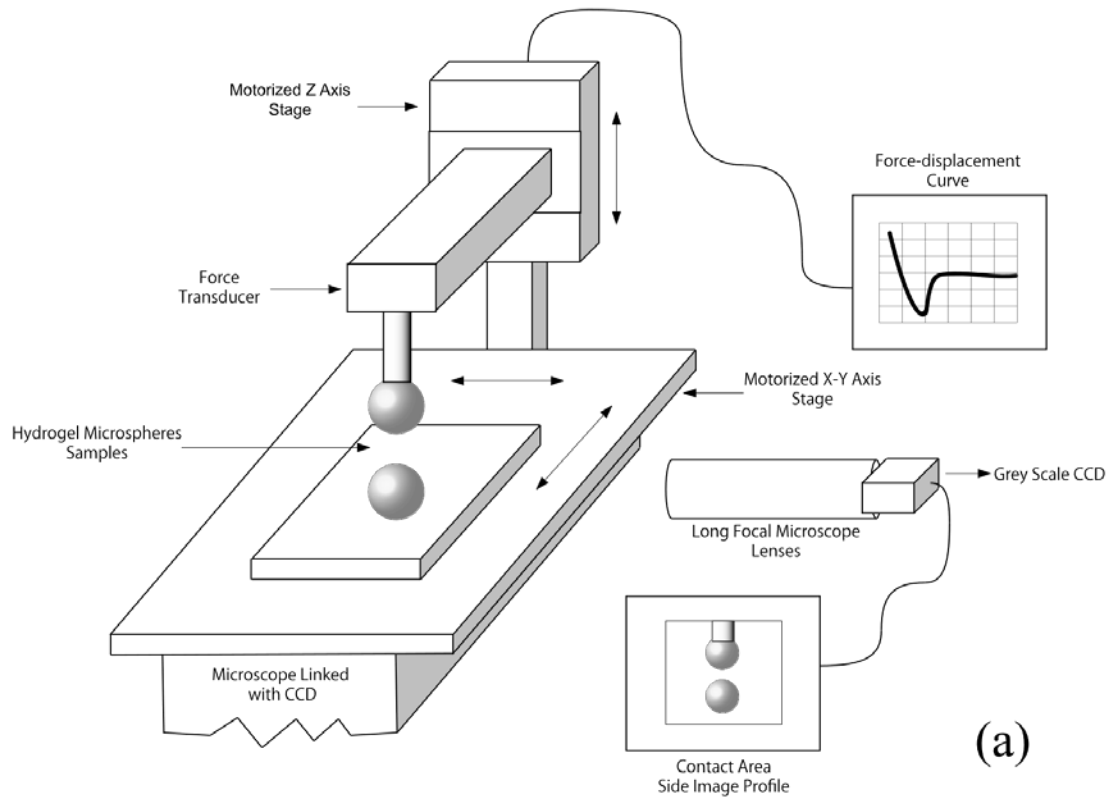


Figure 2.3 (a) Schematic (not to scale) and (b) image of the experimental setup to measure adhesion.

The upper microsphere was glued onto the end of the force transducer probe, driven by the motorized *Z*-axis stage. The lower microsphere was glued onto a glass substrate driven by the motorized *X-Y* stage. The system operates similarly to the principle of AFM in force measurement. As the force transducer brings the upper sphere towards the lower sphere in the normal direction, the vertical position of the *Z*-axis stage and the force signal from the transducer is recorded and converted to force-displacement curves accordingly.

A side-view image acquisition system was incorporated with the nanomechanical tester in the measurements for two-fold purposes. Firstly, the system ensures the pole-to-pole alignment between the two spheres to prevent the distortion of the capillary bridge profile. Any misalignment will not only affect the theoretical analyses but also create an unwanted horizontal force, potentially causing the spheres to slide. Secondly, it is to record the images of the capillary profile during the whole contacting and detaching process for further theoretical validation.

The motorized *X-Y* axis control unit was responsible for the horizontal displacement adjustment with 100 nm resolution in both *X* and *Y* directions. The unit included an Interactive Control Centre Joystick (ICCJ) (Prior Scientific, PS3J100 Control Centre), a high precision motorized stage (Prior Scientific, H117 P1T4), and a controller module (Prior Scientific, ProScan III). During the process of the sample alignment, the image acquisition system was placed on multiple angles. The motorized *X-Y* axis control unit controlled by the ICCJ is capable of moving the lower sphere in a minimum *X-Y* displacement increment of 100 nm.

The force-displacement sensing system was controlled by a host computer using a customized LabVIEW program. Figure 2.4 shows the data flow of the system input and output. The force transducer and its controlling block were connected to a DAQ

(data acquisition device) (National Instruments, 6036E). DAQ device was installed onto a host computer using a PCI connector. The readings of the transducer were in the form of voltage, and it needed to be converted to force accordingly based on the sensitivity of the exact model of the transducer. The displacement data of the Z-axis stage was transferred through a standard 4-pin USB connector to the host computer.

In parallel, the side-view image acquisition system was linked with another computer. Image data acquired from the CCD camera was transferred to a Frame Grabber Device DAQ (National Instruments, 185816g-02) card. The image acquisition DAQ card was installed onto the computer using a PCI connector. The synchronization of the *F-D* measuring system and the image acquisition system was done by identifying the same system timestamp generated by the Internet-based Accurate Global Time Synchronization.

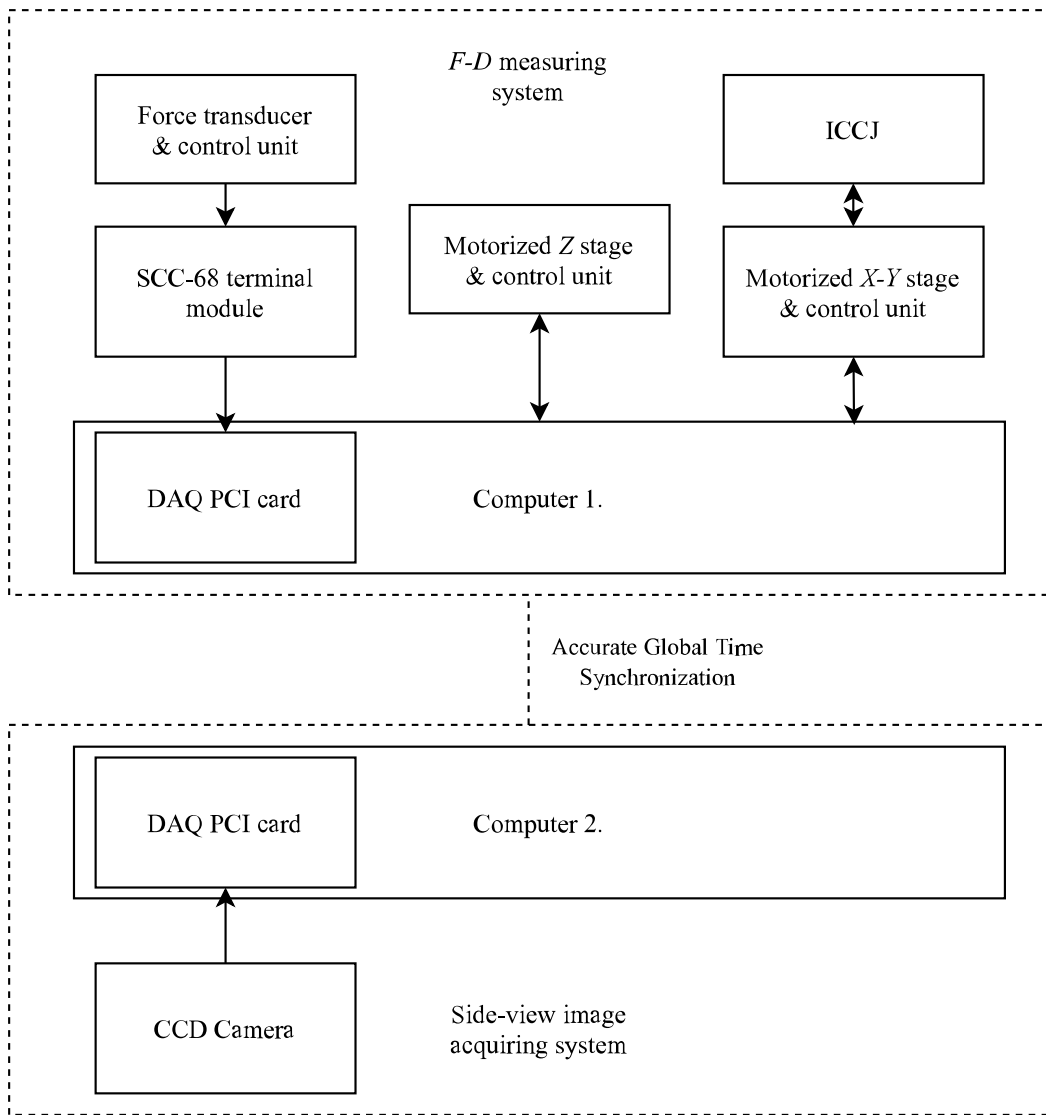


Figure 2.4 Schematic of the system data flow. The arrows indicate the direction of the data flow between different modules.

Under large loads, the force transducer may be overwhelmed and cause unreparable damage. A protocol was therefore written based on the LabVIEW program to limit the movement of the Z-axis stage. When the system detects the force signal reached a maximum threshold of the transducer, the Z-axis stage will stop automatically and reverse the moving direction after a set time of period.

The calibration of the system was done routinely before measurement. The calibration of the force transducer was undertaken by placing a known weight on the end of the transducer probe. Spherical polymethyl methacrylate (PMMA) particles supplied by a commercial manufacturer (EPRUI Biotech Co. Ltd) were measured by a digital analytical balance scale (Sartorius AG, Sartorius 1702). After attaching different microspheres with the known weights to the end of the transducer probe in an ascending sequence, a diagram of the measured voltages against weights can be drawn. A linear regression fitting algorithm written in MATLAB (MathWorks, 2017a) was used to obtain the best fit curve for the acquired data. The fitting shows good linearity as the coefficient of determination R^2 is no less than 0.99, which indicates the force transducer is in an ideal linearity response. The same procedures were performed several times to ensure accuracy. The repeatability calibration of the force transducer was done by calculating the residuals of two output readings under the same weight. The measurements showed all the residuals were within the range of ± 0.1 volts which was approximately 2% comparing to the maximum output, suggested the repeatability of the force transducer can be trusted.

The calibration of the side-view image system was undertaken by photographing a micro-ruler under a set of magnifications as a reference scale. The image was then processed by an image processing software (ImageJ, v1.51), establishing a relationship between pixels and the known distance. After the proper calibration of the

side-view image acquisition system, the displacement can be measured directly by counting the number of pixels between two sets of points.

2.3.2 The major merits of the current system

Compared with others, there are some major advantages of the current method which are listed as below;

1. The method gives a continuous force-displacement curve for both the loading and unloading.
2. The system allows the direct measurement of interparticle capillary force. Previously mentioned techniques like AFM and centrifuge technique usually only operate between particles in contact with a substrate due to the limitation of the experimental hardware setup.
3. The method can be applied to both rigid and soft materials.
4. The system is cable of recording the displacement not only by the Z-axis stage but also optically from the side-view acquisition system. This will greatly improve the capability of determining the exact contacting point between the particles.
5. The magnitude of the work of adhesion can be properly estimated by adopting appropriate analysis to the “pull-off” force measurement (see chapter 4).

Apart from the above advantages, an outstanding feature of the current experimental approach is that with an installation of a humidity control chamber, the system can be modified to measure F - D curves between particles due to the capillary force caused by the liquid condensation (see chapter 5). As mentioned before, it is worth pointing out that it is not possible to control the humidity in most centrifuges [61]. Similar

humidity control setups have been used in AFM and SFA over the years. These instruments were applied for the particle with a diameter range from several to a few hundred nanometers [24,29,72]. However, the direct measurement of $F-D$ curves of the condensation capillary force impact between particles is rarely done on a micrometer level.

It is obvious that, although the force and displacement sensing resolution and the sample sizes of the current novel setup are different from the instrument like AFM and SFA, their general working principles are similar.

3 Theoretical backgrounds

This chapter reviews some of the fundamental concepts of capillary and the theories available for the description of the capillary force between both soft and rigid microspheres.

3.1 Introduction of the capillary force

Capillary force refers to an attractive force caused by liquid menisci between two lyophilic solid surfaces. A vivid example was given by Halsey and Levine in their article “How Sandcastles Fall” [73]. In their research, they demonstrated the impact of how capillary force significantly affects the stability of sandpiles. Everyone who has been at a beach knows that dry sand flows easily. However, to build a sandcastle the sand must be humidified. The wetted sand can be shaped into different forms is because the sand particles adhere to each other. This strong adhesion is the so-called “capillary force”, which is caused by the liquid menisci forming around the contact areas between the neighboring particles. “Meniscus force” and “capillary adhesion” are also referred widely to the same cohesion effect. Fisher [74] and Haines [75,76] were the first to realize the significance of the capillary force in the 1920s. Over the years, it has been demonstrated that when dealing with the granular powders, the effect of the capillary force needs to be taken into account [77–79]. There are two major ways of meniscus forming; one is the capillary condensation, and the other is the accumulation of absorbed liquid. In many cases, capillary force dominates over other surface forces when two hydrophilic surfaces are in contact under ambient conditions.

It also has to be pointed out that the capillary forces are not only caused by the liquid menisci in the vapor environment but also might be caused by the menisci of one liquid in another immiscible liquid [80,81]. Due to the complexity of modeling capillary force, it is worth learning the principle of capillary force and review some of the well-known theories.

3.2 Liquid surface tension: the origin of the capillary force

The capillary force is generated from the pressure difference between inside the meniscus and outside, which is caused by the liquid surface tension. The explanation of the “liquid surface tension” is often given on a molecular basis. The molecules inside the liquid encounter both attractive and repulsive forces in all directions due to their neighboring molecules. Since the repulsive forces have a much shorter range than the attractive force and only become significant at an extremely high external pressure [82], the attractive forces usually dominate. The interactions between a given molecule and its nearest neighboring molecules lead to a reduction of its potential energy [83]. This type of interaction raises cohesion among the molecules also leads to adhesion between molecules of that liquid and any solid bounding surface. The molecules around the liquid-vapor interface region have a smaller number of immediate neighboring molecules as the density of the vapor is considered much smaller than the liquid. Thus, their potential energy is not decreased as much as in the interior of the liquid. In other words, the molecules near the vapor-liquid interface experience a relatively weaker force from the vapor region above the surface. Thus, these molecules will encounter an average force that is normal to the vapor-liquid interface, pulling them back into the bulk of the liquid. This means necessary work or energy is required against this type of attractive force from the interior to the surface. The higher energy

requirement suggests that the molecules near the vapor-liquid interface possess greater potential energy compared with those inside the bulk of the liquid. This is characterized as the surface tension, which is the interfacial potential energy divided by an area, the unit is J/m^2 . Equivalently, a force per length definition can be applied, resulting the unit of surface tension to be expressed as N/m [83–85]. Simply speaking, the existence of the surface tension has two reasons [86]:

1. The forces between neighboring molecules have a short range of action.
2. The matter/molecule density is considerably smaller in the gas phase comparing to a liquid.

Every system tends to move towards a state with the minimum potential energy, which means the surface of a liquid will tend to contract. This mechanism results in the concave surface of the liquid, such as the shape of a droplet. The liquid interface is often modeled as an “elastic skin”, which is similar to the surface of a rubber balloon [87]. Thus, if the vapor-liquid interface is curved rather than a planar surface, the resultant surface tension force normal to the interface will create a pressure difference across the interface. The pressure on the concave side of the interface is greater than the other. This pressure difference Δp can be described by the Young-Laplace equation as [88]:

$$\Delta p = \gamma_{LV} \left(\frac{1}{r_1} + \frac{1}{r_2} \right) \quad (3.1)$$

where γ_{LV} is the interfacial surface tension, r_1 and r_2 are the two principal radii of the curvature, respectively. When the capillary forms between two surfaces, Δp rises an attractive force pulling the neighboring surfaces together. This cohesion effect is the so-called capillary force.

In practice, capillary force may occur in an elastic structure when its restoring ability is unable to fully overcome the interfacial attraction induced by liquid surface tensions [89]. The geometry of a steady capillary bridge surface is described by the aforementioned Young-Laplace equation, in which the mean curvature of this surface is constant in the absence of gravity. Solutions of the Young-Laplace equation for the axisymmetric capillary bridge have already been reported in various researches [90,91]. These approaches give the meridional profile for the capillary bridge surface, which are formulated in terms of elliptic functions. Approximations have been developed to simplify these methods over the years. One common approximation is the toroidal approximation in which the meridional profile of the capillary bridge is described by an arc (part of a circle). The accuracy of the toroidal approximation has been investigated in various studies [91,92] and especially by Lian *et al.* [93], who also compared various ways of evaluating the capillary force with the toroidal approximation [94].

3.3 Liquid-condensation capillary

The most common scenario of capillary force is when the capillary forms spontaneously between two hydrophilic surfaces in the humid air. It is well known that the physical behavior of liquid in confined spaces differs from that inside of a liquid bulk [95–98]. The term “chemical potential” which refers to a form of potential energy that can be absorbed or released during a phase transition or chemical reaction is often used. When at the boiling point for a given pressure, the liquid chemical potentials are the same for the vapor phase and liquid phase. However, if a liquid whose potential for liquid phase is less than its own value for the vapor phase (i.e., temperature below

boiling point at a given pressure) at saturation, it will tend to condense and form into a liquid capillary [99].

Several classic and advanced theories have been proposed over the years. The most famous ones are the Kelvin equation and its variants. The Kelvin equation forms the basis of critical nucleation theory, and it is widely used in the interpretation of a variety of phenomena such as adhesion, the enhanced solubility of small particles, and the retention and transport of liquid in porous materials [100]. The Kelvin equation assumes that undersaturated vapors will condense into menisci between two surfaces of sufficiently small dimensions. This assumption gives the equilibrium mean radius of curvature r_m of a liquid-vapor interface in terms of the actual vapor pressure p and the saturated vapor pressure p_s . Kelvin equation can be applied to not only liquid droplets, but also the vapour bubbles and capillary-held wetting liquids.

The Kelvin equation is used extensively to mathematically describe capillary condensation in both theoretical modeling and experimental validations. It is frequently employed in the prediction of capillary condensation occurred under different conditions and in the evaluation of the forces that are exerted on the absorbent by condensates, the thickness of adsorbed layers [101]. Despite its frequent use, the Kelvin equation is based on many assumptions that are not always valid for certain scenarios. For instance, the most fundamental assumptions for the Kelvin model are that the applied liquid is incompressible and the vapor is ideal; the surface tension and the molar density of the liquid are both independent of the gap size between the two surfaces. However, these assumptions are not necessarily true, especially for liquids confined in a nano-sized gap [102–104]. Furthermore, because the Kelvin equation is based on macroscopic thermodynamics for a liquid and vapor in equilibrium, its own

accuracy when applied in hysteretic isotherms is dependent mainly on which non-equilibrium branch has been selected for the calculations [96,105].

It has been experimentally proved that the Kelvin equation and its variants are valid in gaps with radii as small as 4 nm [106,107]. However, further experiments show that the assumption is no longer valid when the gap size decreases to 2 nm [104,108] or below.

3.4 The capillary force between soft particles

The Johnson-Kendall-Roberts (JKR) [109], Derjaguin-Muller-Toporov (DMT) [110] model, Maugis model [111] for contact under normal loading have been developed based mainly on solid-solid interactions (mainly Van der Waals forces). However, for contact in a humid environment or contact between two hydrogel spheres, where a capillary may be present, the capillary force with a longer force range usually dominates. This topic was firstly addressed by Fogden and White in their study in 1990. Their work was followed by Maugis and Gauthier-Manuel [112] who included capillary effects within the framework of their energy-based fracture mechanics theory. Since then, more quantitative descriptions of the classical contact theories applied to the capillary force between solid surfaces have been widely reported, particularly with soft materials. This is because the classical adhesion theories like JKR and Maugis model are relatively insensitive to the natural origin of the adhesion itself [113], and their capability of predicting the elastic behavior of soft matter with exceptional accuracy. These methods are often referred to as the “energetic approach” due to their implementation of the interfacial energy concept [114]. This section gives a brief review of some of the classical contact theories and their applications on the contact between soft materials.

3.4.1 Classical contact theories

Hertz [115] established his famous theory of contact in 1882. He assumed a continuous pressure distribution for non-adhesive contact between the two contacting surfaces. The two contacting bodies were assumed to be pure elastic with a normal, non-conformal, and frictionless surface. Later, adhesive interactions between the surfaces were brought into consideration by Johnson *et al.* in their JKR theory. The JKR theory modifies the Hertz theory by including an auto-adhesive effect which is distributed evenly across the contact region. Alternatively, the DMT theory presented the adhesive contact model which takes into account the long-range intermolecular forces outside the contact region. Their theory was further detailed in the references [116,117]. On the first look, the DMT theory seems to contradict the JKR theory directly. Tabor [118] addressed this problem by defining a dimensionless parameter μ_T representing the ratio between the gap outside the contact zone and the equilibrium distance between atoms. This parameter established the range of applicability of the two models and suggested that the interactions within and outside the contact zone needed to be accounted for. Furthermore, Müller *et al.* [119,120] developed their numerical model based on a Lennard-Jones-type potential, demonstrating a continuous transition from the DMT region to the JKR region as Tabor parameter μ_T gradually increases. Later on, Maugis [121] presented his solution using Dugdale approximation. Johnson and Greenwood reported an adhesion map [122] demonstrating the boundary conditions of these theories. One thing that needs to point out that the aforementioned theories are all based on the principle assumptions of Hertz theory. More advanced models [123–126] discussing scenarios where adhesion combines with friction, viscoelasticity in detail are beyond the scope of this thesis.

3.4.2 Applications of the models

The phenomenon of capillary force between soft materials is ubiquitous in nature, ranging from granular powder [127,128] to biological cells [129,130]. These interesting cases inspire numerous researches over the years. One motivation comes from the studies of bio-adhesion of insects and tree frogs to the surfaces [131–135]. These researches show that there is clear evidence indicating that the main adhesive force in smooth adhesive pads, which exist in certain insects and tree frogs, stemmed from capillary and the magnitude of the adhesion scales with the area of these pads. Recently hydrogel particles have been widely used in food, pharmaceutical, and biomaterial industries [136]. Since these particles typically contain a high percentage of water, the capillary force plays an important in their adhesive contact [137,138].

Applying the classical contact theories to the capillary force between soft contacting surfaces has seen a significant increase since Fogden and White laid their foundations. They recognized the long-range characteristic of the capillary force comparing to the solid-solid adhesion as short-range interaction and developed their capillary force model based on the JKR model for elastic deformation. Maugis and Gauthier-Manuel extend that model to the DMT and the JKR-DMT transition [112]. The model is restricted to small contact radii and does not apply to extremely soft materials such as hydrogels. Xu *et al.* [139] presented a modified Tabor parameter for the JKR-DMT transition in the presence of a liquid capillary. Xue and Polycarpou calculated the effect of elastic deformation due to the capillary force numerically[140]. They assumed the shape of the contact between two contacting spheres is given by the Hertz model and adjusted the capillary effect by setting a constant curvature boundary condition. Butt *et al.* [141] presented a solution with a similar approach but derived an analytical expression for the capillary force addition with finite element simulations.

3.5 The capillary force between rigid particles

An alternative approach for modeling the capillary force between particles is to directly implement the Kelvin equation and Young-Laplace equation, which is often known as the “Laplace approach.” Researchers usually prefer this approach when dealing with particles when their elastic deformation can be considered negligible. This preference is due to the fact that rigid materials are much harder to deform; thus, the elastic deformation effect caused by capillary force is usually considered to be negligible. This section reviews some of the celebrated theories to calculate the capillary force between rigid particles and their applications.

3.5.1 Young-Laplace equation and its variants

The capillary forces acting between two rigid particles are usually categorized by two factors: First, the direct action of the surface tension of the liquid around the periphery of the meniscus which acts as a cohesion force pulling the particles together. Second, the pressure inside the meniscus is reduced comparing to the outer pressure caused by the capillary pressure Δp given by the Young-Laplace equation [74,75]. This pressure difference acts over the cross-section area of the meniscus, which also attracts the two particles towards each other [142,143]. The force existing around the periphery of the meniscus is often neglected in the treatment of capillary forces because it is typically much smaller than the force acting over the cross-section area of the meniscus for lyophilic surfaces [144]. Hence, the accurate quantification of the capillary force would depend on the modeling of the capillary geometric shape. The most common assumption is the aforementioned toroidal approximation. Applying the toroidal approximation leads to a much simpler solution of the capillary geometric shape; however, several limitations must be addressed. The implementation of the

toroidal approximation implies that the surface tension effects dominate, and the gravitational effect is negligible. This suggests that the toroidal approximation can only give relatively accurate predictions towards smaller capillaries. Moreover, even in the absence of gravity, the Young-Laplace equation predicts a different shape rather than a simple circle [91]. This toroidal approximation leads to a varying mean curvature of the capillary bridge surface, which is inconsistent with the Young-Laplace equation. Based on numerical solutions of the Young-Laplace equation, Erle *et al.* [90] have shown that for an identical volume of the capillary and the separation between the spheres, two solutions for the meridional profiles may exist. The distinctions between the two solutions are the different predictions of the rupture distance.

Furthermore, surface heterogeneity is often neglected in the calculation and discussion of capillary forces. Solid surfaces usually have defects or different variations in chemical compositions, which leads to an inhomogeneous contacting area, potentially influencing the formation of the capillary [145].

3.5.2 Applications of the models

The direct implementation of the Kelvin equation and Young-Laplace equation simplifies the modeling of capillary forces, makes some aspects of the problem much approachable for further investigations. For example, a series of researches took a deep look into the influences of surface roughness. The surface roughness of the particles is often a controlling factor in the strength of adhesion because it determines the degree to which two adhering surfaces complement each other [24,145]. The lower the complementarity between the two surfaces, the lower the adhesion force. Because the actual area of contact has decreased. Thus, the variations of menisci sizes under different vapor pressures play an important role in the capillary force magnitudes. The

effect of surface roughness mitigates as the sizes of menisci between surface asperities increase. Capillary forms under low [36,78,146] and high vapor pressure [145,147] are reported with experimental validations.

The effect of particle shapes and sizes is another aspect. Butt *et al.* [24] give a thorough review of capillary forming between various shapes of configurations using toroidal approximation. The review reported that when considering geometries other than spheres, the capillary force can change fundamentally. Firstly, not only the strength but also the distance dependency changes. Secondly, the vapor pressure has different impacts on different geometries. For example, if we assume the contacting surfaces are completely smooth, for the spherical contacts, the capillary forces are almost independent of the differences of vapor pressure. While for other geometries, such as capillary between a cylinder with a conical end and a plane, the capillary forces might change drastically. Colak *et al.* [148,149] used AFM with tips of different sizes and shapes experimentally discovered that sharper tips are more susceptible to local surface roughness than larger, flat ones.

4 Capillary force in adhesive contact between hydrogel microspheres

4.1 Introductions

Classical contact mechanics and adhesion theories such as JKR[109] and DMT[110] provide a fundamental understanding of the contact and adhesion between surfaces. Despite the fact that most theories are developed under the assumption of solid-solid contact, previous studies [112,150] showed that they could be potentially applied to complex contact situations such as a solid-liquid-vapor interface. Recently, extended contact theories for the complex contact are in demand, partly because of increasing interest in soft polymeric microparticles [151,152] and biological cells [153], which are characterized by small dimensions and relatively low Young's moduli. Recent theoretical and computational studies shed light on how capillary force influences the adhesive contact between two rigid particles [154] as well as a rigid particle to a soft substrate [155,156].

Despite theoretical studies extensively reported, experimental measurements of capillary force between hydrogel particles remain challenging because interparticle forces typically range from a few nanonewtons (nN) to hundreds of micronewtons (μN) depending on the particle sizes. Ultrasensitive instruments for force-displacement measurement are therefore essential for experimental investigations of the capillary-dominant adhesive contact between two hydrogel microspheres. As introduced in section 2.2.1, AFM has long been recognized as a powerful technique to study capillary force thanks to its capability in measuring force-displacement on

nanoscale objects or surfaces. Extensive AFM-based investigations in various effects, such as hydrophilicity [157], RH [158], ionic diffusion [159] and surface roughness [160], influencing the capillary forces between the nanoparticle and solid surface have been reported. Notwithstanding its superiority in force and displacement sensing, the challenge remains for using AFM to directly measure capillary force between soft microparticles because accurate alignment between the particles is difficult to achieve. As introduced in section 2.2.2, SFA has alternatively been used to study capillary forces between interacting surfaces across fluid media [71]. SFA is ideally suited for rigid surface-surface interactions, longer-range forces, and surfaces interactions with long relaxation times such as adhesive contact between high-viscosity materials. However, SFA-based measurement for capillary force between soft particles is not feasible due to the limitation in its instrumental setup. There is therefore a need for new advancement in experimental technique to measure the capillary influence in adhesion between soft particles. In this chapter, I demonstrate how to apply the novel nanomechanical tester (as described in section 2.3.1) to measure the pull-off force and side-view profiles between two hydrogel microspheres during separation. Contact theories such as JKR and generalized Hertzian theories have been applied to interpret quantitatively the capillary-dominant adhesion. The comparison between the experimental measurements and theoretical predictions facilitates the determination of the work of adhesion and Young's modulus of the particles.

4.2 Experimental section

4.2.1 Fabrication of hydrogel microparticles

Hydro-gel spheres were made of 1.5 weight % agarose (Sigma Life Science, low gelling temperature agarose, A9414) solution. The agarose powder was suspended in deionized water at 20°C and heated to 85°C in a water bath (Grant Instruments Ltd, JB Nova Unstirred JBN12) to allow the powder to fully dissolve. The solution was then dispersed through a spray nozzle into vegetable oil (Flora, pure sunflower oil, 392803) to produce micron-size particles that are essentially spherical due to surface tension. Depending on the spray velocity and nozzle dimension, the range of particle sizes lies between 200 to 1000 μm in diameter.

4.2.2 Preparation of hydrogel disk

A disk-shaped sample of agarose gel was prepared for the indentation test to independently characterize Young's modulus of the gel (see section 4.2.4). Fully-dissolved agarose solution at 85°C was poured into a petri dish of 5 cm in diameter and 2 cm in thickness, respectively. The petri dish was then cooled in a humidity-controlled chamber (ibidi GmbH, Gas Mixer M-323) with 80% RH under room temperature (20 °C) until the solution was solidified to form the gel sample.

4.2.3 Capillary force measurements

The approach to characterize interparticle capillary force was based on the direct measurement of the separation force-displacement curves between two liquid-bridged particles. One agarose sphere was selected and attached on the flat surface of a force transducer probe, which was driven by a micro-stepper stage. The second sphere was firmly glued on a flat glass substrate to prevent it from sliding throughout the whole contact process. The *X-Y* motorized stage was used to ensure the two poles aligned

axially. The top sphere was lowered at a constant speed ($20\mu\text{m/s}$) by the Z -stage till a ca. $25\mu\text{m}$ approach (the compressive displacement at the pole of deformed spheres) was reached to form a finite solid-solid contact. After 3 seconds contact time, the actuator was then retracted at the same speed to shrink the contact area till ‘pull-off’. The force-approach curves were measured and recorded using the data acquisition system. The grayscale CCD with a long focal lens was used to capture the simultaneous side-view profiles (see Figure 4.1(a)).

Agarose gel has been well recognized as homogeneous and isotropic material which contains a high percentage of water (ca. 98.5% W/W for the current spheres). When the hydrogel spheres were brought into intimate contact in air, a compression developed at the contact circle deformed the spheres and raised the elastic energy stored in the viscoelastic medium of agarose. The compression also squeezed a minute amount of water from the saturated spongy materials, leading to a meniscus at the annulus around the contact circle.

Measurements were repeated for spheres with a range of dimensions as well as a range of loading-unloading speeds ($10 - 30\mu\text{m/s}$). At least three replications of the force-approach curve have been measured for each dimension at each separation speed. During the entire separation period, side-view images of the two spheres were acquired dynamically by the CCD camera. The captured images were then processed by MATLAB (MathWorks, 2017a) using an edge detection algorithm to determine two principal radii r_1 and r_2 of the meniscus (see Figure 4.1(b)).

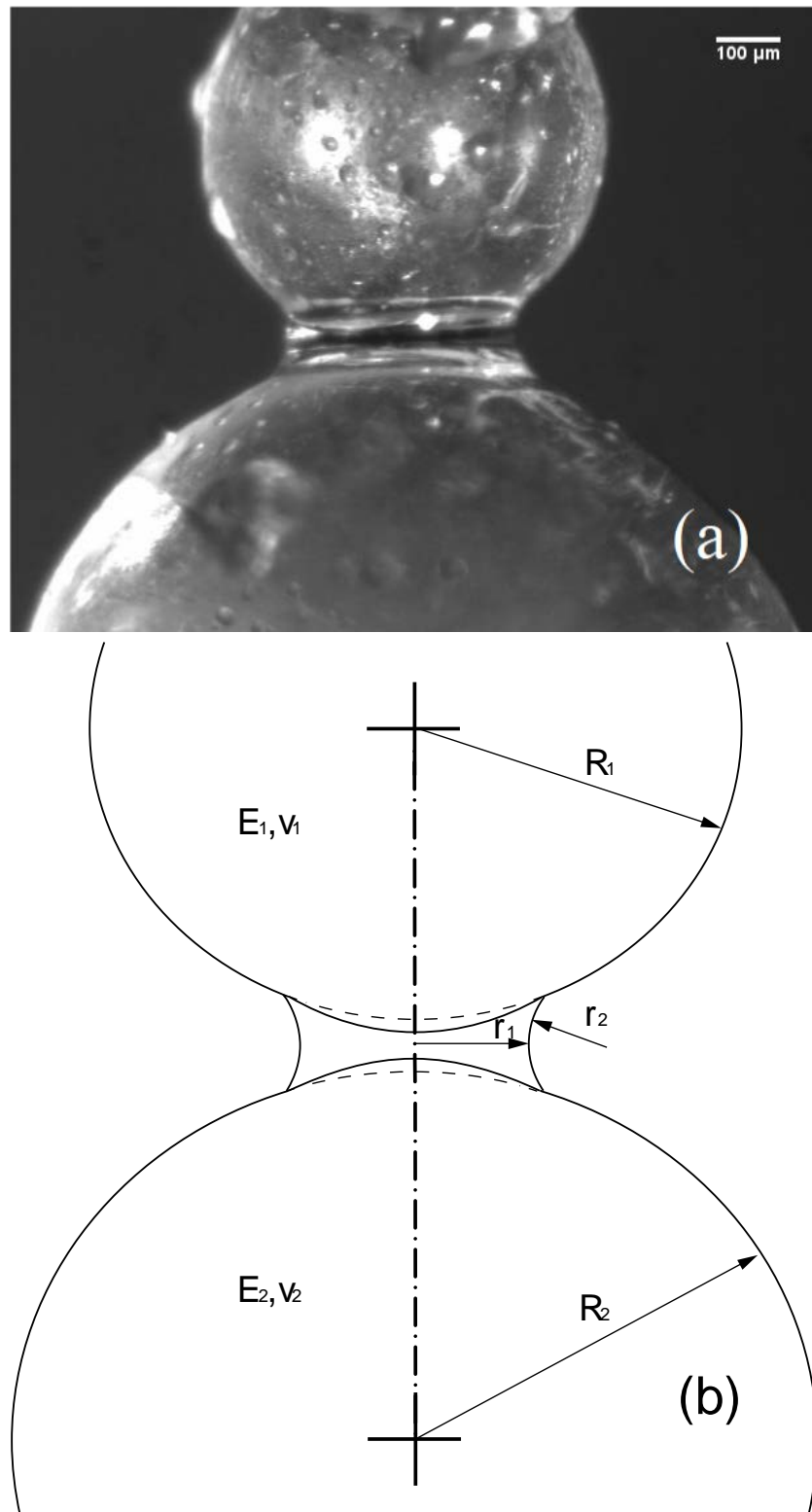


Figure 4.1 (a) Micrographs and (b) schematic of the liquid bridge formed between two agarose hydrogel spheres.

The acquired images (see Figure 4.2) show the liquid re-absorption process is swift and the liquid re-absorbed fully within ca. 0.166 s after the capillary bridge was broken. The sphere volumes were measured based on the captured images before and after each group of experiments performed; the volume change during the measurement period due to liquid vaporization was found to be negligible. During the entire measurement period, an illuminator was used to illuminate the two spheres for enhancing the acquired image qualities.

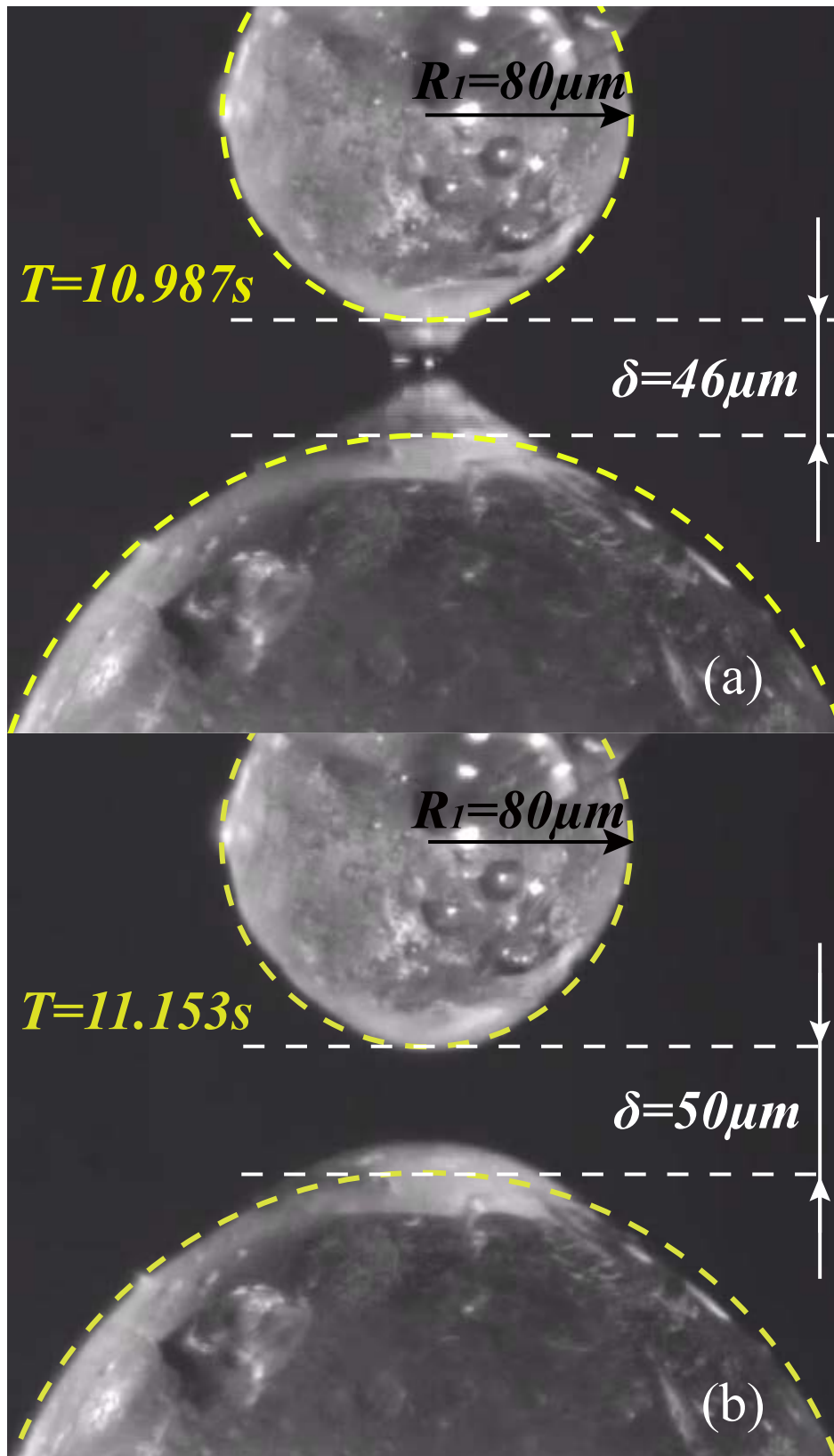


Figure 4.2 The side-view images acquired at a constant separation speed of $20 \mu m/s$, show (a) the capillary breakage and (b) the liquid re-absorbed completely after 0.166 s.

4.2.4 Indentation testing

For an independent characterization of the agarose's elasticity, an alternative setup was constructed based on the same force-displacement sensing platform mentioned above to perform indentation testing of the materials. A PMMA sphere with 800 μm in diameter was installed on the tip of the force transducer to serve as a spherical indenter. Young's modulus of the PMMA was selected to range from 1800 to 3100 MPa, that is, about 10000 times higher than those of agarose gel, to ensure the deformation of the indenter negligible during indentation. The PMMA bead was then lowered at a constant speed (20 $\mu\text{m/s}$) to indent the disk-shaped gel sample up to 30 μm (see Figure 4.3). The force-indentation depth curves were measured and used to estimate the values of Young's modulus for cross-validation of those of the agarose particles measured by the aforementioned pull-off test.

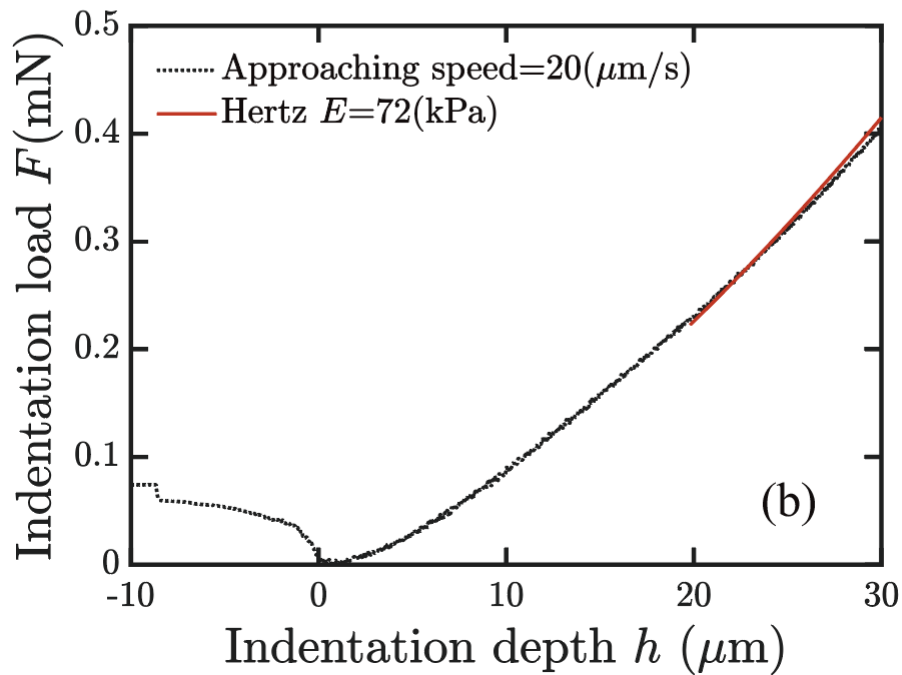
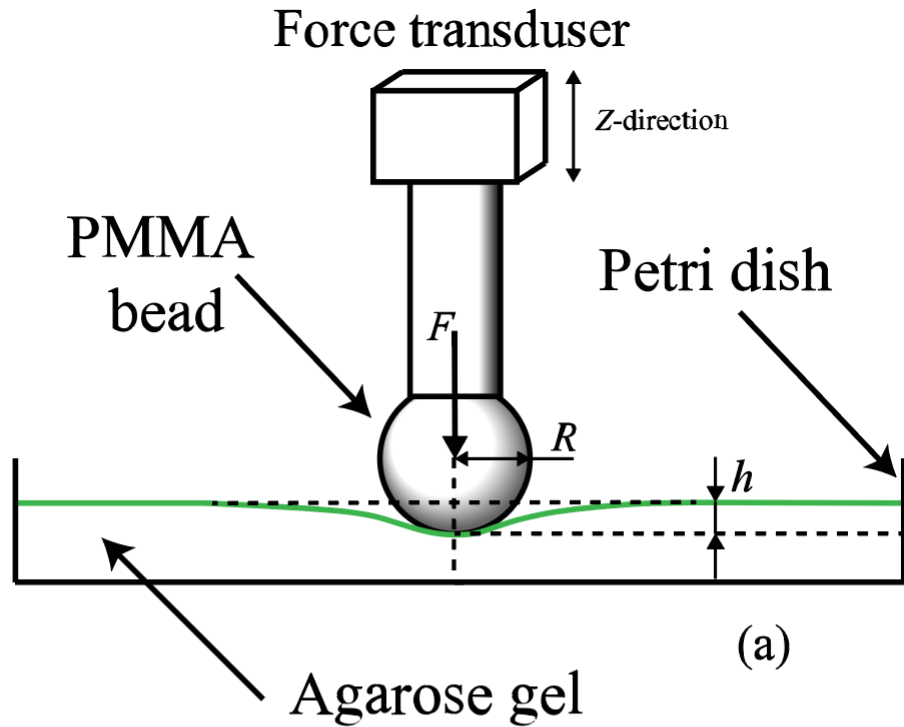


Figure 4.3 (a) Schematic of the alternative spherical indentation test for measuring Young's modulus of the agarose gel independently (not to scale). (b) Comparison of theoretical and the experimental indentation force F versus indentation depth h , $F(h)$ curve (measured at a constant loading speed $20 \mu\text{m/s}$). Young's modulus was 72 kPa for the prediction of Hertz theory with least-square fitting.

4.3 Theoretical basis

4.3.1 Contact mechanics and adhesion

On the theoretical front, the classic Hertz contact theory describes the non-adhesive contact between two deformable elastic spheres [115]. When a compressive contact normal load P is applied to two elastic spheres along the aligned axes, it creates a circular radius a and an approach δ , Hertz contact theory requires

$$\delta_{\text{Hertz}} = \frac{a_{\text{Hertz}}^2}{R}, \quad (4.1)$$

$$P = \frac{4E^* a_{\text{Hertz}}^3}{3R}, \quad (4.2)$$

where E^* is the reduced Young's modulus, and R is the effective radius, respectively, defined by:

$$\frac{1}{E^*} = \frac{1 - \nu_1^2}{E_1} + \frac{1 - \nu_2^2}{E_2}, \quad (4.3)$$

and

$$R = \frac{R_1 R_2}{R_1 + R_2}, \quad (4.4)$$

where ν is Poisson's ratio and E is Young's modulus; the subscripts denote spheres 1 and 2.

Equation (4.2) can be rewritten into a simpler form

$$a_{\text{Hertz}}^3 = \frac{RP}{K}, \quad (4.5)$$

and $K = 4E^*/3$.

In JKR theory [109], a work of adhesion $\Delta\gamma$, which is defined as a reversible thermodynamic work per unit area that is needed to separate an interface from the

equilibrium state of two phases to a separation distance of infinity, is incorporated into the Hertz theory, yielding a new contact radius and a new approach of

$$a_{\text{JKR}} = \left(\frac{R}{K} P_1 \right)^{1/3} = \left[\frac{R}{K} \left(P + 3\Delta\gamma\pi R + \sqrt{6\Delta\gamma\pi R P + (3\Delta\gamma\pi R)^2} \right) \right]^{1/3}, \quad (4.6)$$

$$\delta_{\text{JKR}} = \frac{a_{\text{JKR}}^2}{R} - \sqrt{\frac{8\Delta\gamma\pi a_{\text{JKR}}}{3K}}. \quad (4.7)$$

The JKR analysis takes into account the adhesion force of the solids by including the surface energy. Young-Dupré [161] requires $\Delta\gamma = \gamma_1 + \gamma_2 - \gamma_{12}$, γ represents the interfacial surface energy, where the subscripts denote surface 1 and 2 (interfacial energy between solid and vapor), and the interface 12. Consequently, the apparent Hertz load P_1 is greater than the applied contact normal load P , as described by the equation (4.6).

Removal of the applied normal load (i.e., $P = 0$) reduces the contact radius to a_0 given by

$$a_0 = \left(\frac{6\pi\Delta\gamma R^2}{K} \right)^{1/3}. \quad (4.8)$$

An extensive form of equation (4.5) for JKR can be given as

$$a_{\text{JKR}}^3 - (a_0 a_{\text{JKR}})^{3/2} = \frac{PR}{K}. \quad (4.9)$$

Detailed descriptions of the DMT theory are given elsewhere [110]. Tabor [118] and Maugis [150] discussed the difference between these two limiting solutions. They proposed a transition from the DMT to JKR limit which can be governed by a dimensionless characteristic parameter, representing the ratio between the height of the neck around the contact zone and the equilibrium separation distance between the atoms at the interface. This parameter is well known as the Tabor parameter (see below).

If a liquid droplet is trapped at the contact interface (again, see Figure 4.1(b)), the adhesion force F_{adh} which is attributed to the capillary bridge is given by [162]

$$F_{\text{adh}} \cong F_{\text{cap}}(\Delta p), \quad (4.10)$$

where $F_{\text{cap}}(\Delta p)$ is the capillary force due to the Laplace pressure [88] within the meniscus given by:

$$\Delta p = \gamma_{\text{LV}} \left(\frac{1}{r_1} + \frac{1}{r_2} \right) = \frac{\gamma_{\text{LV}}}{r_m}, \quad (4.11)$$

where r_1 and r_2 are the two principal radii to describe the curvatures of the meniscus, r_m is the harmonic mean radius, and the γ_{LV} is the liquid/vapor surface tension. Note that r_m is negative due to $\Delta p < 0$.

Fogden and White [111] proposed a generalized Hertz theory which accounts for the Laplace pressure. A constant k is introduced

$$k = \frac{3\pi^{1/2} \left(-r_m - \frac{1}{2}D_0 \right)^{3/2} K}{2^{3/2} \gamma_{\text{LV}} R^{1/2}} \left(1 + \frac{D_0}{2r_m} \right)^{-1}. \quad (4.12)$$

The authors also considered the possibility that a repulsive force between the two surfaces may prevent them from coming into molecular contact, and thus D_0 is the minimum separation distance between the two surfaces and the finite contact radius a_0 generated from the interfacial adhesion can be rewritten as:

$$a_0 = \left(12\pi\gamma_{\text{LV}} \left(1 + \frac{D_0}{2r_m} \right) R^2 / K \right)^{1/3}. \quad (4.13)$$

According to their theory, a small k represents relatively large and soft spheres with vapor pressure close to the values marking the onset of capillary condensation. For such a system, a generalized Hertzian contact radius-load relationship may be expressed,

$$a^3 - (a_0 a)^{3/2} = \frac{PR}{K}. \quad (4.14)$$

Intriguingly, the mathematical similarity between equations (4.14) and (4.9) alludes to that the generalized Hertzian and JKR may possess a similar origin in their adhesion. However, the two theories present different formulations in terms of a_0 , owing to their distinctive adhesion sources.

For a system with a relatively large radius of the meniscus, i.e. $D_0 \ll -2r_m$, the solid-solid repulsive effect becomes insignificant [162] and the equation (4.13) can then be simplified as

$$a_0 = \left(\frac{12\pi\gamma_{LV}R^2}{K} \right)^{1/3}. \quad (4.15)$$

Comparing equation (4.8) with equation (4.15), the two theories may be reconciled by the following relationship between the work of adhesion and the surface tension:

$$\Delta\gamma = 2\gamma_{LV}. \quad (4.16)$$

Prior to Fogden and White derived the system constant k , Tabor [118] has introduced a similar non-dimensional parameter μ_T , which is well known as the Tabor parameter to describe the JKR-DMT transition for solid-to-solid elastic adhesion. For JKR solution, both compressive and tensile stress act in the area of contact, and no force occurs outside. On the contrary, for DMT solution, the repulsive pressure only acts in the area of contact, and adhesive force simply adds to the Hertz problem outside the contact area. Later Xu *et al.* [139] proposed a modified Tabor parameter for the contact in the presence of capillary condensation as

$$\mu_T^c = \left(\frac{2R\Delta\gamma^2}{9K^2r_m^3} \right)^{1/3}. \quad (4.17)$$

As mentioned above, for a system with relatively large radii of the meniscus, $D_0 \ll -2r_m$, then equation (4.12) reduces to another form where can be seen a strong correspondence with equation (4.17):

$$\mu_T^c = \left(\frac{\pi}{4} k^{-2}\right)^{1/3}. \quad (4.18)$$

Essentially, the Fogden and White's system constant is an alternative mathematical expression of the modified Tabor parameter for the adhesive contact in the presence of meniscus condensation. To summarize, the JKR model is valid for a relatively soft and large system roughly $\mu_T^c > 2$, which is corresponding to $k < 0.3$ (*cf.* equation (4.18)), and the DMT model is valid for a relatively small and rigid system, $\mu_T^c < 0.1$ [163].

4.3.2 Viscoelastic model

A theoretical model to describe viscoelastic adhesive contact [164] is applied to interpret the rate-dependent elastic modulus of the agarose spheres. Based on the theory, substituting the elastic modulus-approach convolution into Hertz contact theory will give a force-approach relationship in the time domain [165] as

$$P(t) = \frac{4\sqrt{R}}{3(1-\nu^2)} E(t) * [\delta(t)]^{3/2} \quad (4.19)$$

where $E(t)$ is the relaxed modulus of the spheres.

$$E(t) * [\delta(t)]^{3/2} = \int_{\xi=0^-}^t E(t-\xi) \frac{d}{d\xi} [\delta(\xi)]^{3/2} d\xi \quad (4.20)$$

Since the two spheres approached and separated at a constant speed in the experimental measurements, the approach can be expressed as:

$$\delta = Vt \quad (4.21)$$

where V denotes the constant speed.

Equation (4.19) is transformed into the Laplace domain to describe the viscoelastic responses:

$$\overline{P(s)} = \frac{4\sqrt{R}}{3(1-\nu^2)} \overline{E(s)} \cdot \overline{\delta(s)^{3/2}} \quad (4.22)$$

where $\overline{P(s)} = \int_0^\infty P(t)e^{-st} dt$, $\overline{E(s)} = \int_0^\infty E(t)e^{-st} dt$, and $\overline{\delta(s)^{3/2}} = \int_0^\infty [\delta(t)]^{3/2} e^{-st} dt$

Substitution of equation (4.21) with equation (4.22) yields:

$$\overline{P(s)} = \frac{4\sqrt{R}V^{3/2}}{3(1-\nu^2)} \overline{E(s)} \cdot \frac{\Gamma(5/2)}{s^{5/2}} \quad (4.23)$$

where Γ is a gamma function.

For modeling viscoelastic behaviors of hydrogel material, the Voigt model, which consists of a Newtonian dashpot and linear elastic spring connected in parallel (Figure 4.4) is applied. The constitutive equation to describe the stress-strain relationship of a homogenous hydrogel can be expressed as [166]

$$\sigma = E_0 \varepsilon + \mu \frac{d\varepsilon}{dt} = E(t) \varepsilon \quad (4.24)$$

where σ and ε are stress and strain, respectively, E_0 denotes elastic modulus in the steady-state (or Young's modulus), and μ is the viscosity coefficient.

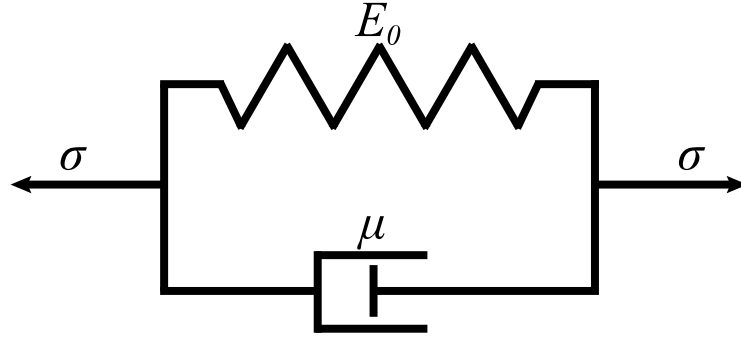


Figure 4.4 Schematic diagram of Voigt model, the system consists of a Newtonian dashpot and linear elastic spring connected in parallel undergoing the same deformation.

Equation (4.24) can be transformed into its Laplace domain as:

$$\frac{\overline{\sigma(s)}}{\overline{\varepsilon(s)}} = (E_0 + \mu s) \quad (4.25)$$

where $\overline{\sigma(s)} = \int_0^{\infty} \sigma(t)e^{-st} dt$, $\overline{\varepsilon(s)} = \int_0^{\infty} \varepsilon(t)e^{-st} dt$.

According to the correspondence principle [167], the general elastic and viscoelastic solutions can be combined into the Laplace domain to obtain an equation describing Young's modulus:

$$\overline{E_0(s)} = \frac{\overline{\sigma(s)}}{\overline{\varepsilon(s)}} = (E_0 + \mu s) \quad (4.26)$$

Substituting of equation (4.23) with equation (4.26), and inversely transforming the Laplace to the time domain, leads to

$$P(t) = \frac{4\sqrt{R}E_0V^{3/2}}{3(1-\nu^2)} \left(t^{3/2} + \frac{3}{2}\tau t^{1/2} \right) \quad (4.27)$$

where $\tau = \mu/E_0$ is defined as the relaxation time [166].

Once τ was determined by fitting the force-time $P(t)$ curve with equation (4.27), equation (4.24) can be written into the form of

$$\sigma = E_0 \varepsilon + \mu \frac{d\varepsilon}{dt} = E_0 \varepsilon + E_0 \tau \frac{d\varepsilon}{dt} \quad (4.28)$$

For simplicity, here I define an engineering strain $\bar{\varepsilon} \approx \frac{\bar{\delta}}{R}$, i.e., the ratio of a mean approach $\bar{\delta}$ to the effective radius R , and let $\varepsilon = \bar{\varepsilon}$; the equation (4.28) can be rearranged as

$$\sigma = E_0 \bar{\varepsilon} + E_0 \tau \frac{d(\frac{\bar{\delta}}{R})}{dt} = E_0 \bar{\varepsilon} \left(1 + \tau \frac{V}{R \bar{\varepsilon}}\right) \quad (4.29)$$

Substituting equation (4.24) into equation (4.29), the $E(t)$ can be expressed as

$$E(t) = E_0 + E_0 \frac{\tau V}{R \bar{\varepsilon}} = E_0 \left(1 + \frac{\tau V}{R \bar{\varepsilon}}\right) \quad (4.30)$$

Therefore, the equation (4.30) provides a relationship between Young's modulus and the separation speed V .

4.4 Results and discussion

Figure 4.5 compares experimental measurements with the predictions of the JKR theory and shows consistency in the force-approach $P(\delta)$ curve for a constant unloading speed of 20 $\mu\text{m/s}$. Using least-squares fitting the measured $P(\delta)$ curve with equation (4.6) and equation (4.7), the work of adhesion and the reduced Young's modulus of the spheres are determined to be $\Delta\gamma = (146 \pm 4)$ mN/m and $E^* = (53 \pm 2)$ kPa, respectively. The Young's modulus is then calculated as $E = (79 \pm 3)$ kPa if Poisson's ratio ν of the hydrogel spheres is assumed to be 0.5 (*cf.* equation (4.3)). A comparable value of Young's modulus $E = (72 \pm 3)$ kPa was measured from the spherical indentation test for the disk-shaped agarose sample by simply fitting with the loading force-indentation depth $F(h)$ curve with Hertz theoretical prediction, i.e.

$F = \frac{4}{3}E^*R^{1/2}h^{3/2}$ (again, see Figure 4.3(b)). There was a liquid collar around the contact area, which manifest as a “negative” force in the force-indentation depth curve. However, liquid bridge force has no significant influence on the determination of the Young’s modulus of the hydrogel, because the mechanical force dominant region (0.2-0.4 mN) of force-indentation depth curve was used in the analysis. Hyper-elastic behaviors often exhibit in soft matters such as hydrogel materials under large deformation. However, both the experimental curves of the pull-off $P(\delta)$ and indentation testing $F(h)$ do not manifest such non-linear behaviors because they were measured under small deformations (engineering strains <1.5%).

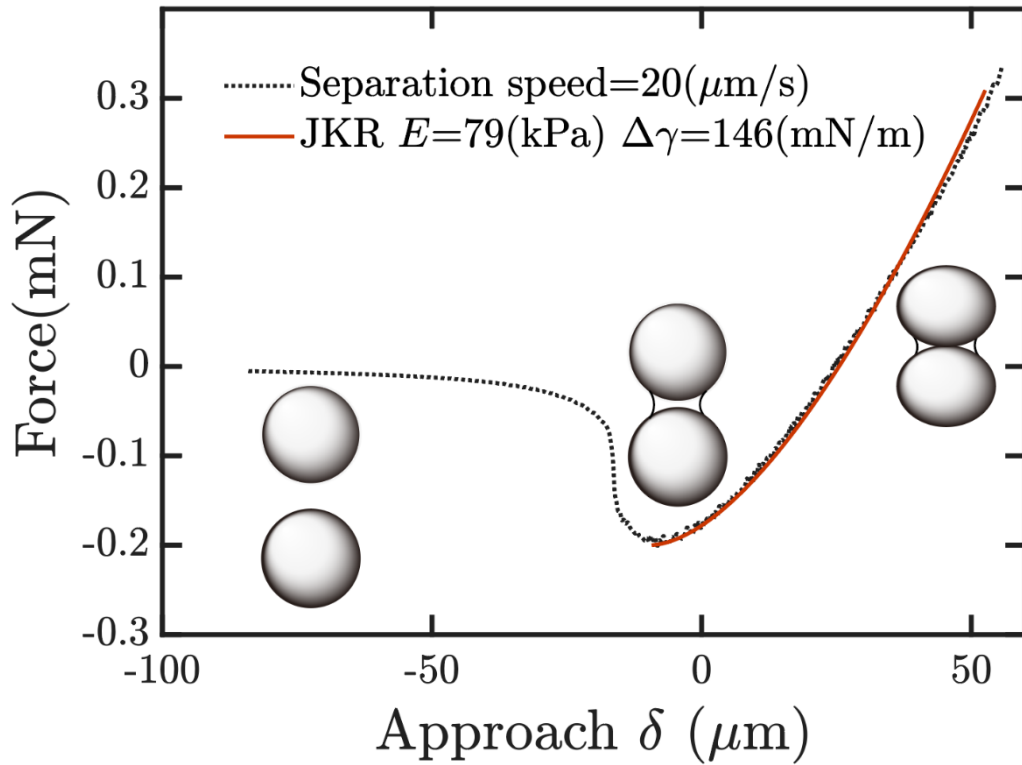


Figure 4.5 Comparison of experimental force-approach $P(\delta)$ curve (measured at a constant separation speed $20 \mu\text{m/s}$) and the JKR theoretical prediction with least-square fitting.

It is worth to note that the water surface tension γ_{LV} is ca. 72 mN/m at room temperature [88], which is consistent with the theoretical prediction of $\Delta\gamma = 2\gamma_{LV}$ (cf. equation (4.16)). For the current case ($R \approx 250 \mu\text{m}$, $r_m \approx -1$ to $-7 \mu\text{m}$), μ_T^c was found to be in the range of 0.9 to 6.2. Since the values of μ_T^c are larger than 0.1, the DMT approximation is not applicable. Due to the lack of explicit solutions for the DMT-JKR transition, and only empirical equations being available [168], the JKR theory is the most suitable for fitting with the $P(\delta)$ curves.

Figure 4.6(a) shows the experimentally measured $P(\delta)$ curves for various separation speeds. The $P(\delta)$ curves for the higher speeds clearly show the increase in their slopes due to viscoelastic deformation. Fracture mechanics [169,170] shows that the contact line between two deformable solids can be considered as the crack tip of a crack path along the interface, and the work of adhesion $\Delta\gamma$ is equal to the critical elastic energy release rate G , for crack initiation or propagation. Previous experiments for viscoelastic solids show the relationship $G(v, t) = G_0[1 + f(v, T)]$ between G , crack tip velocity v and temperature T [171–173]. G_0 is the threshold value when an arrested crack is about to grow. The factor $f(v, T)$ depends on the viscoelastic dissipation of the elastomers close to the cracktip, which increases with the increment of v . Thus, the work of adhesion between viscoelastic spheres in a dry contact is expected to increase with the separation speed. Figure 4.6(b) shows the JKR-fitted $\Delta\gamma$ values for the current capillary force to be independent of the separation speed in contrast to the dry-contact, while E exhibits a linear increase manifesting typical viscoelastic behavior of hydrogel materials. To examine the viscoelasticity of the spheres, Figure 4.8(a) shows least-squares fitting experimental force-time $P(t)$ curve at a speed $20 \mu\text{m/s}$ with the equation (4.27) of the viscoelastic model to determine the relaxation time $\tau = 0.17 \text{ s}$, which demonstrates a considerable liquid-like behavior

apart from their elastic deformation behavior [174]. Moreover, Figure 4.8(b) shows the comparison of the measured Young's modulus E at various separation speeds (also see Figure 4.6(b)) and the prediction of the viscoelastic model using the equation (4.30) for various separation speeds $V=10 - 30 \mu\text{m/s}$. Hence the viscoelastic model of section 3.2 provides a quantitative interpretation for the increase of the Young's modulus as separation speed increases.

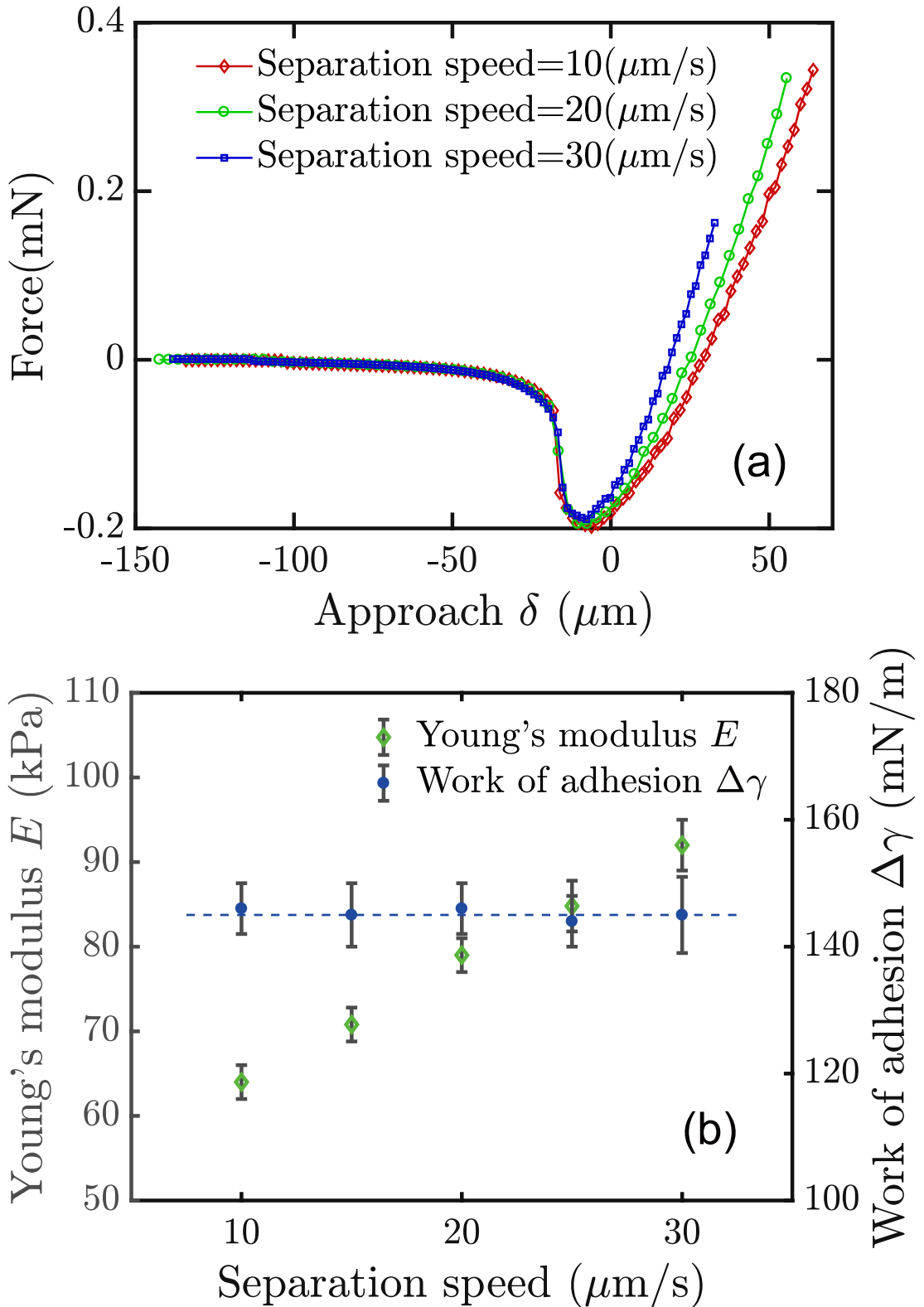


Figure 4.6 (a) The unloading force-approach $P(\delta)$ curves measured at different separation speeds. (b) The JKR-fitted values of Young's modulus E and work of adhesion $\Delta\gamma$.

We also examined the roughness of the particle surfaces using an optical 3D microscope (Bruker, ContourGT-K). The root mean square (RMS) roughness of the surface was measured around 4.2 μm . Several studies [175,176] have shown rubber-like materials with similar magnitudes of surface roughness under dry contact have noticeably lower adhesion values even at a much higher separation speed. Therefore, the results imply that the adhesion of the agarose particles is mainly originated from the water-vapor interfacial surface tension, which is less susceptible to the surface roughness and the separation speed. It is worth pointing out that the liquid bridge can be formed spontaneously between the particles subject to a compressive force, irrespective of their surface roughness and the ambient humidity. Although the two hydrogel spheres are viscoelastic, the structure of their contact region is regulated by the same physics that establishes the shapes of liquid droplets. A similar phenomenon in the adhesion occurred in the case of a rigid particle in contact with a soft gel substrate has been described by Jensen *et al.*[177]. For solids, the difference between surface free energy γ and surface tension σ is well distinguished. The surface free energy is defined as the work required to create a new unit of area reversibly and isothermally, while the surface tension is the amount of the reversible work per unit area needed to stretch a pre-existing surface elastically. For liquids, the surface free energy and the surface tension are identical, while for solid materials, γ does not necessarily equal to σ [178–180]. Maugis suggested that for an ideal case of solids 1 and 2 forming a single crystal, the interfacial energy γ_{12} should be zero in the aforementioned Young-Dupré equation ($\Delta\gamma = \gamma_1 + \gamma_2 - \gamma_{12}$), and the energy $\Delta\gamma$ should equal 2γ , which is the cohesive energy [181]; referring to the capillary bridge between the two hydrogel particles in the current case. A corresponding physical mechanism exists in the solid-liquid interphase of the two hydrogel particles, in which

liquid capillary bridges their contact. Because the liquid phase dominates the surface tension, the surface energy between the two agarose hydrogel particles should be identical to the surface tension of the solvent. This can be confirmed by the current experiment as $\Delta\gamma$ is equal to twice the surface tension of water γ_{LV} , which alludes to the physical interaction of two spherical liquid droplets. This interesting behavior may be attributed to the porous microstructure of agarose gel which retains typically water content more than 90% W/W.

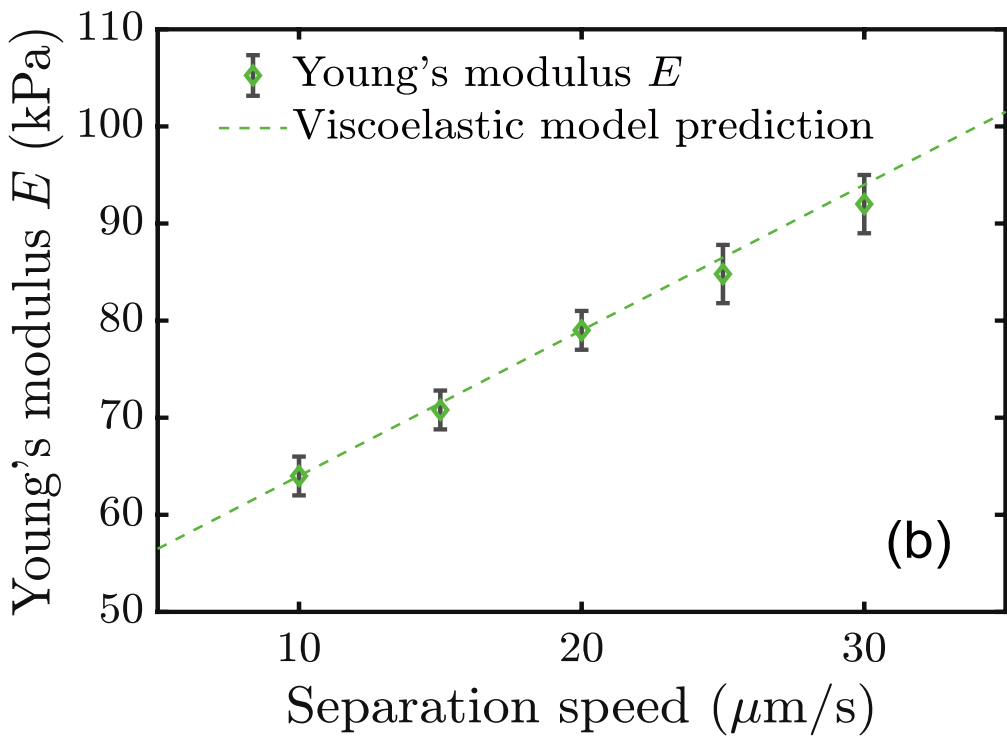
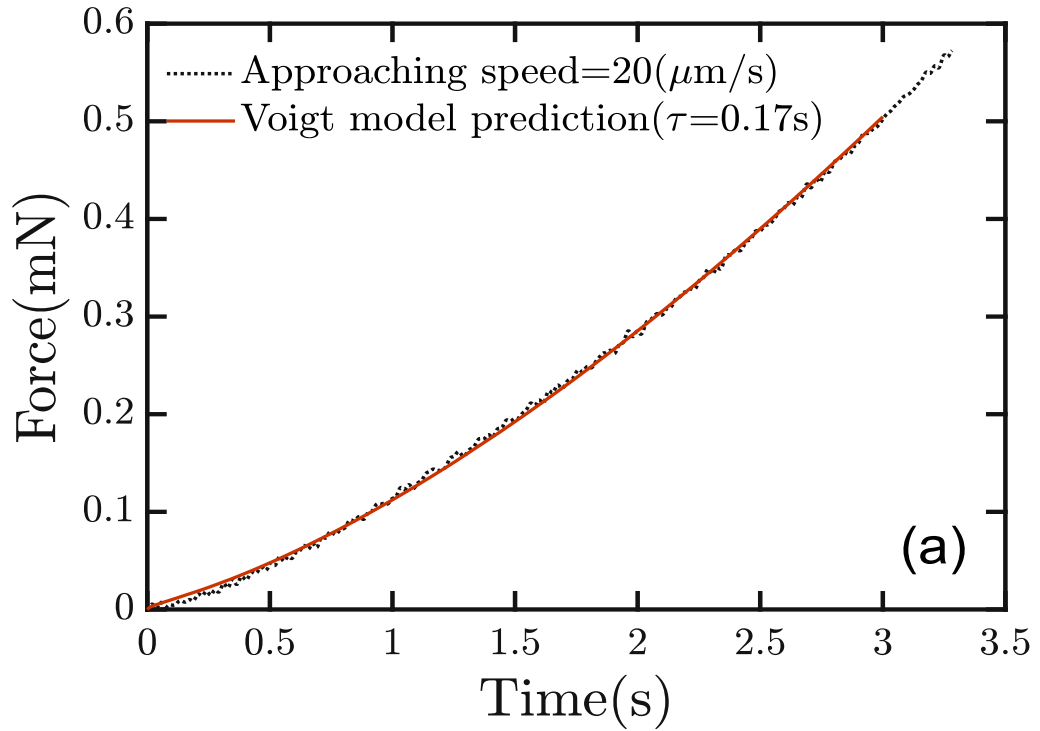


Figure 4.7 (a) Using least-squares fitting experimental force-time $P(t)$ curve (measured at a constant speed $20 \mu\text{m/s}$) with the Eq. (4.27). (b) Comparison of the measured Young's modulus E at various separation speeds and the prediction of the viscoelastic model using the Eq. (4.30).

4.5 Summary

We have directly measured the unloading $P(\delta)$ curves and the side-view profiles between two liquid-bridged agarose microspheres at various separation speeds. The JKR theory has been successfully applied to interpret the measured $P(\delta)$ curves of the microparticles for the quantitative estimation of their mechanical and interfacial properties. My finding demonstrates that the hydrogel particles exhibit viscoelastic deformation under mechanical forces, while their interparticle adhesion is governed by the surface tension. Moreover, the work of adhesion shows to be independent of the separation speed and, by contrast, Young's modulus exhibits a linear increase that can be interpreted by the viscoelastic model proposed in section 3.2. Therefore mechanical characterization of capillary force will be essential for the soft particulate materials to improve material properties in their applications such as food processing and drug delivery.

5 Investigations of humidity influencing interparticle capillary force

5.1 Introduction:

When two lyophilic surfaces are brought to proximity in the presence of vapor as an intervening medium, the condensation of vapor will form a liquid meniscus in between at the tight gap. Such a phenomenon ubiquitously exists in many materials, such as granular materials [182], colloid particles [183] and sandy soils [184]. One of the distinct examples in these materials is that moisture may increase adhesion forces between particles which results in agglomeration of powders. Hence, studying the humidity dependence of interparticle capillary force is of paramount importance in many engineering applications such as food processing [4], pharmaceutical mixtures [3], powder handling [185], aerosol suspension [186] and biomaterial dehydration [187]. Fundamentally, such studies are also essential to better understand the underlining humidity influence on nanoscale systems. For example, when a liquid meniscus is formed on solid surfaces, the capillary forces may impact the indentation measurement of the materials using AFM [188].

Several advanced instruments have been applied to measure the humidity-dependent adhesion; namely, SFA [48], force feedback microscope [189], force traction device [190] and AFM [29,146]. Among these techniques, AFM (details see section 2.2.1) is the most prevailing technique to study the capillary force owing to its superiority in force measurement; typical force resolutions range from a few piconewtons to nanonewtons. Hence it can be used to measure the adhesion force between two

surfaces accurately; for example, a particle removed from a substrate. AFM has been widely employed to investigate the humidity influence on the capillary forces in various applications, including oxide microparticle adhered on oxide surface [191], AFM tip/probe interaction with a smooth [192] or patterned surface [193] and pollen adhesion on hydrophilic surfaces [194]. Moreover, it has been reported that AFM was applied to investigate the dependence between adhesion force and RH [25,26]. Alternatively, SFA (details see section 2.2.2) has been widely used to measure capillary forces based on a similar working principle as AFM, i.e. measuring the adhesion force between two liquid-bridged surfaces separating. For example, SFA has been applied to measure the impact of humidity on adhesion between rough surfaces [195], evaporation and condensation of the meniscus in a slit-like pore [55], and adhesion mechanisms for gecko-inspired microfibrillar surfaces [196]. However, up to now, there is no report that these techniques have been applied to directly measure the humidity dependence of capillary forces between two spherical particles on a micrometer level.

On the theoretical front, analytical and numerical models play a pivotal role to understand how humidity influences the pull-off force compliance. In principle, these models use the Kelvin equation to describe the mean curvature of the meniscus, while apply the Young-Laplace equation to calculate the pressure difference between the meniscus and the surrounding air. Several analytical models, i.e., first-order approximations which describe the interrelationship between the meniscus profile and the separation distances of two spherical surfaces have given reasonable explanations for the experimental results of adhesion force force-displacement curve (compliance) [197]. Recent developments of numerical models and simulations have offered more detailed considerations in the exact shape of the liquid bridge [198] or Van der Waals

force influence [199] on the condensation in the humid air. Furthermore, several models [145,200] considering the impact of surface roughness have been developed over the years. Recently investigations have been carried out for the effects of surface roughness on liquid bridge capillarity between two parallel planes [201] and particle-wall impaction under different humidity conditions [202]. However, so far, the investigation on surface roughness influencing the humidity-dependent capillary force between two spherical microparticles has not yet been reported.

In this study, the novel technique for force-displacement sensing is used to directly measure the pull-off compliance of two polymer microparticles during separation in a controllable humid environment (details see 2.3.1 and Figure 5.1). Both an analytical model and a numerical model have been applied to interpret the experimental results of the interparticle capillary force measured under high RH. Moreover, the adhesion forces against a range of RH have been investigated using a model which takes into account the effects of surface roughness. Humidity influence on the capillary force of the microparticles has therefore been characterized quantitatively.

5.2 Experimental section

5.2.1 Experimental procedure

The force-displacement measurement unit was placed and sealed in a transparent chamber which regulated the RH accurately by using a humidity controller (ibidi GmbH, Gas Mixer M-323) (again, see Figure 5.1).

Spherical PMMA particles (Figure 5.2) were supplied by a commercial manufacturer (EPRUI Biotech Co. Ltd, PRC). The particle sizes range from 700 to 900 μm in diameter. Two PMMA microspheres of a similar size (ca. 800 μm in diameter) were selected to form a vertical alignment. The top sphere was attached to the force transducer probe, while the bottom sphere was glued firmly on a flat glass substrate to avoid unwanted sliding during the contact process. The *X-Y* stage adjusted the position of the bottom sphere to align with the top sphere axially. The long-focal CCD microscope was used to monitor the movement from the side-view in two orthogonal directions to ensure a pole-to-pole alignment. The top sphere was then lowered by the *Z*-stage and brought to form contact at the poles. The humidity controller then regulated the RH in the chamber to reach a target RH value, ranging from 60 to 95%. For measuring the pull-off force-displacement curves, the top sphere was then retracted by the *Z*-stage moving upward until the two spheres are fully separated.

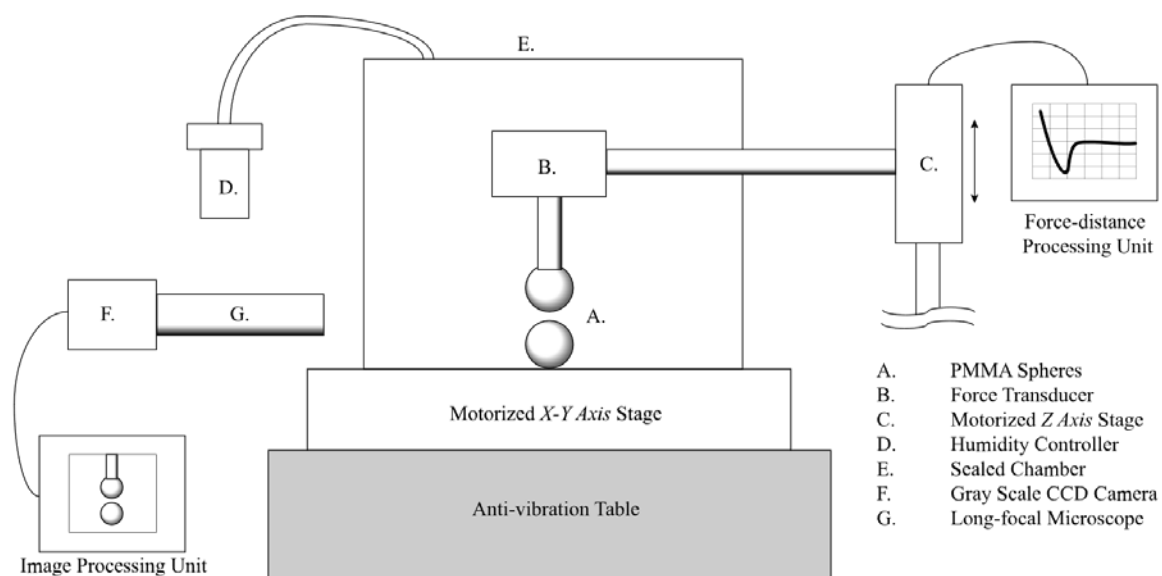


Figure 5.1 The schematic of the experimental setup (not to scale).

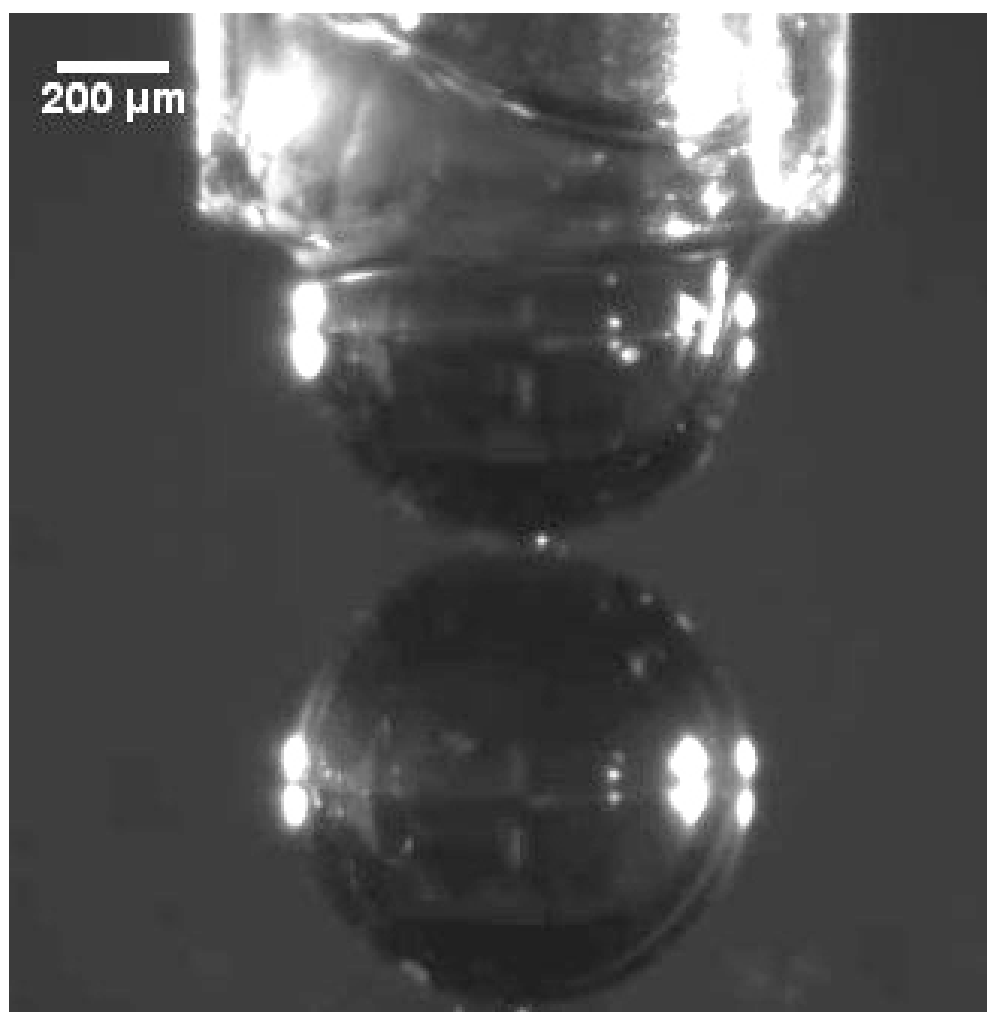


Figure 5.2 Micrographs of the PMMA spheres in contact.

5.2.2 Surface roughness measuring

The surface topographies of PMMA spheres were characterized by AFM scanning to measure their surface roughness. A tapping mode AFM (Bruker, Innova), which consisted of a silicon probe and a spring with a stiffness constant of 3 N/m (Bruker, RFESP), was applied to perform a line-by-line scanning (256 sampling points per line) over a $5 \times 5 \mu\text{m}^2$ at a rate of 0.25 Hz. AFM image processing and local root mean square (RMS) roughness calculations were carried out by Gwyddion (Gwyddion, v2.56) and MATLAB (MathWorks, 2017a).

5.3 Analytical and numerical analyses

5.3.1 First-order approximation

Based on a similar approach of the analytical models [24,203–205], the liquid surface of the meniscus in the direction parallel to the axis of symmetry is described as a circle of radius r between two identical spheres of radius R_s . The geometric shape of the capillary is defined by two principal radii l and r (see Figure 5.3). The size of the liquid meniscus is assumed to be very small, so the surface force denotes the majority of the interaction, and the gravity is negligible.

The total capillary force F consists of two components:

$$F = 2\pi\gamma l - \pi l^2 \Delta P \quad (5.1)$$

The first term on the right-hand side indicates the liquid surface tension γ acting around the neck of the meniscus, which creates a pulling surface tension force between the two spheres. The second term on the right-hand side is the so-called capillary pressure force, which is expressed by the cross-section area of the neck of the capillary bridge πl^2 and the pressure difference ΔP between the inside and outside of the meniscus.

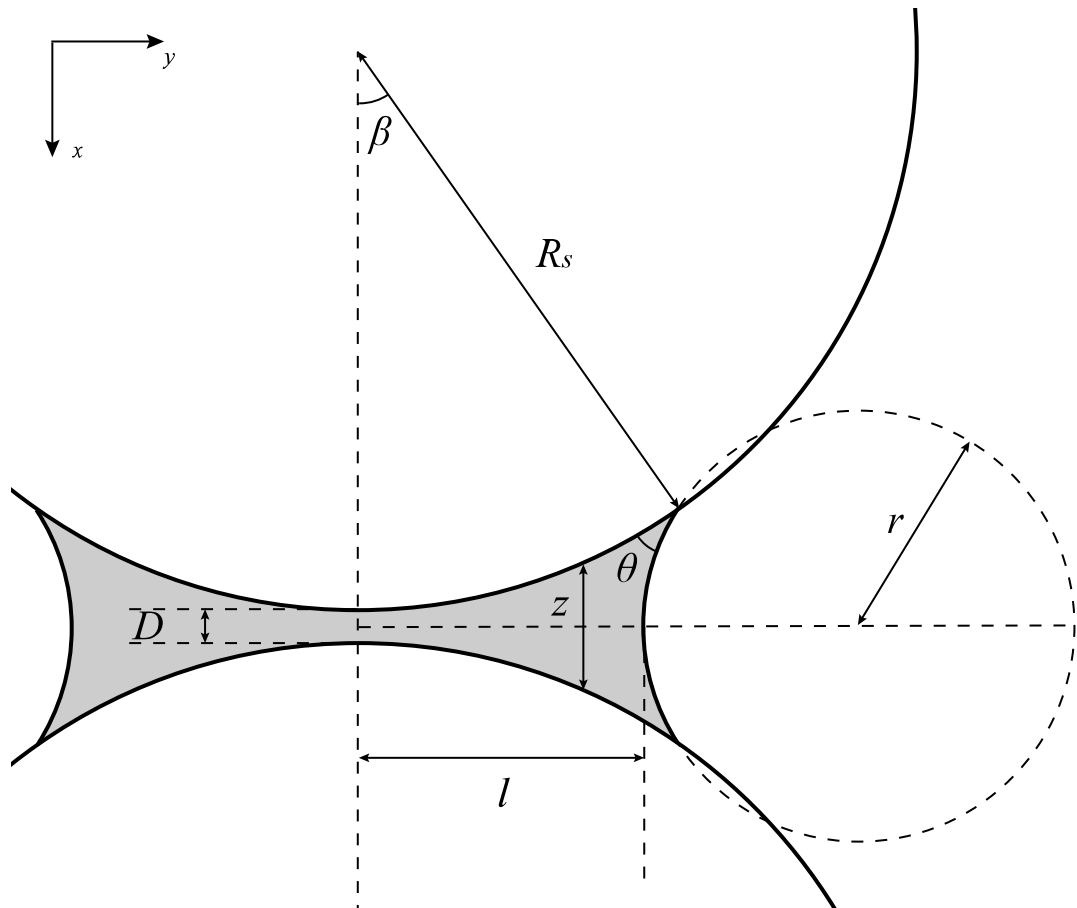


Figure 5.3 Schematic of the liquid bridge formed between two PMMA spheres of the same radius.

The Young-Laplace equation relates the curvature of the meniscus interface to the pressure difference ΔP of the liquid and vapor. In the absence of gravitation, the Young-Laplace equation can be expressed as:

$$\Delta P = \gamma \left(\frac{1}{l} - \frac{1}{r} \right) \quad (5.2)$$

Furthermore, under the assumption that the liquid phase is in the thermodynamic equilibrium with the surrounding air, the Kelvin equation describes capillary condensation, which relates the actual vapor pressure P to the curvature of the surface of the condensed liquid. It can be expressed as:

$$\bar{R}T \ln \frac{P}{P_0} = V_m \Delta P \quad (5.3)$$

where \bar{R} is the molar gas constant, which is 8.314 J/(mol K). T stands for the temperature. P_0 is the saturation vapor pressure over a planar liquid surface. V_m stands for the molar volume of the liquid and $\frac{P}{P_0}$ is the RH.

Combine equation (5.2) and equation (5.3), Kelvin length λ_K , a parameter which characterizes the range of the capillary forces, can be defined as:

$$\lambda_K = \frac{\gamma V_m}{\bar{R}T} = \ln \frac{P}{P_0} \left(\frac{1}{l} - \frac{1}{r} \right)^{-1} \quad (5.4)$$

At 25 °C, the saturation vapor pressure P_0 and surface tension γ of water are 3.17 kPa and 71.99 mN/m respectively; λ_K can be calculated as 0.52 nm.

If I assume $R_s \gg l \gg r$, the saturation equilibrium condition is met when

$$\lambda_K = - \left(\ln \frac{P}{P_0} \right) r^{-1} \quad (5.5)$$

For modeling the three-phase contact line, the filling angle β and the liquid contact angle θ are introduced. To simplify further calculations, I define

$$c = \cos(\theta + \beta) \quad (5.6)$$

An approximate expression of the capillary force F under the assumption of constant capillary volume V is given by:

$$F = 2\pi\gamma cR_s \left(1 - \frac{D}{\sqrt{\frac{V}{\pi R_s} + D^2}} \right) \quad (5.7)$$

D is the axial pole-to-pole distance between two spheres (see Figure 5.3). Kohonen *et al.* [53] derived an approximation of the growing speed of the meniscus radius r when the condensation equilibrium condition is not yet to be met:

$$\frac{dr}{dt} = \frac{2D_d M_W P_0}{\rho \bar{R} T R_s} \left(\frac{P}{P_0} - e^{-\frac{\lambda_K}{r}} \right) \quad (5.8)$$

where $D_d = 2.5 \times 10^{-5} \text{ m}^2/\text{s}$ is the diffusion coefficient of the surrounding vapor molecules at 25 °C. M_W is the molar mass of the liquid molecules, and ρ is the liquid density. The radius r stops to grow when the equilibrium condition is met (see equation (5.5)). When the distance D between the two spheres continues to increase during separation, the radius of meniscus r will correspondingly increase due to the stretching capillary. According to equation (5.8), $r > \lambda_K$, $\frac{dr}{dt} < 0$ indicates that r tends to shrink. The maximum shrinking speed $-\frac{dr}{dt}$ will reach when $r \gg \lambda_K$. For the current study, the separation speed is 1 $\mu\text{m}/\text{s}$, which is considerably faster than the maximum shrinking speed of 0.14 $\mu\text{m}/\text{s}$ at RH 95% calculated based on equation (5.8). Hence, the liquid bridge can be reasonably assumed as a constant volume in the current analysis.

The adhesion force F_{adh} is defined as the force required to separate the two contacting spheres, which can be expressed by simplifying equation (5.7) with $D = 0$:

$$F_{\text{adh}} = 2\pi\gamma cR_s \quad (5.9)$$

Equation (5.9) is derived based on the assumption of two smooth contacting spheres, which shows that the adhesion force is affected by the spheres radii and the liquid surface tension.

5.3.2 Numerical model

Dörmann and Schmid (DS) [198,206] developed a numerical model that calculates the profile of the humidity-dependent capillary bridge. Similar to the first-order approximation, the DS model also employs both the Kelvin equation and the Young-Laplace equation to calculate the Kelvin length and the pressure difference between the meniscus and surrounding air. However, instead of assuming a circular profile for the meniscus, the DS model simulates the exact shape of the bridge profile by numerically integrating the gradients of many distinct vertices consecutively. The gradients are interpolated linearly between every two neighboring vertices.

In the present model, an exact shape can be calculated based on the capillary volume V . The center of Sphere 1 is taken as the frame of reference, and the line connecting the two sphere centers serves as the x-axis (see Figure 5.4). The meniscus can then be modeled as many distinct vertices, and in between two neighboring vertices linked by a piecewise straight line. The first vertex on the sphere is determined by an estimated filling angle β . For the first point, the coordinates are $(R_s \cos \beta, R_s \sin \beta)$. The gradient of the piecewise straight line on this vertex which describes the profile of the meniscus is $\nabla_1 = -\cot(\theta + \beta)$. With a given increment dx on the X-axis, the coordinates of second vertex can be calculated using those of the first vertex and the given gradient. The coordinates of the second vertex are $(R_s \cos(\beta + ds), R_s \sin(\beta + \nabla_1 \times ds))$.

The two principal radii of r_1 and r_2 of the meniscus is governed by the classical Young-Laplace equation (see equation (5.2))

$$\Delta P = \gamma \left(\frac{1}{r_2} - \frac{1}{r_1} \right) = -\frac{\gamma}{\lambda_K} \quad (5.10)$$

Axisymmetry of the capillary bridge requires r_2 to be measured from the x-axis, which is the distance between the center of the circle and the second vertex. With the known value of Kelvin length as 0.52 nm, the r_1 can be then deduced. Profile of the meniscus $y(x)$ is linked to the curvature radius r_1 by

$$r_1 = \frac{\left[1 + \left(\frac{dy}{dx} \right)^2 \right]^{\frac{3}{2}}}{\frac{d^2y}{dx^2}} \quad (5.11)$$

Solving the differential equation (5.11), the gradient of the piecewise straight line connecting the second and the third vertices $\nabla_2 = \frac{dy}{dx}$, can be calculated. The procedure continues until the meniscus reaches the second sphere. The coordinates on the second sphere are then checked with the coordinates on the first sphere to see if they are symmetrical to the central axis between the two spheres. If the first vertex is at (x_1, y_1) , the last vertex, located on Sphere 2, which can be obtained after a total number $n - 1$ of integration of the line gradient, has coordinates (x_n, y_n) . The convergence check condition can be given as

$$|y_1 - y_n| < 10^{-11} \text{ m} \quad (5.12)$$

Once $y(x)$ is found, the capillary volume V_{DS} is determined by summing up the volumes of conical frustums between every adjacent vertex. In the case of two adjacent vertices (x_i, y_i) and (x_{i+1}, y_{i+1}) , the volume of the frustum is given by

$$V_i = \frac{\pi}{3} (y_i^2 + y_{i+1}^2 + y_i y_{i+1}) (x_{i+1} - x_i) \quad (5.13)$$

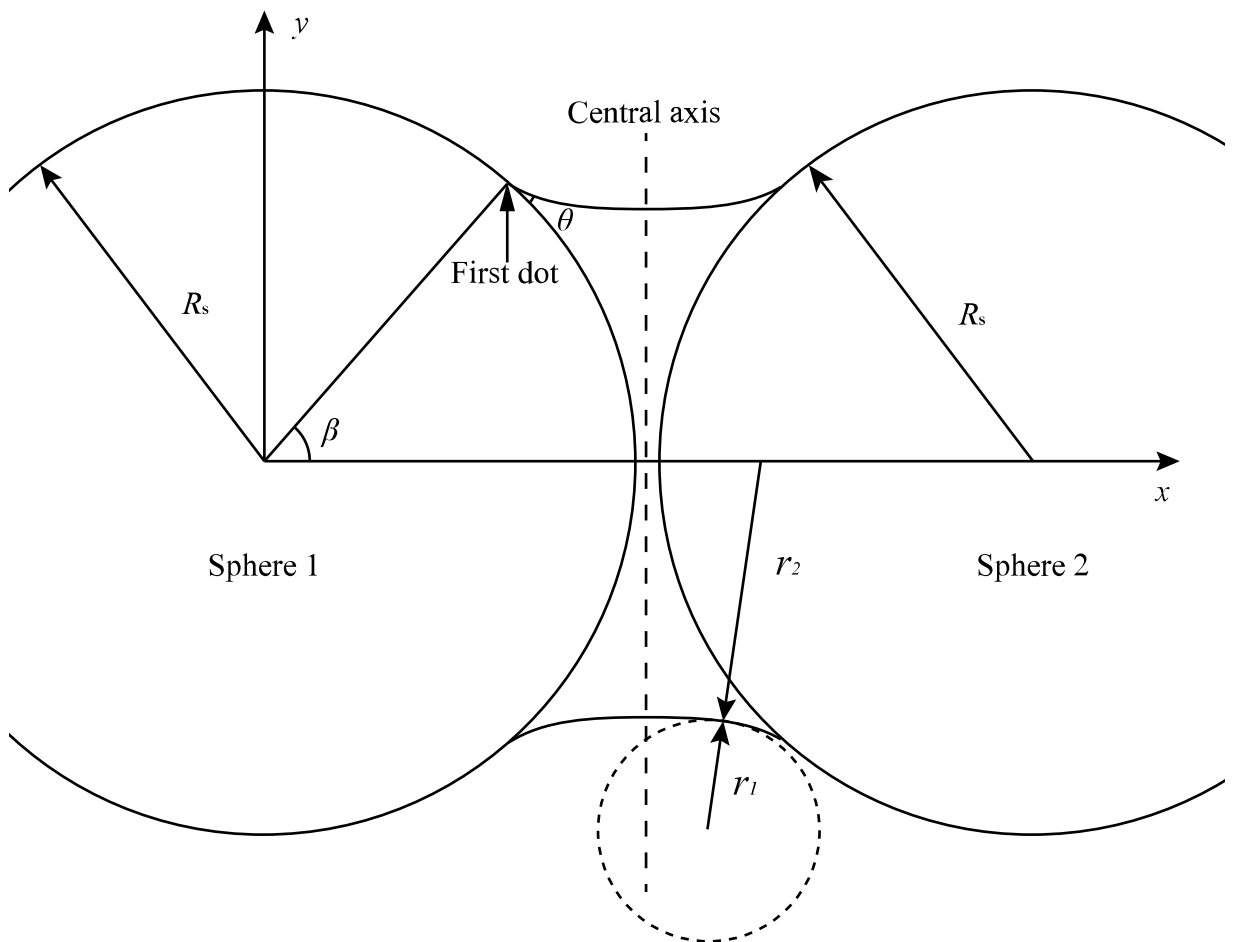


Figure 5.4 Schematic of the coordinate system for the numerical solution based on the DS model. Capillary forms between two spheres of the identical radius R_s , with the filling angle β and contact angle θ . The first calculation vertex is located on Sphere 1.

Then the volumes of the two spherical caps V_{sc} which reaches into the capillary are subtracted.

$$V_{sc} = 2 \times \frac{\pi}{3} R_s^3 (2 + \cos \beta)(1 - \cos \beta)^2 \quad (5.14)$$

Thus, the total volume of the capillary calculated based on the DS model can be determined as

$$V_{DS} = \sum_{k=1}^{n-1} V_k - V_{sc} \quad (5.15)$$

The total volume V_{DS} is checked with the volume V obtained from the first-order approximation. If the calculated volume V_{DS} is larger than the volume V , a smaller filling angle β will be used to recalculate capillary profile and volume through the algorithm, and vice versa. A MATLAB (MathWorks, 2017a) program is developed to perform the numerical iteration (see Figure 5.5 for the flowchart of the program).

After the final meniscus profile is obtained, the capillary force is calculated at the neck of the meniscus, which can be linked by the radius of the neck of the meniscus r_{neck}

$$F = -\Delta P \pi r_{neck}^2 + 2\gamma \pi r_{neck} \quad (5.16)$$

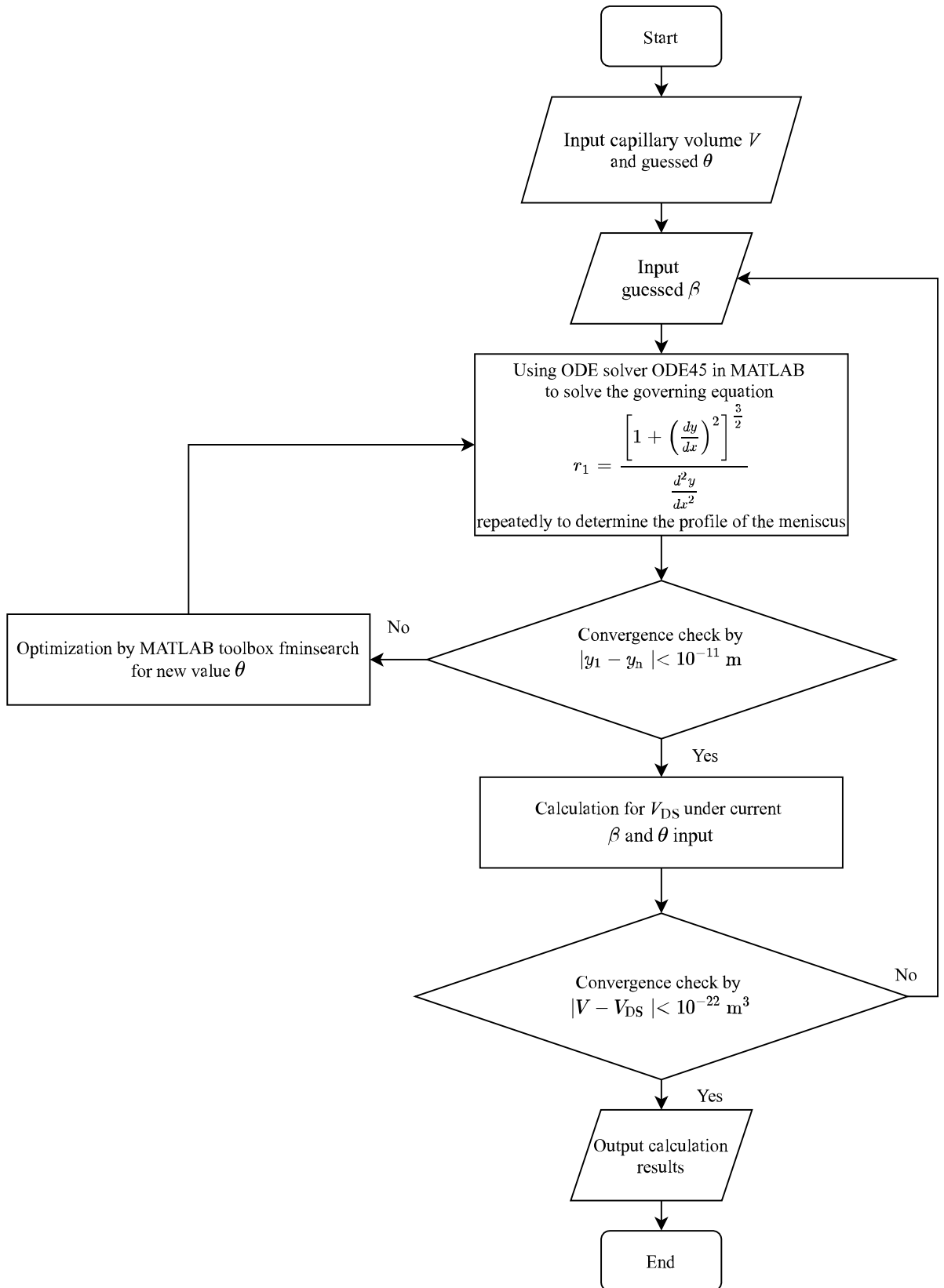


Figure 5.5 Flowchart of numerical calculation for the geometric shape of the meniscus.

5.3.3 Influence of the surface roughness

As previously mentioned, equation (5.9) is only valid for two perfectly smooth spheres in contact, which results in that the adhesion force is independent of the surrounding vapor pressure. However, several previous experimental studies showed the dependence between adhesion forces and RH [33,207], which might be attributed to the surface roughness of the contacting surfaces. For the current case, the Kelvin length $\lambda_K \approx 0.52$ nm denotes the length scale of the surface structures which have the same scale as the roughness of a relatively smooth surface; Surface roughness can not be ignored in computing adhesion force. The surface roughness will normally reduce the capillary force, because of the low vapor pressure of the capillary bridge only formed on individual asperities. The geometric size of the single asperity will dominate the adhesion force, which is considerably smaller than the radii of the spheres. For high vapor pressure, the geometric size of the meniscus grows immensely comparing to the surface roughness, thus the smaller capillary bridges will merge into one. The adhesion force will be dominated by the overall radii R_S of the spheres (see Figure 5.6). Several investigators took into account of surface roughness and assumed that the capillary only formed between asperities [191,208]. Butt[145] recently introduced a model to quantify the surface roughness impact on the adhesion force between particles. Similar to the aforementioned first-order approximation, Butt's model assumes the capillary profile as a circular shape and that liquid can only condense into a gap when the gap width between two contacting spheres is smaller than $2cr$.

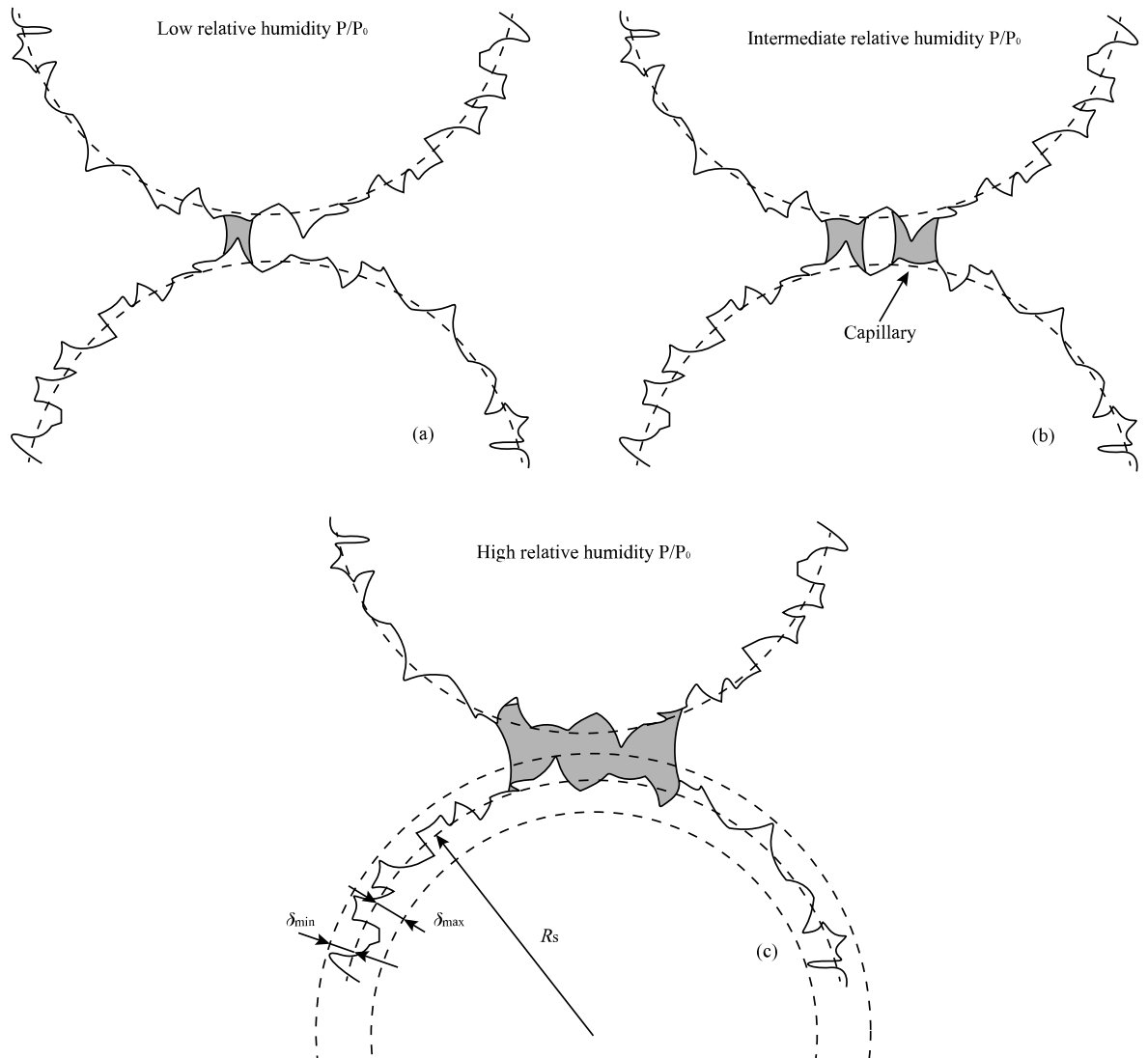


Figure 5.6 Schematic of capillary bridges forming between asperities of two spheres under different RH (not to scale): (a) only one capillary bridge forms between asperities under low RH; (b) number of capillary bridges increases with RH; (c) various smaller capillary bridges merge into one.

Surface roughness functions φ_1 and φ_2 are assigned to the two surfaces. The function φ_i is in the dimension of m^{-1} indicates the probability of an asperity with height δ and is therefore restrained by $\int_{-\infty}^{\infty} \varphi_1(\delta) d\delta = 1$. A joint surface roughness function φ is defined as the convolution of φ_1 and φ_2 .

A shape function $g'(z)$ is also introduced to describe the general shape of the two contacting surfaces, where z is the intersurface gap and is measured parallel to x -axis (see Figure 5.3). A height distribution $g(z)$ is defined as the convolution of the joint surface roughness function φ and the general surface shape function $g'(z)$.

$$g(z) = \int g'(\zeta) \varphi(\zeta - z) d\zeta \quad (5.17)$$

Finally, an integrated height distribution $G(z)$ is given, it relates to the height distribution $g(z)$ as

$$G(z) = \int_{-\delta_{min}}^{z-\delta_{min}} g(\zeta) d\zeta \quad (5.18)$$

δ_{min} is the maximal asperity heights (see Figure 5.6(c)). Then, the adhesion force is giving by

$$F_{adh} = A_0 G(z) \frac{\gamma}{r} \quad (5.19)$$

where $A_0 = \pi R_s^2$ is a reference area.

Without loss of generality, the two spheres are taken to be identical such that

$$g'(z) = \frac{1}{R_s^2} \left(R_s - \frac{z}{2} \right) \quad (5.20)$$

It is further assumed that $\varphi_1 = \varphi_2$ and the asperities are uniformly distributed and are characterized by height ranging from $-\delta_0/2$ and $\delta_0/2$ (see Figure 5.7(a)). The joint surface roughness function φ thus becomes:

$$\varphi(\delta) = \int_{-\delta_0/2}^{\delta_0/2} \varphi_1(\zeta)\varphi_2(\delta - \zeta)d\zeta \quad (5.21a)$$

$$\varphi(\delta) = \frac{\delta_0 + \delta}{\delta_0^2} \text{ for } -\delta_0 \leq \delta \leq 0 \quad (5.21b)$$

$$\varphi(\delta) = \frac{\delta_0 - \delta}{\delta_0^2} \text{ for } 0 < \delta \leq \delta_0 \quad (5.21c)$$

Combine equations (5.17) (5.18) (5.20) and (5.21), the integrated height distribution $G(z)$ is found to be[145]:

For $0 \leq z < \delta_0$,

$$G(z) = \frac{z^3}{6\delta_0^2 R_s} \quad (5.22a)$$

For $\delta_0 < z \leq 2\delta_0$,

$$G(z) = \frac{1}{6\delta_0^2 R_s} [z^3 - 2(z - \delta_0)^3] \quad (5.22b)$$

For $z \geq 2\delta_0$,

$$G(z) = \frac{1}{R_s^2} [(R_s - z)(z - \delta_0) + 2\delta_0] \approx \frac{z - \delta_0}{R_s} \quad (5.22c)$$

Substituting equation (5.5) and (5.22) into equation (5.19), F_{adh} can be found as a function of RH, should the surface roughness is known.

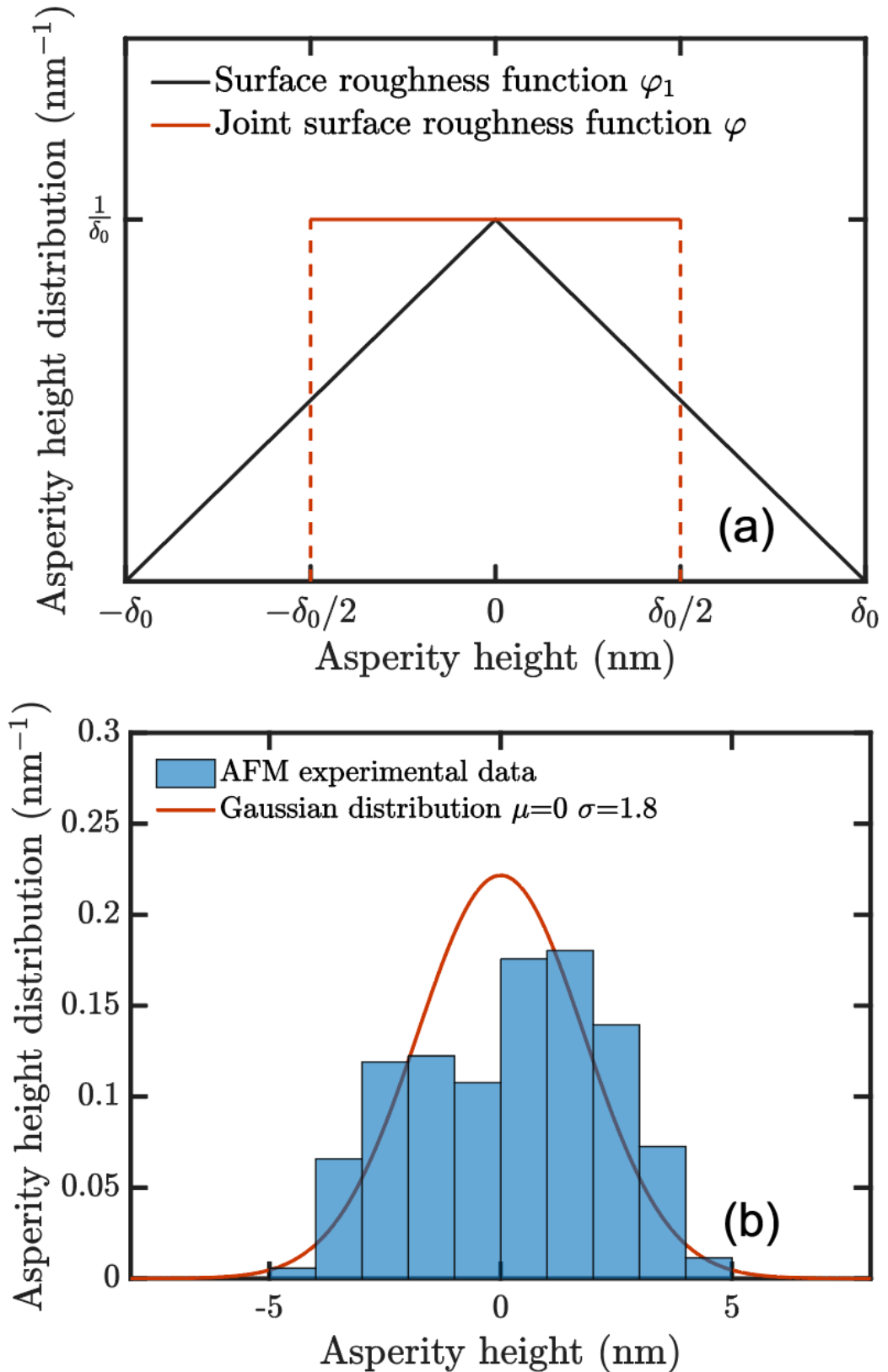


Figure 5.7 (a) the uniform surface roughness function φ_1 and the joint surface roughness function φ are assumed in Butt's model; (b) the experimental surface roughness function measured by AFM, fitted with Gaussian distribution with $\mu = 0$ and $\sigma = 1.8$.

5.4 Results and discussion

Figure 5.8 shows the experimental force versus distance ($F-D$) curve under a RH of 95% comparing with both the first-order approximation and the DS model. The measured $F-D$ curve fits with equation (5.7) using the least-squares fitting to determine the capillary volume V and the parameter c , respectively. These parameters were inputted into the DS model to predicate the exact meniscus shape of the capillary and to calculate the capillary force by using equation (5.16).

A simple method can be used if we want to obtain information on the shape of the capillary profile using the first-order approximation. When the saturation equilibrium condition is met, the radius of meniscus r can be determined by equation (5.5). By knowing the capillary volume V and the rotationally symmetrical characteristic of the capillary bridge, the capillary profile using the first-order approximation hence can be determined.

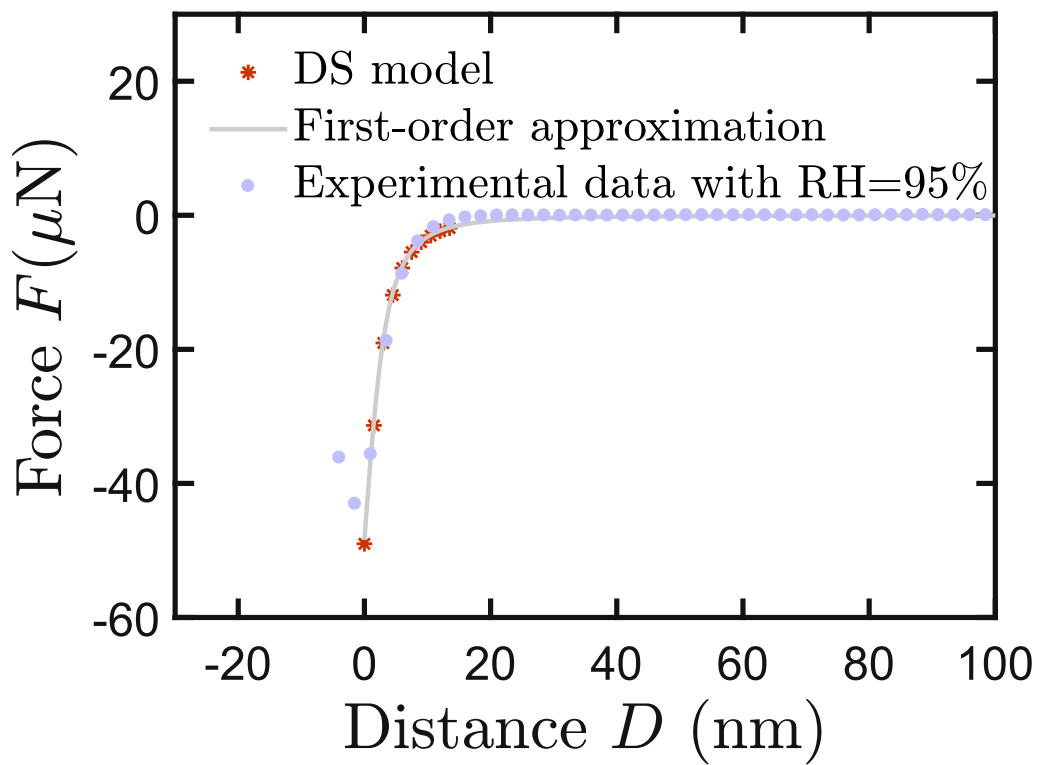


Figure 5.8 Experimental force-distance (F - D) curve (measured at a constant separation speed $1 \mu\text{m/s}$) in comparison with the predictions of: (a) the first-order approximation; (b) the DS model.

Figure 5.9(a) shows the quarter view of two liquid-bridge spheres using the data obtained from the experiment under RH 95%, (b) shows the capillary profile simulated by the DS model, in comparison with the circular profile assumed in the first-order approximation. The near-wall slope and the profile of the meniscus neck predicted by the two approaches are shown in (c) and (d), respectively. One can see a minor difference between the two solutions regarding the geometric shape of the meniscus. The length difference around the capillary neck is less than 0.01%. Figure 5.9 shows that the difference in the predictions between the approximation and the DS model is minor. Thus, the almost identical predictions of the F - D curves by the two approaches can then be reasonably explained by the geometric resemblance of two meniscus profiles.

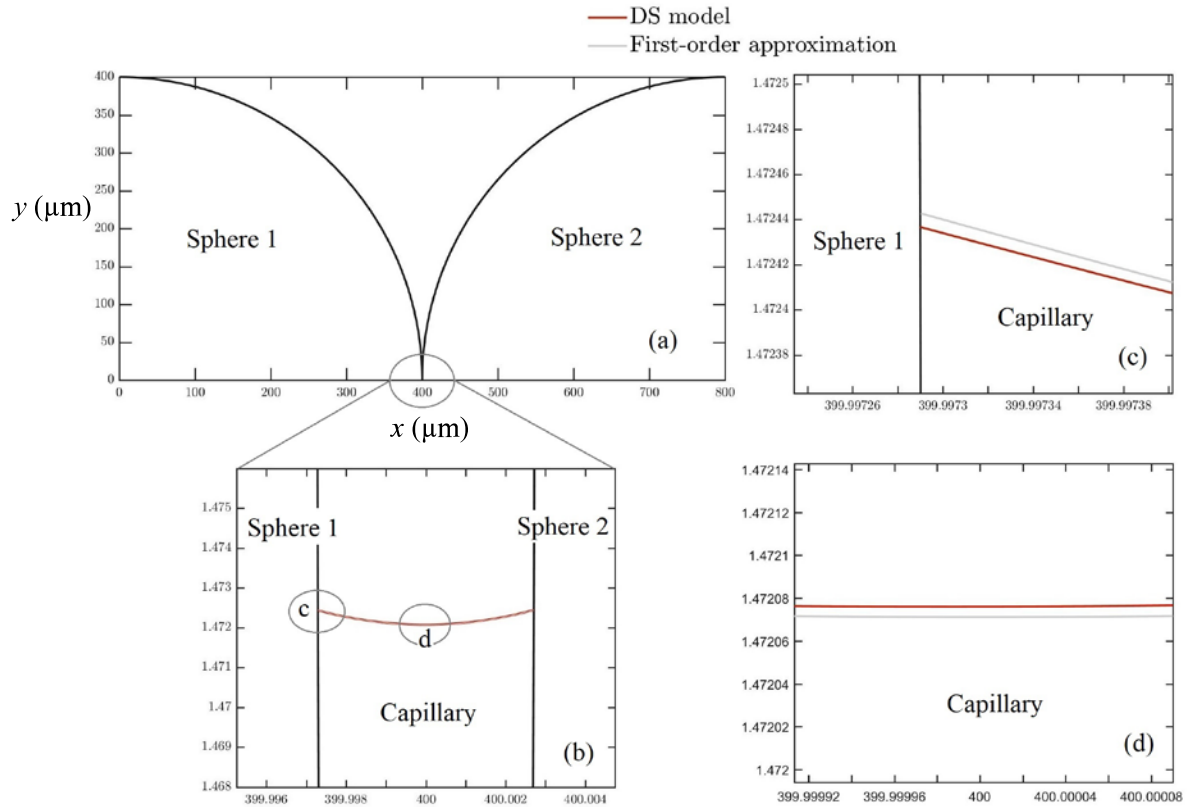


Figure 5.9 Capillary geometric boundary between two PMMA spheres using the DS model and first-order approximation (unit in μm); (a) quarter view of two liquid-bridge spheres; (b) the calculated shape of the meniscus, and the subtle difference of the predictions between the DS model and first-order approximation in: (c) the near-wall slope and (d) the profile of the meniscus neck.

Figure 5.10 shows the experimental measurements of the adhesion forces plotted against the RH. A significant increase of the adhesion force is observed with the RH changing from 60% to 95%. After fitting the experimental data with the surface roughness model using equations (5.19) and (5.22), the parameter describing the height of the asperity δ_0 is determined as 0.77 nm. For the RH at 95%, the meniscus radius r is calculated as 10.14nm, which is considerably larger than the δ_0 . For $r \gg \delta_0$, the dominating factor in the adhesion force F_{adh} is the particle radius R_s (in equation (5.9)), instead of the integrated height distribution $G(z)$ (in equation (5.19)) under the condition of a low RH. Therefore the roughness effect at RH 95% can be reasonably assumed negligible. For this reason, equation (5.9) is applicable for obtaining the parameter c , with the F_{adh} acquired from the experiment.

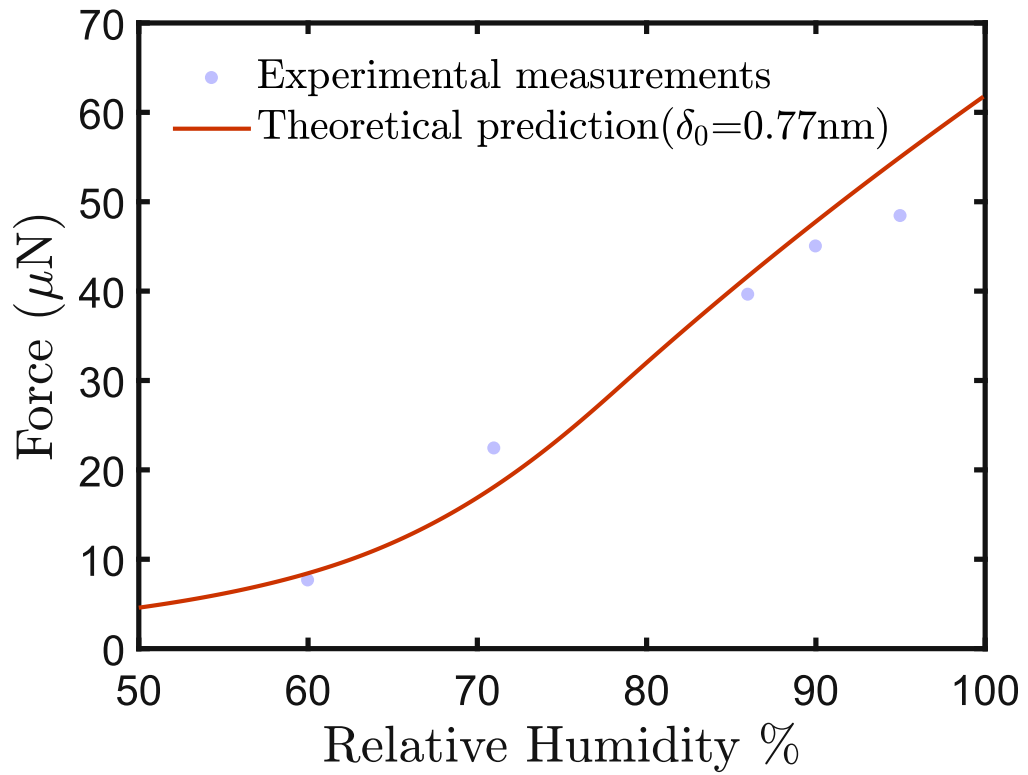


Figure 5.10 The adhesion force between two PMMA spheres under different RH compared with the theoretical predictions based on equations (5.19) and (5.22).

The filling angle of β is much less than the liquid contact angle θ ($\beta/\theta < 0.01$) for the current experiment, thus the parameter $c = \cos(\theta + \beta)$ can be simplified as $c \approx \cos \theta$. The contact angle of the three-phase solid-liquid-vapor interface is considered as the surface characteristic, which is associated with material chemistry and topography, and it remains constant regardless of the liquid droplet size on the solid surface and the ambient RH [209,210]. The parameter c and the contact angle θ are determined as $c = 0.27$ under the RH of 95% which corresponding to $\theta = 74.48^\circ$. The calculated θ is comparable with the value reported in the literature for PMMA-water interface (ca. 68°) [211].

Figure 5.11(a) shows the AFM topography scans (Z -height) of two representative PMMA sphere surfaces, and (b) shows the RMS roughness distribution maps in 8×8 pixels, which were extracted from the topography. Area average RMS roughness values were calculated for Area 1 and Area 2 of 2.2 ± 0.4 nm and 2.7 ± 0.4 nm, respectively. The obvious topographical features/defects (showed in substantial brighter color) was discarded when calculating the area average RMS roughness. Note that because the AFM was performed on a spherical surface, a polynomial background leveling algorithm [212] was used to level the surface before the data process (such as RMS roughness calculation) was carried out.

Figure 5.11(c) shows the asperity height distribution of surface roughness. Unlike the uniform distribution in Butt's model, the experimental data shows a typical Gaussian distribution pattern in reality. Fitted by the Gaussian probability density function, the standard deviation σ is calculated as 1.8 ± 0.4 (see Figure 5.7(b)).

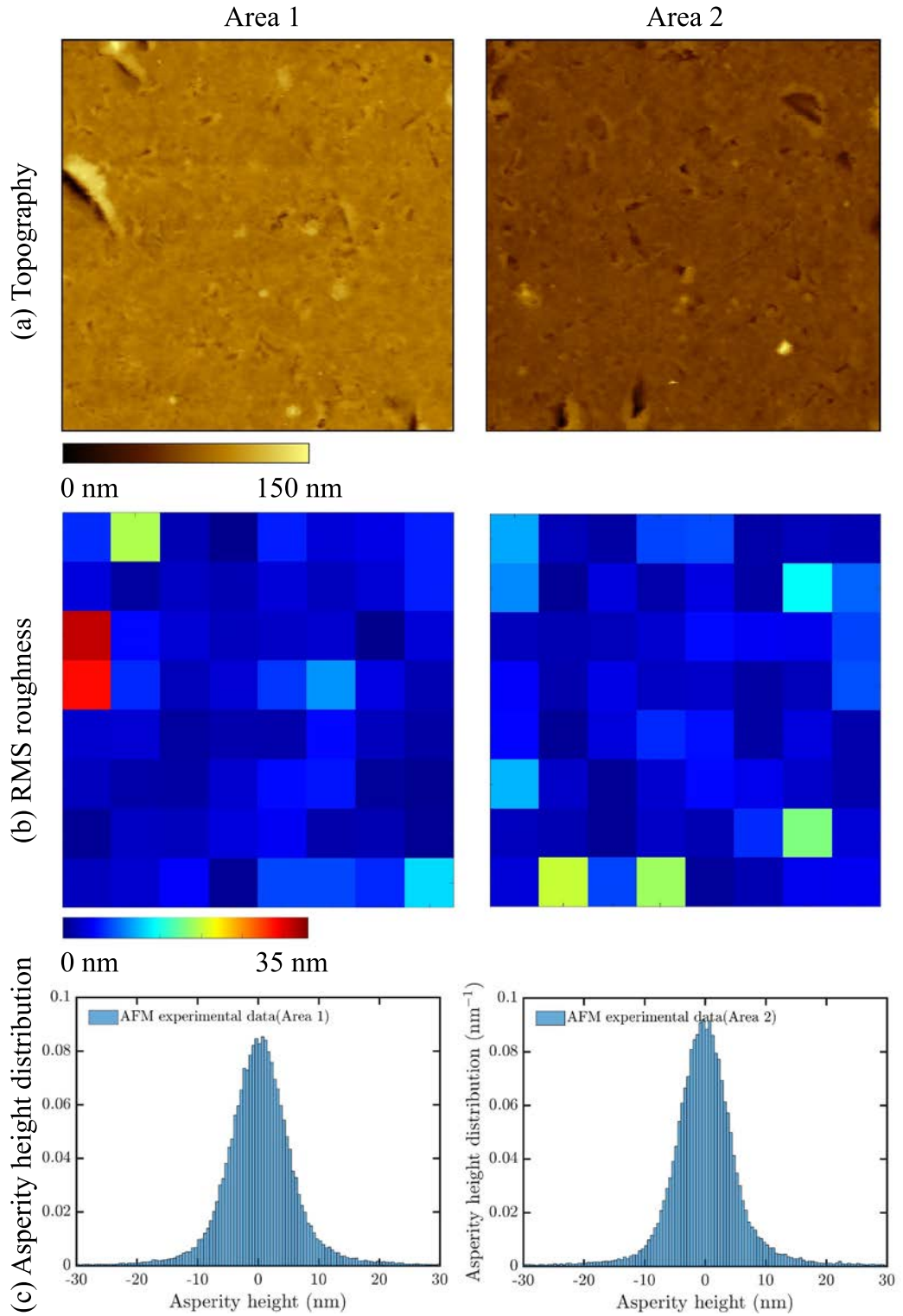


Figure 5.11 AFM measurements of (a) surface topography and (b) RMS roughness, carried out on two different areas from two different PMMA spheres (256 sampling points per line, $5 \times 5 \mu\text{m}^2$). The 8×8 pixels RMS distribution maps in (b) were constructed from the roughness heights of the topography in (a). (c) shows the measured asperity height distribution of surface roughness.

Figure 5.12 shows the theoretical joint surface roughness function φ_{Butt} based on Butt's uniformed asperity distribution calculated from equation (5.21). The experimental joint surface roughness function φ_{Exp} was calculated by convoluting two Gaussian distribution functions with the expectation parameter $\mu = 0$ and standard deviation $\sigma = 1.8$. The moderate discrepancy between φ_{Butt} and φ_{Exp} can be explained by the following reasons:

1. The AFM-measured surface roughness distribution shown in Figure 5.11(c) is more like a Gaussian distribution than a uniform distribution, as assumed by Butt.
2. Despite the fact that PMMA exhibits a relatively high Young's modulus (ca. 3 GPa), the finite deformation of the asperities can still occur due to the increased contact stress at the interface between the two particles.
3. At lower RH, meniscus that exists in a gap size comparable to a few molecular lengths may introduce mesoscopic effects such as non-continuum phenomena in the liquid [47]. Note that the calculated Kelvin length $\lambda_K = 0.52$ nm is roughly the same size of the water molecule diameter (ca. 0.28 nm).

Compared to the currently measured data, Butt's theory has demonstrated reasonable prediction in the surface roughness influencing the F - D curves. My new findings confirm that the humidity-dependent adhesion force can be modeled by the surface roughness distribution independently measured by AFM topography scan.

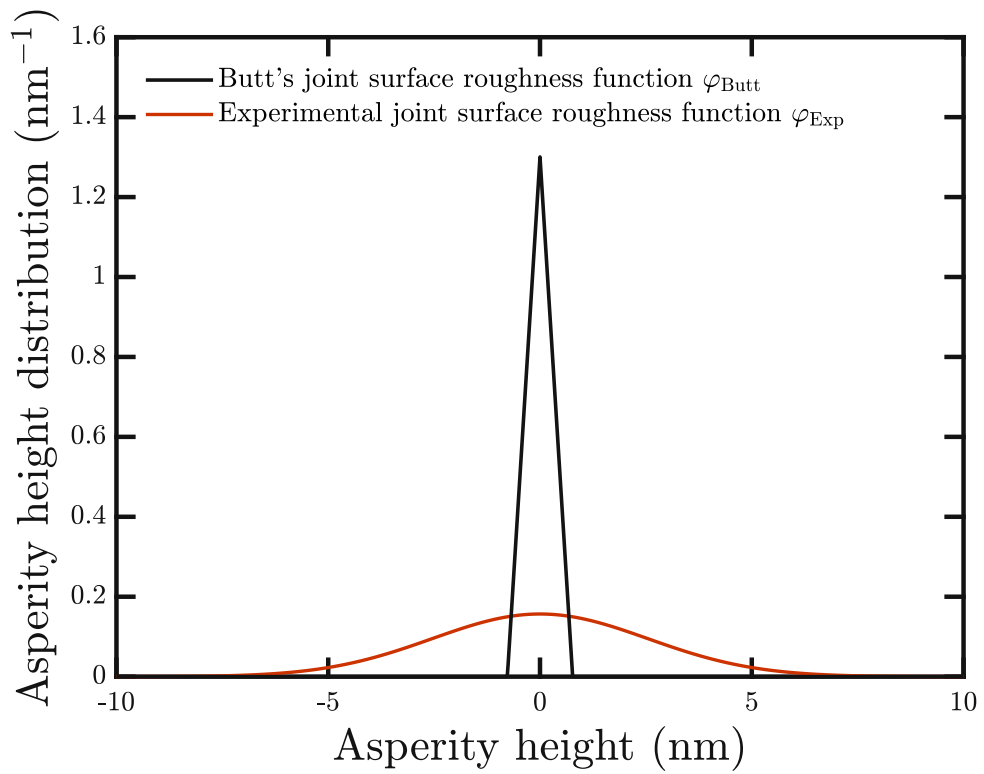


Figure 5.12 The comparison between Butt's joint surface roughness function φ_{Butt} calculated by the uniform surface roughness distribution and the joint surface roughness function φ_{Exp} calculated by the Gaussian distribution fitted by the experimental surface roughness data.

5.5 Summary

The constitutive relation $F(D)$ of detaching two identical adhering microspheres was measured and modeled as a function of RH. The first-order approximation and the numerical DS model have been applied to interpret the measured data. The results predicted by the two approaches have good agreement in terms of the capillary profile and the $F-D$ curve, and the estimated contact angle θ is comparable with the value reported in the literature. A surface roughness model has quantitatively interpreted the dependence between RH and the adhesion force, and the predicted surface roughness distribution has been evaluated in comparison with the AFM-scanned topography. The study demonstrates that the adhesion force increases with the increase of RH due to the effect of surface roughness.

6 Conclusions and future work

The experimental techniques, combined with the appropriate analyses, described in the thesis have facilitated the investigation of the capillary forces between microparticles. The current study has included both the measurement of the force-displacement response curve and the side-view image profile. Using the available theories, some of the important mechanical and interfacial properties (such as material deformability and surface roughness) have been properly estimated. For soft microparticles with capillary rises from the accumulation of absorbed liquid, the interfacial energy and mechanical properties such as Young's modulus have been calculated. For rigid microparticles with capillary rises from liquid condensation, the geometric shape of the capillary is calculated both numerically and analytically. The main specific conclusion of the current study can be summarized in the following major parts: (1) the governing effects responsible for the observed capillary forces, (2) the experimental method, and (3) the theoretical interpretations. They are summarized in the following sections.

6.1 The governing effects responsible for the observed capillary forces

There are some important effects which govern the capillary forces between two contacting microparticles. Although these effects, which are mentioned below, may be specified as unique mechanisms, most of them are often interrelated to each other in the actual cases.

1. *The deformability:* This effect has been shown to have a significant impact on the magnitude of the capillary forces between microspheres. For soft hydrogel spheres, due to relatively low Young's modulus, the spheres tend to deform by the direct impact of the capillary. The deformability of the sphere also affects the value of the modified Tabor parameter. The effect has been quantitatively described by the generalized Hertz theory and JKR theory. However, for the case of PMMA particle contact, in which the spheres are less deformable, this effect still awaits a detailed examination.
2. *Viscoelastic effects:* This effect plays an important role in the soft hydrogel microparticle mechanical response. In the current work, Young's modulus of soft microparticles exhibits a linear increase with the separation speed. The increase of Young's modulus directly affects the deformability of the particles. As described in the aforementioned paragraph, Young's modulus will eventually have an impact on the modified Tabor parameter which is the key parameter of choosing the appropriate contact mechanics theory.
3. *Surface roughness:* For PMMA spheres, the surface roughness shows to lower magnitude of the capillary forces due to the capillary only forming between surface asperities. The impact of surface roughness mitigates as the RH gradually increases. For soft hydrogel spheres, the surface roughness has not seen any effects on the magnitude of the capillary forces.

6.2 The experimental method

1. *The principle of the apparatus:* The current apparatus incorporates the force-displacement measurements with the side-image profile optical acquisition system to measure the system's crucial mechanical parameters such as

interfacial energy and Young's modulus accurately. The side-image profiles have been shown to provide critical information on the geometric shape of the capillary, the re-absorption process of the liquid, and the deformation behavior of the systems.

2. *The pole-to-pole particle alignment methods:* This technical problem has been recognized to be extremely difficult in many previous studies on the nano-/micro- particle-to-particle adhesion contact measurements. With the help of the precision *X-Y* axis stage and the side-image profile optical acquiring system, a perfect pole-to-pole particle alignment is achieved between the testing microparticles samples.
3. *The precision humidity control:* The precision humidity control system has been used to serve two main purposes. (1) Mitigates the evaporation effect of the hydrogel microparticles. (2) Regulate the liquid condensation process between rigid PMMA polymer microparticles.

6.3 The theoretical interpretation

6.3.1 For soft hydrogel microparticles with capillary rises from the accumulation of absorbed liquid

1. *The JKR theory and generalized Hertz theory:* The JKR theory has been shown to reconcile with the generalized Hertz theory, which takes capillary force into account for soft microspheres in a relationship that the work of adhesion is equal to twice the surface tension of water.
2. *The viscoelasticity model:* A Voigt model combined with the Hertz model has been used to quantitatively interpret the viscoelastic behavior of the hydrogel.

The current work demonstrates that while the work of adhesion is independent of the separation speed, Young's modulus, however, exhibits a linear increase.

6.3.2 For rigid microparticles with capillary rises from liquid condensation influenced by RH

1. *The first-order approximation and the numerical solution:* A first-order approximation derived based on the Kelvin equation and Young-Laplace equation have shown differences in the predictions of the geometric shape of the capillary, compared with those predicted by the DS numerical model.
2. *The RH dependent capillary force model:* A surface roughness model using the uniform asperity distribution assumptions has been used to quantitatively analyze the RH-dependent capillary force. The results show that the influences of surface roughness decrease with the increase of the RH, which is in good agreement with the experimental observations.

6.4 Future work

In terms of the objectives in this study, future work can be summarized as follows:

1. The scope of the current study is limited to the size of microparticles (ca. 200-1000 μm) due to the engineering aspect limitations of the current experimental and theoretical solutions. More advanced experimental and computational simulation methods are required to achieve a full scope of the scaling effect of the capillary forces. For nanometer-sized capillary, the fundamental continuum medium hypothesis needs to be re-examined.
2. The materials are treated as rigid or linear elastic in the current study. However, hyperelasticity is very common among rubber-like materials, especially for materials with relatively low Young's modulus. More advanced models such as

the Mooney-Rivlin model and the Arruda-Boyce model are expected to achieve a more accurate description of the mechanical properties of the testing samples with the help of the Finite Element Method (FEM).

3. The current study focuses on the water capillary in a vapor environment; however, it has been shown that the property of the liquid and the surrounding medium has the same effects on the magnitude of the capillary force. Different types of liquid might exhibit very different behaviors; for example, for the liquid with much higher density, the gravitational effect may become much noticeable. Thus, further investigations of different mediums with different physical and chemical properties are expected.

References

- [1] D.A. Hammer, M. Tirrell, Biological adhesion at interfaces, *Annu. Rev. Mater. Sci.* 26 (1996) 651–691.
- [2] L. Picard, P. Phalip, E. Fleury, F. Ganachaud, Chemical adhesion of silicone elastomers on primed metal surfaces: A comprehensive survey of open and patent literatures, *Prog. Org. Coatings*. 80 (2015) 120–141.
- [3] R. Mukherjee¹, K. Sen, L. Fontana, C. Mao, B. Chaudhuri, Quantification of moisture-induced cohesion in pharmaceutical mixtures, *J. Pharm. Sci.* 108 (2019) 223–233.
- [4] E.C. Montes, N.A. Santamaría, J.-C. Gummy, P. Marchal, Moisture-induced caking of beverage powders, *J. Sci. Food Agric.* 91 (2011) 2582–2586.
- [5] S. Rønneberg, C. Laforte, C. Volat, J. He, Z. Zhang, The effect of ice type on ice adhesion, *AIP Adv.* 9 (2019) 055304.
- [6] P. Capra, G. Musitelli, P. Perugini, Wetting and adhesion evaluation of cosmetic ingredients and products: correlation of in vitro–in vivo contact angle measurements, *Int. J. Cosmet. Sci.* 39 (2017) 393–401.
- [7] J. Lister, B. Ennis, *The science and engineering of granulation processes*, Kluwer Academic Publisher, London, 2004.
- [8] F. Podczeck, J.M. Newton, M.B. James, Adhesion and friction between powders and polymer or aluminium surfaces determined by a centrifuge technique, *Powder Technol.* 83 (1995) 201–209.
- [9] C. Meier, R. Weissbach, J. Weinberg, W.A. Wall, A.J. Hart, Critical influences of particle size and adhesion on the powder layer uniformity in metal additive manufacturing, *J. Mater. Process. Technol.* 266 (2019) 484–501.
- [10] X. Wang, Z. Zhang, O. Torsæter, J. He, Atomistic insights into the nanofluid transport through an ultra-confined capillary, *Phys. Chem. Chem. Phys.* 20 (2018) 4831–4839.
- [11] S. Beaudoin, P. Jaiswal, A. Harrison, J. Laster, K. Smith, M. Sweat, M. Thomas, Fundamental forces in particle adhesion, in: *Part. Adhes. Remov.*, 1st ed., MA: Wiley-Scrivener, Berverly, 2015.
- [12] A. Zimon, *Adhesion of dust and powder*, 2nd ed., Consultants Bureau, New York, 1982.
- [13] N. Zarate, *The influence of interfacial condensed moisture on adhesion between solid organic particles and surfaces*, Purdue University, West Lafayette, IN, USA, 2010.
- [14] D.L. Sedin, K.L. Rowlen, Adhesion forces measured by atomic force microscopy in humid air, *Anal. Chem.* 72 (2000) 2183–2189.
- [15] N. Hosoda, S.N. Gorb, Underwater locomotion in a terrestrial beetle: Combination of surface de-wetting and capillary forces, *Proc. R. Soc. B Biol. Sci.* 279 (2012) 4236–4242.
- [16] M.E. Fisher, H. Nakanishi, Scaling theory for the criticality of fluids between plates, *J. Chem. Phys.* 75 (1981) 5857–5863.

- [17] M.M. Kohonen, H.K. Christenson, Capillary condensation from vapors of n-Hexane/Perfluoro-n-hexane mixtures, *J. Phys. Chem. B.* 106 (2002) 6685–6695.
- [18] H. Shinto, K. Uranishi, M. Miyahara, K. Higashitani, Wetting-induced interaction between rigid nanoparticle and plate: A Monte Carlo study, *J. Chem. Phys.* 116 (2002) 9500–9509.
- [19] J. Jang, G.C. Schatz, M.A. Ratner, Liquid meniscus condensation in dip-pen nanolithography, *J. Chem. Phys.* 116 (2002) 3875–3886.
- [20] J. Jang, M. Yang, G. Schatz, Microscopic origin of the humidity dependence of the adhesion force in atomic force microscopy, *J. Chem. Phys.* (2007) 174705.
- [21] P. Lambert, A. Chau, A. Delchambre, Comparison between two capillary forces models, *Langmuir.* 24 (2008) 3157–3163.
- [22] J.S. McFarlane, D. Tabor, Adhesion of solids and the effect of surface films, *Proc. R. Soc. London. A.* 202 (1950) 224–243.
- [23] C.C. Harris, N.R. Morrow, Pendular moisture in packings of equal spheres, *Nature.* 203 (1964) 706–708.
- [24] H.-J. Butt, M. Kappl, Normal capillary forces, *Adv. Colloid Interface Sci.* 146 (2009) 48–60.
- [25] G. Binnig, C.F. Quate, Atomic force microscope, *Phys. Rev. Lett.* 56 (1986) 930–933.
- [26] M. Schenk, M. Fütting, R. Reichelt, Direct visualization of the dynamic behavior of a water meniscus by scanning electron microscopy, *J. Appl. Phys.* 84 (1998) 4880–4884.
- [27] W.A. Ducker, T.J. Senden, R.M. Pashley, Direct measurement of colloidal forces using an atomic force microscope, *Nature.* 354 (1991) 239–241.
- [28] H.-J. Butt, Electrostatic interaction in atomic force microscopy, *Biophys. J.* 60 (1991) 777–785.
- [29] A.J. Harrison, D.S. Corti, S.P. Beaudoin, Capillary forces in nanoparticle adhesion: A review of AFM methods, *Part. Sci. Technol.* 33 (2015) 526–538.
- [30] M. Farshchi-Tabrizia, M. Kappl, H.-J. Butt, Influence of humidity on adhesion: An atomic force microscope study, *J. Adhes. Sci. Technol.* 22 (2008) 181–203.
- [31] A. Ptak, H. Gojzewski, M. Kappl, H.-J. Butt, Influence of humidity on the nanoadhesion between a hydrophobic and a hydrophilic surface, *Chem. Phys. Lett.* 503 (2011) 66–70.
- [32] N. V. Zarate, A.J. Harrison, J.D. Litster, S.P. Beaudoin, Effect of relative humidity on onset of capillary forces for rough surfaces, *J. Colloid Interface Sci.* 411 (2013) 265–272.
- [33] R. Jones, H.M. Pollock, J.A.S. Cleaver, C.S. Hodges, Adhesion forces between glass and silicon surfaces in air studied by AFM: Effects of relative humidity, particle size, roughness, and surface treatment, *Langmuir.* 18 (2002) 8045–8055.
- [34] J. Jang, G.C. Schatz, M.A. Ratner, Capillary force in atomic force microscopy, *J. Chem. Phys.* 120 (2004) 1157–1160.
- [35] M. He, A.S. Blum, D.E. Aston, C. Buenviaje, R.M. Overney, R. Luginbühl, Critical phenomena of water bridges in nanoasperity contacts, *J. Chem. Phys.* 114 (2001)

1355–1360.

- [36] A. Ata, Y.I. Rabinovich, R.K. Singh, Role of surface roughness in capillary adhesion, *J. Adhes. Sci. Technol.* 16 (2002) 337–346.
- [37] F.W. DelRio, M.L. Dunn, L.M. Phinney, C.J. Bourdon, M.P. de Boer, Rough surface adhesion in the presence of capillary condensation, *Appl. Phys. Lett.* 90 (2007) 163104.
- [38] P.J. van Zwol, G. Palasantzas, J.T.M. De Hosson, Influence of random roughness on the adhesion between metal surfaces due to capillary condensation, *Appl. Phys. Lett.* 91 (2007) 101905.
- [39] P.J. van Zwol, G. Palasantzas, J.T.M. De Hosson, Influence of roughness on capillary forces between hydrophilic surfaces, *Phys. Rev. E.* 78 (2008) 031606.
- [40] M.P. de Boer, Capillary adhesion between elastically hard rough surfaces, *Exp. Mech.* 47 (2007) 171–183.
- [41] A.P. Tetuko, D.S. Khaerudini, P. Sardjono, P. Sebayang, G. Rosengarten, Superhydrophobic surface as a fluid enhancement material in engineering applications, *AIP Conf. Proc.* 1555 (2013) 3–6.
- [42] G. Greci, G. Birarda, E. Mitri, L. Businaro, S. Pacor, L. Vaccari, M. Tormen, Optimization of microfluidic systems for IRMS long term measurement of living cells, *Microelectron. Eng.* 98 (2012) 698–702.
- [43] L. Sirghi, R. Szoszkiewicz, E. Riedo, Volume of a nanoscale water bridge, *Langmuir.* 22 (2006) 1093–1098.
- [44] Y.I. Rabinovich, A. Singh, M. Hahn, S. Brown, B. Moudgil, Kinetics of liquid annulus formation and capillary forces, *Langmuir.* 27 (2011) 13514–13523.
- [45] J.N. Israelachvili, D. Tabor, The measurement of van der Waals dispersion forces in the range 1.5 to 130 nm, *Proc. R. Soc. London. A.* 331 (1972) 19–38.
- [46] TABOR D, WINTERTON RHS, The direct measurement of normal and retarded van der Waals forces, *Proc. R. Soc. London. A.* 312 (1969) 435–450.
- [47] R.L. Fisher, J.N. Israelachvili, Experimental studies on the applicability of Kelvin equation to highly curved concave menisci, *J. Colloid Interface Sci.* 80 (1981) 528–541.
- [48] M.M. Kohonen, H.K. Christenson, Capillary condensation of water between rinsed mica surfaces, *Langmuir.* 16 (2000) 7285–7288.
- [49] H.K. Christenson, Adhesion between surfaces in undersaturated vapors-A reexamination of the influence of meniscus curvature and surface forces, *J. Colloid Interface Sci.* 121 (1988) 170–178.
- [50] E.J. Wanless, H.K. Christenson, Interaction between surfaces in ethanol: Adsorption, capillary condensation, and solvation forces, *J. Chem. Phys.* 101 (1994) 4260–4267.
- [51] H.K. Christenson, Capillary condensation due to van der Waals attraction in wet slits, *Phys. Rev. Lett.* 73 (1994) 1821–1824.
- [52] J.E. Curry, H.K. Christenson, Adsorption, wetting, and capillary condensation of nonpolar fluids in mica slits, *Langmuir.* 12 (1996) 5729–5735.
- [53] M.M. Kohonen, N. Maeda, H.K. Christenson, Kinetics of capillary condensation in a nanoscale pore, *Phys. Rev. Lett.* 82 (1999) 4667–4670.

- [54] N. Maeda, M.M. Kohonen, H.K. Christenson, Phase behavior of long-chain n-Alkanes at one and between two mica surfaces, *J. Phys. Chem. B.* 105 (2001) 5906–5913.
- [55] N. Maeda, Phase transitions of capillary-held liquids in a slit-like pore, *J. Phys. Chem. B.* 110 (2006) 25982–25993.
- [56] H.K. Christenson, Capillary condensation in systems of immiscible liquids, *J. Colloid Interface Sci.* 104 (1984) 234–249.
- [57] J.N. Israelachvili, Thin film studies using multiple-beam interferometry, *J. Colloid Interface Sci.* 44 (1973) 259–272.
- [58] G. Böhme, H. Rabenhost, G. Sandstede, Adhesion measurements involving small particles, *Tran. Instn. Chem. Engrs.* 40 (1962) 252–259.
- [59] S.W. Booth, J.M. Newton, Experimental investigation of adhesion between powders and surfaces, *J. Pharm. Pharmacol.* 39 (1987) 679–684.
- [60] T.T. Nguyen, C. Rambanapasi, A.H. de Boer, H.W. Frijlink, P.M. v. D. Ven, J. de Vries, H.J. Busscher, K. v.D. Voort Maarschalk, A centrifuge method to measure particle cohesion forces to substrate surface: The use of a force distribution concept for data interpretation, *Int. J. Pharm.* 393 (2010) 88–95.
- [61] S. You, M.P. Wan, Modeling and experiments of the adhesion force distribution between particles and a surface, *Langmuir.* 30 (2014) 6808–6818.
- [62] T. Brunschwiler, G. Schlottig, S. Ni, Y. Liu, J. V. Goicochea, J. Zürcher, H. Wolf, Formulation of percolating thermal underfills using hierarchical self-assembly of micro- and nanoparticles by centrifugal forces and capillary bridging, *Proc. 2012 45th Int. Symp. Microelectron. IMAPS 2012.* (2012) 749–759.
- [63] U. Beck, G. Reiners, D. Lerche, U. Rietz, H. Niederwald, Quantitative adhesion testing of optical coatings by means of centrifuge technology, *Surf. Coatings Technol.* 205 (2011) S182–S186.
- [64] P.G.C. Petean, M.L. Aguiar, Determining the adhesion force between particles and rough surfaces, *Powder Technol.* 274 (2015) 67–76.
- [65] Z. Fournier, D. Geromichalos, S. Herminghaus, M.M. Kohonen, F. Mugele, M. Scheel, M. Schulz, B. Schulz, C. Schier, R. Seemann, A. Skudelny, Mechanical properties of wet granular materials, *J. Phys. Condens. Matter.* 17 (2005) S477–S502.
- [66] E. Bayramli, T.G.M. Van De Ven, An experimental study of liquid bridges between spheres in a gravitational field, *J. Colloid Interface Sci.* 116 (1987) 490–502.
- [67] M.M. Kohonen, D. Geromichalos, M. Scheel, C. Schier, S. Herminghaus, On capillary bridges in wet granular materials, *Phys. A Stat. Mech. Its Appl.* 339 (2004) 7–15.
- [68] G.D. Danilatos, Foundations of environmental scanning electron microscopy, *Adv. Electron. Electron Phys.* 71 (1988) 109–250.
- [69] G.D. Danilatos, Review and outline of environmental SEM at present, *J. Microsc.* 162 (1991) 391–402.
- [70] B.L. Weeks, M.W. Vaughn, J.J. Deyoreo, Direct imaging of meniscus formation in atomic force microscopy using environmental scanning electron microscopy, *Langmuir.* 21 (2005) 8096–8098.

- [71] B. Zhao, H. Zeng, Y. Tian, J. Israelachvili, Adhesion and detachment mechanisms of sugar surfaces from the solid(glassy) to liquid(viscous) states, *Proc. Natl. Acad. Sci. U. S. A.* 103 (2006) 19624–19629.
- [72] H.J. Butt, B. Cappella, M. Kappl, Force measurements with the atomic force microscope: Technique, interpretation and applications, *Surf. Sci. Rep.* 59 (2005) 1–152.
- [73] T.C. Halsey, A.J. Levine, How sandcastles fall, *Phys. Rev. Lett.* 80 (1998) 3141–3144.
- [74] R.A. Fisher, On the capillary forces in an ideal soil; correction of formulae given by W. B. Haines, *J. Agric. Sci.* 16 (1926) 492–505.
- [75] W.B. Haines, Studies in the physical properties of soils. A note on the cohesion developed by capillary forces in an ideal soil., *J. Agric. Sci.* 15 (1925) 529–535.
- [76] W.B. Haines, Studies in the physical properties of soils. A further contribution to the theory of capillary phenomena in soil., *J. Agric. Sci.* 17 (1927) 264–290.
- [77] M. Scheel, R. Seemann, M. Brinkmann, M. Di Michiel, A. Sheppard, B. Breidenbach, S. Herminghaus, Morphological clues to wet granular pile stability, *Nat. Mater.* 7 (2008) 189–193.
- [78] Y.I. Rabinovich, J.J. Adler, M.S. Esayanur, A. Ata, R.K. Singh, B.M. Moudgil, Capillary forces between surfaces with nanoscale roughness, *Adv. Colloid Interface Sci.* 96 (2002) 213–230.
- [79] M. D’Amore, G. Donsi, L. Massimilla, The influence of bed moisture on fluidization characteristics of fine powders, *Power Technol.* 23 (1979) 253–259.
- [80] A.A. Feiler, J. Stiernstedt, K. Theander, P. Jenkins, M.W. Rutland, Effect of capillary condensation on friction force and adhesion, *Langmuir.* 23 (2007) 517–522.
- [81] A. Opitz, S.I.-U. Ahmed, J.A. Schaefer, M. Scherge, Nanofriction of silicon oxide surface covered with thin water films, *Wear.* 254 (2003) 924–929.
- [82] R.J. Hunter, *Foundations of colloid science*, 2nd ed., Oxford University Press, Oxford, 2001.
- [83] J. Pellicer, J.A. Manzanares, S. Mafé, The physical description of elementary surface phenomena: Thermodynamics versus mechanics, *Am. J. Phys.* 63 (1995) 542–547.
- [84] R.C. Brown, The fundamental concepts concerning surface tension and capillarity, *Proc. Phys. Soc.* 59 (1947) 429–448.
- [85] M. Sophocleous, Understanding and explaining surface tension and capillarity: an introduction to fundamental physics for water professionals, *Hydrogeol. J.* 18 (2010) 811–821.
- [86] J.J. Bikerman, *Physical surfaces*, Academic, New York, 2012.
- [87] M. V. Berry, The molecular mechanism of surface tension, *Phys. Educ.* 6 (1971) 79–84.
- [88] A.W. Adamson, A.P. Gast, *Physical chemistry of surfaces*, Interscience publishers, New York, 1967.
- [89] J.-L. Liu, X.-Q. Feng, On elastocapillarity: A review, *Acta Mech. Sin.* 28 (2012) 928–940.

- [90] M.A. Erle, D.C. Dyson, N.R. Morrow, Liquid bridges between cylinders, in a torus, and between spheres, *AIChE J.* 17 (1971) 115–121.
- [91] F.M. Orr, L.E. Scriven, A.P. Rivas, Pendular rings between solids: Meniscus properties and capillary force, *J. Fluid Mech.* 67 (1975) 723–742.
- [92] D. Megias-Alguacil, L.J. Gauckler, Accuracy of the toroidal approximation for the calculus of concave and convex liquid bridges between particles, *Granul. Matter.* 13 (2011) 487–492.
- [93] G. Lian, C. Thornton, M.J. Adams, A theoretical study of the liquid bridge forces between two rigid spherical bodies, *J. Colloid Interface Sci.* 161 (1993) 138–147.
- [94] N.P. Kruyt, O. Millet, An analytical theory for the capillary bridge force between spheres, *J. Fluid Mech.* 812 (2017) 129–151.
- [95] L.D. Gelb, K.E. Gubbins, R. Radhakrishnan, M. Sliwinska-Bartkowiak, Phase separation in confined systems, *Reports Prog. Phys.* 62 (1999) 1573–1659.
- [96] M. Thommes, K.A. Cychosz, Physical adsorption characterization of nanoporous materials: progress and challenges, *Adsorption.* 20 (2014) 233–250.
- [97] Y. Longa, M. Sliwinska-Bartkowiak, H. Drozdowski, M. Kempinski, K.A. Phillips, J.C. Palmer, K.E. Gubbins, High pressure effect in nanoporous carbon materials: Effects of pore geometry, *Colloids Surfaces A Physicochem. Eng. Asp.* 437 (2020) 33–41.
- [98] D.R. Cole, S. Ok, A. Striolo, A. Phan, Hydrocarbon behavior at nanoscale interfaces, *Rev. Mineral. Geochemistry.* 75 (2013) 495–545.
- [99] R. Evans, P. Tarazona, Theory of condensation in narrow capillaries, *Phys. Rev. Lett.* 52 (1984) 557–560.
- [100] L.R. Fisher, R.A. Gamble, J. Middlehurst, The Kelvin equation and the capillary condensation of water, *Nature.* 290 (1981) 575–576.
- [101] E. Barsotti, S.P. Tan, S. Saraji, M. Piri, J. Chen, A review on capillary condensation in nanoporous media : Implications for hydrocarbon recovery from tight reservoirs, *Fuel.* 184 (2016) 344–361.
- [102] J. Rouquerol, F. Rouquerol, P. Llewellyn, G. Maurin, K.S. Sing, *Adsorption by powders and porous solids: principles, methodology and applications*, Academic press, 2013.
- [103] S.P. Tan, M. Piri, Equation-of-state modeling of associating-fluids phase equilibria in nanopores, *Fluid Phase Equilib.* 405 (2015) 157–166.
- [104] J.G. Powles, On the validity of the Kelvin equation, *J. Phys. A Gen. Phys.* 18 (1985) 1551–1560.
- [105] S. Naumov, R. Valiullin, P.A. Monson, J. Kärger, Probing memory effects in confined fluids via diffusion measurements, *Langmuir.* 24 (2008) 6429–6432.
- [106] S. Naumov, R. Valiullin, P.A. Monson, J. Kärger, Direct experimental verification of the Kelvin equation for capillary condensation, *Nature.* 277 (1979) 548–549.
- [107] S. Kim, D. Kim, J. Kim, S. An, W. Jhe, Direct evidence for curvature-dependent surface tension in capillary condensation: Kelvin equation at molecular scale, *Phys. Rev. X.* 8 (2018) 041046.
- [108] P.N. Aukett, N. Quirke, S. Riddiford, S.R. Tennison, Methane adsorption on

- microporous carbons-A comparison of experiment, theory, and simulation, *Carbon* N. Y. 30 (1992) 913–924.
- [109] K.L. Johnson, K. Kendall, A.D. Roberts, Surface energy and the contact of elastic solids, *Proc. R. Soc. London. A. Math. Phys. Sci.* 324 (1971) 301–313.
- [110] B.V. Derjaguin, V.M. Muller, Y.P. Toporov, Effect of contact deformation on the adhesion of elastic solids, *J. Colloid Interface Sci.* 53 (1975) 314–326.
- [111] A. Fogden, L.R. White, Contact elasticity in the presence of capillary condensation I. The nonadhesive Hertz problem, *J. Colloid Interface Sci.* 138 (1990) 414–430.
- [112] D. Maugis, B. Gauthier-Manuel, JKR-DMT transition in the presence of a liquid meniscus, *J. Adhes. Sci. Technol.* 8 (1994) 1311–1322.
- [113] E. Barthel, On the description of the adhesive contact of spheres with arbitrary interaction potentials, *J. Colloid Interface Sci.* 200 (1998) 7–18.
- [114] H.-J. Butt, J.T. Pham, M. Kappl, Forces between a stiff and a soft surface, *Curr. Opin. Colloid Interface Sci.* 27 (2017) 82–90.
- [115] H. Hertz, Ueber die Berührung fester elastischer Körper, *J. Reine Angew. Math.* 92 (1882) 156–171.
- [116] V.M. Muller, B.V. Derjaguin, Y.P. Toporov, On two methods of calculation of the force of sticking of an elastic sphere to a rigid plane, *Colloids Surf.* 7 (1983) 251–259.
- [117] M.D. Pashley, Further consideration of the DMT model for elastic contact, *Colloids Surf.* 12 (1984) 69–77.
- [118] D. Tabor, Surface forces and surface interactions, *J. Colloid Interface Sci.* 58 (1977) 2–13.
- [119] V.M. Muller, V.S. Yushchenko, B.V. Derjaguin, On the influence of molecular forces on the deformation of an elastic sphere and its sticking to a rigid plane, *J. Colloid Interface Sci.* 77 (1980) 91–101.
- [120] V.M. Muller, V.S. Yushchenko, B.V. Derjaguin, General theoretical consideration of the influence of surface forces on contact deformations and the reciprocal adhesion of elastic spherical particles, *J. Colloid Interface Sci.* 92 (1983) 92–101.
- [121] D. Maugis, Adhesion of spheres: The JKR-DMT transition using a dugdale model, *J. Colloid Interface Sci.* 150 (1992) 243–269.
- [122] K.L. Johnson, J.A. Greenwood, An adhesion map for the contact of elastic spheres, *J. Colloid Interface Sci.* 333 (1997) 326–333.
- [123] J.A. Greenwood, K.L. Johnson, An alternative to the Maugis model of adhesion between elastic spheres, *J. Phys. D. Appl. Phys.* 31 (1998) 3279–3290.
- [124] K.L. Johnson, Adhesion and friction between a smooth elastic spherical asperity and a plane surface, *Proc. R. Soc. A Math. Phys. Eng. Sci.* 453 (1997) 163–179.
- [125] K.-S. Kim, R.M. McMeeking, K.L. Johnson, Adhesion, slip, cohesive zones and energy fluxes for elastic spheres in contact, *J. Mech. Phys. Solids.* 46 (1998) 243–266.
- [126] H. Yao, H. Gao, Optimal shapes for adhesive binding between two elastic bodies, *J. Colloid Interface Sci.* 298 (2006) 564–572.

- [127] M. Berhanu, A. Kudrolli, Heterogeneous structure of granular aggregates with capillary interactions, *Phys. Rev. Lett.* 105 (2010) 098002.
- [128] L. Bocquet, E. Charlaix, S. Ciliberto, J. Crassous, Moisture-induced ageing in granular media and the kinetics of capillary condensation, *Nature*. 396 (1998) 735–737.
- [129] Y.S. Chu, S. Dufour, J.P. Thiery, E. Perez, F. Pincet, Johnson-Kendall-Roberts theory applied to living cells, *Phys. Rev. Lett.* 94 (2005) 028102.
- [130] J.P. Shelby, J. White, K. Ganesan, P.K. Rathod, D.T. Chiu, A microfluidic model for single-cell capillary obstruction by *Plasmodium falciparum*-infected erythrocytes, *Proc. Natl. Acad. Sci. U. S. A.* 100 (2003) 14618–14622.
- [131] G. Hanna, W.J.P. Barnes, Adhesion and detachment of the toe pads of tree frogs, *J. Exp. Biol.* 155 (1991) 103–125.
- [132] W. Federle, T. Endlein, Locomotion and adhesion: dynamic control of adhesive surface contact in ants, *Arthropod Struct. Dev.* 33 (2004) 67–75.
- [133] O. Betz, G. Kölsch, The role of adhesion in prey capture and predator defence in arthropods, *Arthropod Struct. Dev.* 33 (2004) 3–30.
- [134] W.J.P. Barnes, Biomimetic solutions to sticky problems, *Science* (80-.). 318 (2007) 203–204.
- [135] E. Arzt, S. Gorb, R. Spolenak, From micro to nano contacts in biological attachment devices, *Proc. Natl. Acad. Sci. U. S. A.* 100 (2003) 10603–10606.
- [136] F. Zhao, D. Yao, R. Guo, L. Deng, A. Dong, J. Zhang, Composites of polymer hydrogels and nanoparticulate systems for biomedical and pharmaceutical applications, *Nanomaterials*. 5 (2015) 2054–2130.
- [137] J.B. Sokoloff, Effects of capillary forces on a hydrogel sphere pressed against a surface, *Langmuir*. 32 (2016) 135–139.
- [138] K. Farzarian, A. Ghahremaninezhad, The effect of the capillary forces on the desorption of hydrogels in contact with a porous cementitious material, *Mater. Struct.* 50 (2017) 216.
- [139] D. Xu, K.M. Liechti, K. Ravi-Chandar, On the modified Tabor parameter for the JKR-DMT transition in the presence of a liquid meniscus, *J. Colloid Interface Sci.* 315 (2007) 772–785.
- [140] X. Xue, A.A. Polycarpou, Meniscus model for noncontacting and contacting sphere-on-flat surfaces including elastic-plastic deformation, *J. Appl. Phys.* 103 (2008) 023502.
- [141] H.J. Butt, W.J.P. Barnes, A. Del Campo, M. Kappl, F. Schönfeld, Capillary forces between soft, elastic spheres, *Soft Matter*. 6 (2010) 5930–5936.
- [142] N.L. Cross, R.G. Picknett, The liquid layer between a sphere and a plane surface, *Trans. Faraday Soc.* 59 (1963) 846–855.
- [143] H.M. Princen, I.Y.Z. Zia, S.G. Mason, Measurement of interfacial tension from the shape of a rotating drop, *J. Colloid Interface Sci.* 23 (1967) 99–107.
- [144] J.N. Israelachvili, *Intermolecular and surface forces*, 3rd ed., Academic press, Burlington, MA, USA, 2010.
- [145] H.J. Butt, Capillary forces: Influence of roughness and heterogeneity, *Langmuir*. 24

(2008) 4715–4721.

- [146] M. Farshchi-Tabrizi, M. Kappl, Y. Cheng, J. Gutmann, H.-J. Butt, On the adhesion between fine particles and nanocontacts: An atomic force microscope study, *Langmuir*. 22 (2006) 2171–2184.
- [147] J. Sprakel, N.A.M. Besseling, M.A. Cohen Stuart, F.A.M. Leermakers, Capillary adhesion in the limit of saturation: Thermodynamics, self-consistent field modeling and experiment, *Langmuir*. 24 (2008) 1308–1317.
- [148] A. Çolak, H. Wormeester, H.J.W. Zandvliet, B. Poelsema, Surface adhesion and its dependence on surface roughness and humidity measured with a flat tip, *Appl. Surf. Sci.* 258 (2012) 6938–6942.
- [149] A. Çolak, H. Wormeester, H.J.W. Zandvliet, B. Poelsema, The influence of instrumental parameters on the adhesion force in a flat-on-rough contact geometry, *Appl. Surf. Sci.* (2015) 1285–1290.
- [150] D. Maugis, Adhesion of spheres: The JKR-DMT transition using a Dugdale model, *J. Colloid Interface Sci.* 150 (1992) 243–269.
- [151] S. Gupta, S.K. Kundu, J. Stellbrink, L. Willner, J. Allgaier, D. Richter, Advanced rheological characterization of soft colloidal model systems, *J. Phys. Condens. Matter*. 24 (2012) 464102.
- [152] Y. Wang, X. Tang, G. Nian, Z. Suo, Strength and toughness of adhesion of soft materials measured in lap shear, *J. Mech. Phys. Solids*. 143 (2020) 103988.
- [153] M.G. Mazza, The physics of biofilms - an introduction, *J. Phys. D. Appl. Phys.* 49 (2016) 203001.
- [154] S. Leroch, M. Wendland, Influence of capillary bridge formation onto the silica nanoparticle interaction studied by grand canonical Monte Carlo simulations, *Langmuir*. 29 (2013) 12410–12420.
- [155] X. Xu, A. Jagota, C.Y. Hui, Effects of surface tension on the adhesive contact of a rigid sphere to a compliant substrate, *Soft Matter*. 10 (2014) 4625–4632.
- [156] X. Zhu, W. Xu, Effect of surface tension on the behavior of adhesive contact based on Lennard-Jones potential law, *J. Mech. Phys. Solids*. 111 (2018) 170–183.
- [157] A. Ptak, H. Gojzewski, M. Kappl, H.J. Butt, Influence of humidity on the nanoadhesion between a hydrophobic and a hydrophilic surface, *Chem. Phys. Lett.* 503 (2011) 66–70.
- [158] M. Farshchi-Tabrizia, M. Kappl, H.J. Butt, Influence of humidity on adhesion: An atomic force microscope study, *J. Adhes. Sci. Technol.* 22 (2008) 181–203.
- [159] H.K. Christenson, J.N. Israelachvili, Growth of ionic crystallites on exposed surface, *J. Colloid Interface Sci.* 117 (1987) 576–577.
- [160] P.J. Van Zwol, G. Palasantzas, J.T.M. De Hosson, Influence of roughness on capillary forces between hydrophilic surfaces, *Phys. Rev. E*. 78 (2008) 031606.
- [161] S. Wu, *Polymer interface and adhesion*, M. Dekker, New York, 1982.
- [162] R.L. Fisher, Direct measurement of the effect of meniscus forces on adhesion: a study of the applicability of macroscopic thermodynamics to microscopic liquid interfaces, *Colloids Surf.* 3 (1981) 303–319.
- [163] M. Ciavarella, J. Joe, A. Papangelo, J.R. Barber, The role of adhesion in contact

- mechanics, *J. R. Soc. Interface.* 16 (2019) 20180738.
- [164] H. Yu, Z. Li, Q.J. Wang, Viscoelastic-adhesive contact modeling: Application to the characterization of the viscoelastic behavior of materials, *Mech. Mater.* 60 (2013) 55–65.
- [165] X. Zhu, E. Siamantouras, K.K. Liu, X. Liu, Determination of work of adhesion of biological cell under AFM bead indentation, *J. Mech. Behav. Biomed. Mater.* 56 (2016) 77–86.
- [166] Y.C. Fung, *Biomechanics: Mechanical properties of living tissues*, Springer-Verlag New York, 1993.
- [167] E.H. Lee, J.R.M. Radok, The Contact Problem for Viscoelastic Bodies, *J. Appl. Mech.* 27 (1960) 438–444.
- [168] R.W. Carpick, D.F. Ogletree, M. Salmeron, A general equation for fitting contact area and friction vs load measurements, *J. Colloid Interface Sci.* 211 (1999) 395–400.
- [169] J.A. Greenwood, K.L. Johnson, The mechanics of adhesion of viscoelastic solids, *Philos. Mag. A.* 43 (1981) 697–711.
- [170] K. Kendall, Cracks at adhesive interfaces, *J. Adhes. Sci. Technol.* 8 (1994) 1271–1284.
- [171] B.N.J. Persson, E.A. Brener, Crack propagation in viscoelastic solids, *Phys. Rev. E.* 71 (2005) 036123.
- [172] A.N. Gent, J. Schultz, Effect of wetting liquids on the strength of adhesion of viscoelastic materials, *J. Adhes.* 3 (1972) 281–294.
- [173] D. Maugis, M. Barquins, Fracture mechanics and the adherence of viscoelastic bodies, *J. Phys. D. Appl. Phys.* 11 (1978) 1989–2023.
- [174] M. Ahearne, Y. Yang, A.J. El Haj, K.Y. Then, K.K. Liu, Characterizing the viscoelastic properties of thin hydrogel-based constructs for tissue engineering applications, *J. R. Soc. Interface.* 2 (2005) 455–463.
- [175] A. Tiwari, L. Dorogin, A.I. Bennett, K.D. Schulze, W.G. Sawyer, M. Tahir, G. Heinrich, B.N.J. Persson, The effect of surface roughness and viscoelasticity on rubber adhesion, *Soft Matter.* 13 (2017) 3602–3621.
- [176] L. Dorogin, A. Tiwari, C. Rotella, P. Mangiagalli, B.N.J. Persson, Role of preload in adhesion of rough surfaces, *Phys. Rev. Lett.* 118 (2017) 238001.
- [177] K.E. Jensen, R. Sarfati, R.W. Style, R. Boltyanskiy, A. Chakrabarti, M.K. Chaudhury, E.R. Dufresne, Wetting and phase separation in soft adhesion, *Proc. Natl. Acad. Sci. U. S. A.* 112 (2015) 14490–14494.
- [178] R. Shuttleworth, The surface tension of solids, *Proc. Phys. Soc. Sect. A.* 63 (1950) 444.
- [179] R.C. Cammarata, Surface and interface stress effects in thin films, *Prog. Surf. Sci.* 46 (1994) 1–38.
- [180] E. Orowan, Surface energy and surface tension in solids and liquids, *Proc. R. Soc. London. A.* 316 (1970) 473–491.
- [181] D. Maugis, *Contact, adhesion and rupture of elastic solids*, Springer Science & Business Media, 2013.

- [182] S.C. Thakur, J.P. Morrissey, J. Sun, J.F. Chen, J.Y. Ooi, Micromechanical analysis of cohesive granular materials using the discrete element method with an adhesive elasto-plastic contact model, *Granul. Matter.* 16 (2014) 383–400.
- [183] S. Razavi, L.M. Hernandez, A. Read, W.L. Vargas, I. Kretzschmar, Surface tension anomaly observed for chemically-modified Janus particles at the air/water interface, *J. Colloid Interface Sci.* 558 (2020) 95–99.
- [184] J. Duriez, R. Wan, Contact angle mechanical influence in wet granular soils, *Acta Geotech.* 12 (2017) 67–83.
- [185] X.-Y. Lu, L. Chen, C.-Y. Wu, H.-K. Chan, T. Freeman, The effects of relative humidity on the flowability and dispersion performance of lactose mixtures, *Materials (Basel).* 10 (2017) 592.
- [186] J.C. Vincent, J. Hill, M.D. Walker, S.A. Smith, S.E. Smith, N.E. Cant, Towards a predictive capability for the resuspension of particles through extension and experimental validation of the Biasi implementation of the “Rock’n’Roll” model, *J. Aerosol Sci.* 137 (2019) 105435.
- [187] T. Defraeye, A. Radu, D. Derome, Recent advances in drying at interfaces of biomaterials, *Dry. Technol.* 34 (2016) 1904–1925.
- [188] N.I. Uzhegova, A.L. Svistkov, B. Lauke, G. Heinrich, The influence of capillary effect on atomic force microscopy measurements, *Int. J. Eng. Sci.* 75 (2014) 67–78.
- [189] M. V. Vitorino, A. Vieira, C.A. Marques, M.S. Rodrigues, Direct measurement of the capillary condensation time of a water nanobridge, *Sci. Rep.* 8 (2018) 13848.
- [190] J.O. Wolff, S.N. Gorb, The influence of humidity on the attachment ability of the spider *Philodromus dispar* (Araneae, Philodromidae), *Proc. R. Soc. B Biol. Sci.* 279 (2012) 139–143.
- [191] M. Paajanen, J. Katainen, O.H. Pakarinen, A.S. Foster, J. Lahtinen, Experimental humidity dependency of small particle adhesion on silica and titania, *J. Colloid Interface Sci.* 304 (2006) 518–523.
- [192] A. Fukunishi, Y. Mori, Adhesion force between particles and substrate in a humid atmosphere studied by atomic force microscopy, *Adv. Powder Technol.* 17 (2006) 567–580.
- [193] J. Lehr, A.-M. Kietzig, Dependence of capillary forces on relative humidity and the surface properties of femtosecond laser micromachined titanium, *J. Colloid Interface Sci.* 448 (2015) 356–366.
- [194] S. Ito, S.N. Gorb, Fresh “pollen adhesive” weakens humidity-dependent pollen adhesion, *ACS Appl. Mater. Interfaces.* 11 (2019) 24691–24698.
- [195] R.A. Quon, A. Ulman, T.K. Vanderlick, Impact of humidity on adhesion between rough surfaces, *Langmuir.* 16 (2000) 8912–8916.
- [196] N. Cadirov, J.A. Booth, K.L. Turner, J.N. Israelachvili, Influence of humidity on grip and release adhesion mechanisms for gecko-inspired microfibrillar surfaces, *ACS Appl. Mater. Interfaces.* 9 (2017) 14497–14505.
- [197] L. Sirghi, N. Nakagiri, K. Sugisaki, H. Sugimura, O. Takai, Effect of sample topography on adhesive force in atomic force spectroscopy measurements in air, *Langmuir.* 16 (2000) 7796–7800.
- [198] M. Dörmann, H.J. Schmid, Simulation of capillary bridges between nanoscale

- particles, *Langmuir*. 30 (2014) 1055–1061.
- [199] L. Yang, J. Hu, K. Bai, Capillary and van der Waals force between microparticles with different sizes in humid air, *J. Adhes. Sci. Technol.* 30 (2016) 566–578.
- [200] T.C. Halsey, A.J. Levine, How sandcastles fall, *Phys. Rev. Lett.* (1998) 3141.
- [201] H.N.G. Nguyen, C.-F. Zhao, O. Millet, A.P.S. Selvadurai, Effects of surface roughness on liquid bridge capillarity and droplet wetting, *Powder Technol.* 378 (2021) 487–496.
- [202] X. Li, M. Dong, H. Zhang, S. Li, Y. Shang, Effect of surface roughness on capillary force during particle-wall impaction under different humidity conditions, *Powder Technol.* 371 (2020) 244–255.
- [203] O. Pitois, P. Moucheront, X. Chateau, Liquid bridge between two moving spheres: An experimental study of viscosity effects, *J. Colloid Interface Sci.* 231 (2000) 26–31.
- [204] L. Wang, S. Régnier, A more general capillary adhesion model including shape index: single-asperity and multi-asperity cases, *Tribol. Trans.* 58 (2015) 106–112.
- [205] G. Lian, J. Seville, The capillary bridge between two spheres: New closed-form equations in a two century old problem, *Adv. Colloid Interface Sci.* 227 (2016) 53–62.
- [206] M. Dörmann, H.-J. Schmid, Distance-dependency of capillary bridges in thermodynamic equilibrium, *Powder Technol.* 312 (2017) 175–183.
- [207] D.B. Asay, S.H. Kim, Effects of adsorbed water layer structure on adhesion force of silicon oxide nanoasperity contact in humid ambient, *J. Chem. Phys.* 124 (2006) 174712.
- [208] Y.I. Rabinovich, M.S. Esayanur, K.D. Johanson, J.J. Adler, B.M. Moudgil, Measurement of oil-mediated particle adhesion to a silica substrate by atomic force microscopy, *J. Adhes. Sci. Technol.* 16 (2002) 887–903.
- [209] L. Gao, T.J. McCarthy, Contact angle hysteresis explained, *Langmuir*. 22 (2006) 6234–6237.
- [210] Y. Yuan, T.R. Lee, Contact angle and wetting properties, in: *Surf. Sci. Tech.*, Springer, Berlin, Heidelberg, 2013: pp. 3–34.
- [211] Y. Ma, X. Cao, X. Feng, Y. Ma, H. Zou, Fabrication of super-hydrophobic film from PMMA with intrinsic water contact angle below 90°, *Polymer (Guildf)*. 48 (2007) 7455–7460.
- [212] D. Nečas, P. Klapetek, Gwyddion: An open-source software for SPM data analysis, *Cent. Eur. J. Phys.* 10 (2012) 181–188.